

# Correlation of electronic transport and structure in Pb atomic wires on Si(557) surfaces

Von der Fakultät für Mathematik und Physik  
der Gottfried Wilhelm Leibniz Universität Hannover  
zur Erlangung des Grades

**Doktor der Naturwissenschaften**

Dr. rer. nat.

genehmigte Disertation

von

**Dipl.-Phys. Marcin Czubanowski**

geboren am 24. Oktober 1978 in Posen

2009

2

Referent: Prof. Dr. H. Pfnür

Korreferent: PD Dr. C. Tegenkamp

Tag der Promotion: 29.06.2009

Keywords: One dimensional Pb-wires, conductance in low dimension, SPA-LEED

Schlagwörter: Eindimensionale Pb-Drähte, Leitfähigkeit von den niedrigdimensionalen Strukturen, SPA-LEED

## Abstract

One dimensional electron systems are very interesting because they exhibit a wealth of interesting physical phenomena, such as the quantization of conductance, Peierls instability, Fermi or Luttinger liquids behavior. These effects have been intensively studied with respect to structure and electronic configuration as both are related to each other. The Pb/Si(557) system, which is the subject of this thesis, manifests a phase transition for a Pb coverage of 1.31 ML. This phase transition is observed at temperatures as low as  $T_c = 78K$  and switches between two states. In the high temperature state, the conductivity is thermally activated and has very low anisotropy. For the low temperatures, the conductivity switches into high anisotropy state (a factor of 60). Later in, it was shown that this quasi-1D behavior is a consequence of the interactions within the structure that as a whole are strongly two dimensional.

The goal of this work was to study more the nature of the Pb/Si(557) phase transition. To this end, the structure behavior as characterized through the SPA-LEED, and the electronic transport behavior as characterized through the conductivity measurements were essential to obtain.

The electron scattering experiment performed on the discussed system, has delivered information about the periodic arrangement of the Pb/Si(557) structure that correlates with the STM measurement. The spot splitting at a temperature below  $T_c$  in the  $[\bar{1}\bar{1}2]$  direction are directly related to the average wire separation of 1.55 nm. In addition, the structure of the wires itself has been inspected and a model of the atomic configuration is given. The devil's staircase regime that describes the atomic structure of the wires has been observed in the coverage range of 1.2–1.31ML. Moreover, the most striking result in this section was that the step structure of the Si(557) surface could be modulated via Pb concentration at low temperatures.

The structure stability of 1.31ML Pb/Si(557) has been investigated with LEED under variable temperature conditions. The main point of interest was the structural changes at  $T_c$  for the (1,5) phase, for which the electrical phase transition has been observed. From the energy dependence of the reflex positions, the surface facets orientation was determined to changes from  $[223]$  direction below  $T_c$  to higher index surface e.g.  $[17\ 17\ 25]$ . This effect has been contributed to the coupling of the electronic and lattice variations.

Finally, the electron transport has been examined as a function of coverage, temperature and magnetic field with respect to wire direction. For the (1,5) phase of Pb/Si(557) system, the phase transition has been observed to be very sharp at  $T_c$ . It changes from a delocalized electron system at  $T > T_c$  to a quasi-1D metal phase at  $T < T_c$ . The evaluation of the phase transition with excess coverage has been measured as well. The band gap filling via increase of Pb concentration at the step edges of Pb(223) facets has been observed as a decrease of the logarithm of the conductance as a function of the coverage at  $T < T_c$ . The Pb excess coverage leads to the formation of 1D superlattices which modify the electronic stabilization of the Pb(223) surface as measured by LEED. The measurements performed in a magnetic field show that the Fermi nesting condition is destroyed already at around 2T. This effect can be attributed to the Zeeman energy level splitting. The fact that weak anti-localization has been observed at coverages higher than 1.32ML points towards the enhanced spin-orbit coupling.



## Zusammenfassung

Eindimensionale Elektronensysteme erzeugen großes Interesse auf Grund der großen Zahl von interessanten physikalischen Phänomenen, wie z.B. Quantisierung der Leitfähigkeit, Peierls-Instabilitäten und Fermi- oder Luttinger-Flüssigkeitsverhalten. Sowohl die elektronische Konfiguration, als auch die Struktur dieser Systeme wurden intensiv untersucht, da beide in engem Zusammenhang stehen. Das System Pb/Si(557), welches den Untersuchungsgegenstand dieser Arbeit darstellt, zeigt bei einer Bleibedeckung von 1,31 ML einen Phasenübergang. Dieser Phasenübergang kann bei einer Temperatur von  $T_c = 78K$  beobachtet werden. Im Hochtemperaturbereich ist die Leitfähigkeit thermisch aktiviert und besitzt eine sehr niedrige Anisotropie. Bei niedrigen Temperaturen springt die Leitfähigkeit in einen stark anisotropen Zustand. Es wird gezeigt, dass dieses quasiaendimensionale Verhalten eine Konsequenz der Wechselwirkungen innerhalb der Struktur darstellt, welche aber als Ganzes zweidimensional ist.

Das Ziel der vorliegenden Arbeit war einen tieferen Einblick in die Natur dieses Phasenüberganges zu gewinnen, dazu wurden sowohl strukturelle (SPA-LEED), als auch elektronische (Transportmessungen) Untersuchungen durchgeführt.

Die Elektronenbeugung am beschriebenen System liefert Informationen über die periodische Anordnung der Pb/Si(557) Struktur, die mit STM-Messungen im Einklang stehen. Die Aufspaltung der Reflexe unterhalb von  $T_c$  in  $[\bar{1}\bar{1}2]$ -Richtung steht direkt mit dem Drahtabstand von 1,55 nm in Zusammenhang. Außerdem wurde die Struktur der Drähte selbst untersucht und es wird ein entsprechendes Model angegeben. Im Bereich von 1,2 – 1,3 ML beschreibt eine "devil's staircase" die Struktur der Drähte. Außerdem wurde als wesentliches Ergebnis dieses Abschnittes festgestellt, dass sich bei tiefen Temperaturen die Stufenstruktur über die Bleibedeckung verändern lässt.

Die Stabilität der 1.31ML Pb/Si(557) Struktur wurde mittels LEED bei variabler Temperatur untersucht. Im Fokus des Interesses standen hierbei die strukturellen Veränderungen bei  $T_c$  für die (1,5)-Phase, an der der elektronische Phasenübergang beobachtet wurde. Aus der Energieabhängigkeit der Reflexpositionen konnte ermittelt werden, dass sich die Oberflächenfacetten von [223] unterhalb  $T_c$  auf höher indizierte Flächen (z.B. [17 17 25]) ändern.

Abschließend wurde der elektronische Transport als Funktion der Bedeckung und eines Magnetfeldes in Abhängigkeit von der Drahrichtung untersucht. Für die (1,5)-Phase des Pb/Si(557)-Systems wird dabei ein sprunghafter Phasenübergang bei  $T_c$  beobachtet. Dabei wandelt sich ein delokalisiertes Elektronensystem bei  $T > T_c$  in einen quasiaendimensionales System bei  $T < T_c$ . Die Abhängigkeit des Phasenüberganges von zusätzlicher Bleibedeckung wurde ebenso untersucht. Das Füllen der Bandlücke mit steigender Pb-Bedeckung führt zu einem Abklingen des Logarithmus der Leitfähigkeit mit der Temperatur bei  $T < T_c$ . Das überschüssige Blei führt zu einem eindimensionalen bergitter, welches die elektronische Stabilität der im LEED gemessenen Pb(223)-Oberfläche verändert. Die Magnetfeldmessungen zeigen, dass die "Fermi-Nesting" Bedingung bereits bei Feldern von 2 T zerstört wird. Dieser Effekt kann der Zeeman-Energieaufspaltung zugerechnet werden. Die Tatsache, dass schwache Antilokalisierung bei Bedeckungen größer als 1,32 ML beobachtet wurde deutet auf eine verstärkte Spin-Orbit-Kopplung hin.

# Inhaltsverzeichnis

<b>1</b>	<b>Introduction</b>	<b>8</b>
<b>2</b>	<b>Theoretical background</b>	<b>13</b>
2.1	Pb/Si(111) - Devil's staircase . . . . .	14
2.2	Charge transport theory . . . . .	17
2.2.1	The model of free electrons (Drude model) . . . . .	17
2.2.2	Anderson-localization . . . . .	20
2.2.3	Weak localization . . . . .	22
2.2.4	Size effect . . . . .	23
2.2.5	Electron confinement in 1D . . . . .	25
2.2.6	1D system and Charge Density Waves instability . . . . .	26
<b>3</b>	<b>Experimental</b>	<b>29</b>
3.1	Ultra High Vacuum System . . . . .	29
3.1.1	SPA - LEED . . . . .	30
3.1.2	Cryostat . . . . .	36
3.1.3	Sample holder . . . . .	36
3.2	Lead Evaporator . . . . .	37
3.3	Conductivity measurements . . . . .	39
3.3.1	Two-point measurements . . . . .	39
3.3.2	Four - point measurements . . . . .	40
3.3.3	Eight-point measurements . . . . .	43
<b>4</b>	<b>Silicon (557)</b>	<b>45</b>
4.1	Silicon Bulk . . . . .	45
4.2	The vicinal silicon (557) surface . . . . .	46
4.3	Other vicinal silicon surfaces . . . . .	48
<b>5</b>	<b>Sample preparation and characterization</b>	<b>51</b>
5.1	Preparation of Si(557) and $TiSi_2$ -contacts . . . . .	51
5.2	Electrical characterization of the contacts . . . . .	54
5.3	Electrical characterization of Pb films on Si(557) . . . . .	56

<i>INHALTSVERZEICHNIS</i>	7
<b>6 Pb-coverage phase diagram</b>	<b>61</b>
6.1 Supplement . . . . .	79
<b>7 Temperature driven phase transition</b>	<b>81</b>
<b>8 Metal insulator transition</b>	<b>91</b>
8.1 Suppression of the phase transition . . . . .	92
8.2 Formation of superlattices on vicinal surfaces . . . . .	93
8.3 Transport in the superlattice . . . . .	97
8.4 Magnetoresistance measurements . . . . .	101
<b>9 Summary and outlook</b>	<b>104</b>
<b>Bibliography</b>	<b>110</b>
<b>List of abbreviations</b>	<b>111</b>
<b>10 Acknowledgments</b>	<b>112</b>

# Kapitel 1

## Introduction

The last few decades have shown how interesting low dimensional systems can be. Systems such as In/Si(111) [1], Si(111) $\sqrt{3} \times \sqrt{3}$ -Ag [2] or Pt/Ge(100) silicide [3] have shown that it is possible to reduce the dimensionality of the structure to 2D or quasi-1D on top of a semiconductor surface. For example, in the In/Si(111) system, the adsorbate atoms create a pattern of narrow wires showing a (4x1) reconstruction at the coverage of 1ML. This structure undergoes a reversible phase transition at lower temperature where (4x1) switches to (8x2) reconstruction causing doubling of the lattice constant along the In-chains. This effect results in the modification of the surface states from quasi-1D conductor into an insulator at T=130K. The electron transport measured along the wires indicates insulating behavior in the parallel direction to the wires while the temperature goes below 130K [4]. Such behavior has been theoretically predicted by Peierls, who suggests that the chain of atoms is unstable due to the electronic configuration of the crystal. This results in a band gap opening at the Fermi level. The energy gained by lowering the temperature, which in other words means that the valence band shifts to lower energies, exceeds the strain energy that is necessary for the displacement.

As a second example, experiments performed on the Si(111) $\sqrt{3} \times \sqrt{3}$ -Ag system have successfully demonstrated the effect of doping on semiconductor material via noble metal adatoms. The detailed study of the band dispersion has shown that at lower dimension, the conduction band moves with doping. This, as well as the fact that the bottom of the conduction band has been observed as flat line, suggests a break-down of the effective mass approximation and a rigid-band model. It was shown by photoemission spectroscopy that at very high doping level, the 2D semiconductor becomes metallic.

Finally, the specific example of 1D pattern are the Pt/Ge(100) silicide systems. The wires of 1 atomic width were obtained on a mesoscopic scale with very low defects and impurity concentration. The self assembled chains of Pt were acting as a barrier for the surface states of the Ge substrate. As a result, the electronic states on the Ge terraces could be treated as a quantum particle in a well. The

striking feature and impressing observation was, that in this case the confinement was not in the wires as was in the case of Ag and In, but on the Ge surface states that have metallic character and are between two adjacent chains. As measured by ARPES, due to this confinement at low temperature (77K), new energy levels of the Pt wires has been registered. The energies of these new states were higher than the energies of the aforementioned Ge surface state that is located near the Fermi level. Due to this fact, the Pt structures were acting as the walls of the well.

The common property amongst all of the systems is the strong correlation of the atomic structure with its band configuration. In all cases the structure and energy band changes have been measured by combination of STM, ARPES and diffraction techniques with each others. The correlation between adjacent structure make the systems more quasi-1D then real 1D system. However, electron confinement has been achieved in real systems that can be used for experimental investigation. For the systems where electrons become localized or have to propagate in structures of sizes that are comparable with their wavelengths, the charge and spin can be treated separately as two quasi-particles. This is the case where Luttinger liquids behavior are observed. Unlike the electrons in 3D and 2D, where electron transport can be described as billiard ball behavior, in the 1D case, due to the confinement, the electrons are forced to head-on collisions. In this case the quantum behavior is not negligible and interference of the wave packets of the electrons occurs. Since no such system can be considered purely 1D, so if one of the electrons will be excited, this will generate a chain reaction that will result in collective excitations of all the electrons that are in such confinement systems. Additionally, if the correlation of the electrons within the wires also induce the pairing of the electrons, the behavior predicted in the Luttinger model will be observed; namely, the separation of the charge and the spin. This can be observed as charge or spin density waves.

One of the systems that can be classified into the 1D category are Pb structures in the mono layer-regime, grown on vicinal Si(557) surfaces. What distinguishes the Pb/Si(557) system from the other quasi-1D structures under study, is the ability to change the periodic structure of the substrate by material transport. That means, due to the electronic stabilization the mass-transport in the Si substrate occurs and changes the periodic arrangement of the steps varying the terraces width. Because of the fact that the structure and the electronic properties are connected with each other, it is challenging to examine both properties on the same samples. The correlation of the structural information with the electronic properties obtained via DC-conductance measurements has been the main topic of this work. The structure has been investigated with SPA-LEED which gave the opportunity to study the long range correlation between the Pb-chains and resulting structural changes as well as the structure of the wires itself. As it was revealed in a previously performed investigation performed on this system [5], the chain structure of Pb/Si(557) undergoes the electrical phase transition at

78K. This observation has been correlated by STM with the wire-like structure. Although this finding has clearly show that the phase transition is connected with the changes of the interaction between the wires switching between frozen wires and thermal vibrations, there were still open questions such as what exactly is driving this sudden change in conductance or what is the structure of the single Pb-wire that has been subjected to the conductivity measurement.

Speaking of low dimensional objects that has been obtained by self-assembly, one has to consider a chain that is strongly coupled to the underlying substrate and has finite probability to interact with the neighboring chain as it was demonstrated above. This introduces the instabilities of the ground state of such a chain. The electron - phonon interaction that in the simplest form is given as Peierls transition or Cooper- pairs are enhanced in such systems. Those effects are strongly visible when the temperature is lowered. At lower temperatures, the system tries to lower the energy to reach the lowest possible ground state. This leads to the gap opening in the electronic structure that strongly depends on the interaction between the chains [6]. The interaction between the wires can block the phonon softening (in case of set of chains where the interaction between them is weak, phonon softening is visible as Kohn anomalies). In this case at lower temperatures, the lattice vibration of wave vector  $g = 2k_f$  will disappear and will not contribute to the resistivity that makes the Pb chains ideal conductors. Apart from the electronic configuration also the influence of the electronic stabilization or destabilization - depending on the temperature, coverage, etc. produces long and short range interaction between atomic chains in the sense of changing the periodic structure of the wires (Devil's staircase) [7], [8]. Those effects, particularly their behavior as a function of temperature, could only be seen by SPA-LEED.

Besides the electron - phonon coupling, the electron-electron and spin-orbit coupling can contribute to the interacting quasi-particle or quasi-1D picture. In the quasi-1D system where the electron transport can be strongly influenced by the defects within the structure, the interaction between the lattice vibration and interference with other electrons have to be taken into account [9]. Those effects can be observed as the decrease of the resistivity if a magnetic field is applied. By studying the conductance in the magnetic field it is possible to describe in more detail the scattering processes and, as it will be shown in this thesis, the influence of the momentum induced by the B-field on the nesting condition that has been observed for the 1.3ML of Pb/Si(557). It will be shown that this conditions can be destroyed by splitting of the energy level at the nesting points (Zeeman effect). Following the idea given in [2] and increasing the amount of Pb on electronically stabilized system of Pb(223), the evolution of the sub-band due to increase of the number of electrons per unit cell could be observed. This would be the experimental evidence for doping. The study of the excess coverage onto the 1.3ML Pb/Si(557) system will be presented as structure and electronic changes. Also the influence of the magnetic field on the electron transport at low temperatures

for the mentioned coverage range has been studied.

As discussed, the Pb/Si(557) system give lots of room for examination of the 1D electron behavior. An advantage of this work is the conductivity measurement, which deliver direct information about macroscopic conductance properties measured on this same system without the need for sample transfer into a different experimental setup.





# Kapitel 2

## Theoretical background

Low dimensional systems have been attracting much attention because of their new electronic properties as well as electron transport phenomena that have been observed for systems based on e.g. carbon nano-tubes or lithographically structured objects. The electrons in low dimensions show many interesting properties like ballistic transport, localization, scattering at certain defects or interesting magnetic properties if exposed to a magnetic field. Moreover, the systems where the electrons are localized in one or two dimensions show interaction-driven 2D metal-insulator transitions, the formation of CDW or the transition between different magnetic or electronic states. To explore such behavior, new techniques of preparation of 1D and 2D systems have been looked for. One possible way is to use epitaxy on vicinal surfaces of semiconductor materials for the following reasons:

- The first important property of a semiconductor is the low surface energy that is the condition for epitaxial growth of metals.
- The second feature is the very high resistance of the bulk crystal at low temperatures. Very low conductance of the substrate surface assures the current to flow through the structure on top of the substrate and thus giving very low substrate contribution to the conductivity measurements.
- The third important feature of vicinal surfaces is the regular atomic step arrangement on the substrate surface with well defined distances between the step edges. The average step-step separation depends on the miscut angle. Typically, a precision of  $0.1^\circ$  can be obtained. So, by choosing the initial miscut angle, one is able to obtain different periodicities of the steps. Epitaxy of any metal in the mono-layer range at such a surface will then be stimulated and influenced by the periodicity of the steps of the substrate.

The most popular semiconductor is silicon due to its chemical and physical properties described in chapter 5. The vicinal silicon surfaces were also intensively

investigated and their crystallographic and electronic structure is well known [10, 11, 12]. The most stable and popular examples are Si(553), Si(779), Si(557) surfaces which have been used to perform spectacular experiments with Ag and Au quantum structures. The vicinality of the surface has been used to produce 1D structures via step decoration. Another interesting system based on metal and vicinal silicon surface is Pb/Si(557) system (*see chapter 6*). It has been shown that this system at certain coverage shows a phase transition at  $T_C = 78K$ . In this thesis, it will be shown that Pb destabilizes the substrate surface and leads to a reorganization of the step structure. A modulation of the coverage by very few Pb atoms destabilizes electronically the whole system and leads to the formation of different unit cells by changing the so-called domain wall structure. In this section the basics of the long and short range interaction will be discussed as the Devil's staircase model. The second part of this section will give a closer look at electron transport phenomena in low diemensions.

## 2.1 Pb/Si(111) - Devil's staircase

As the internal structure of Pb-wire growth on narrow Si(111) terraces of the Si(557) surface was an open question that has been answered within the scope of this experimental work, it is important to review the experimental evidence for Pb configuration on the Si(111) surface. As recently shown by Tringides [13], the problem of the dense  $\alpha\sqrt{3} \times \sqrt{3}$  phase of the Pb/Si(111) systems and their variety of different LEED patterns has been discussed as long and short range interaction between Pb linear structures that grow in the coverage range of 1.2 - 1.3 ML. It has been found for this system that Pb can form not only  $\sqrt{3} \times \sqrt{3}$  structures, but due to the free sites of the underlying silicon substrate and the lattice mismatch between Pb and Si also  $\sqrt{7} \times \sqrt{3}$  unit cells and the combination of both are observed as spot splitting in the LEED pattern at the  $\sqrt{3}$  positions. Considering the Si unit cell with its 7x7 reconstruction, one can distinguish 3 positions that Pb atoms can occupy. The three sites have been named T1, H3 and T4 positions and this notation has been widely used in the literature. Those positions are marked in the picture of Si surface model presented in fig.2.1 for better understanding.

The position  $T_1$  is above the atoms of the first silicon layer. The adsorbate atom is simply bound to the underlying silicon atom. This position is also known in the literature as the  $\ddot{O}$ n Topposition. The position  $T_4$  is the site between three substrate atoms of the first layer and the adsorbate that lies on top of the atom of the second layer. The  $H_3$  position is exactly in the middle of the hexagon of atoms of the first Si layer. If the unit cell of Pb would perfectly match the silicon substrate only 1x1 and  $\sqrt{3} \times \sqrt{3}R30^\circ$  would be observed. Because of the fact that the Pb lattice constant is smaller than the silicon lattice constant, the unit cell of Pb can be slightly shifted out of their positions that has been mentioned above

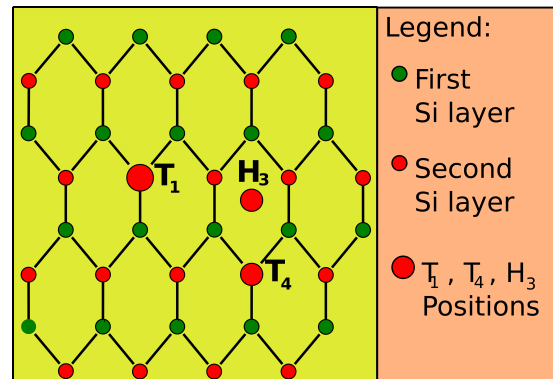


Abbildung 2.1: Model of the silicon surface. Red circle are corresponding to the Si atoms in the second layer and green to the Si atoms in the first layer. The  $T_{1,4}$  and  $H_3$  positions are marked.

as  $H_3$ ,  $T_1$  and  $T_4$ , with respect to the silicon substrate. This results in changing the distances between the Pb atoms within the Pb unit cell and occupying the  $H_3$  position that would be next to it. A shift of the whole Pb structure to the next free  $H_3$ -position results in the  $\sqrt{7} \times \sqrt{3}$  unit cell. This is shown in fig. 2.2.

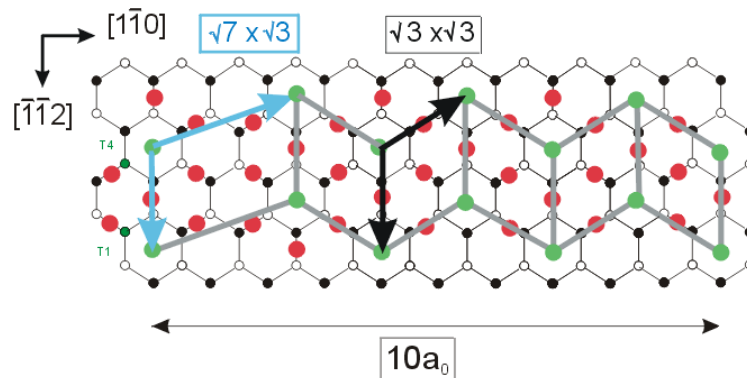


Abbildung 2.2: Model of the Silicon surface with Pb adsorbate in  $\sqrt{7} \times \sqrt{3}$  and  $R30^\circ \sqrt{3} \times \sqrt{3}$  configuration.

In addition to two elementary units, also the combination of these units is shown. It can be easily seen that with these two elementary units one can create periodic arrangements of arbitrary lattice constant that consists of the mentioned unit cells. For the Pb/Si(111) system, it has been shown that depending on the amount of lead and substrate temperature numerous phases can be distinguished [13]. According to the work of M. Tringides *et. al* [13] a phase diagram has been shown in fig. 2.3. The higher order periodicity that has been schematically shown was also known as domain wall structure in the earlier study [14]. It's origin

lies at the lattice mismatch between the adsorbate and substrate which in fact induces the tension between both. According to the Tringides group the linear phases, that have been called Devil's staircase (DS), have two parameters  $m$  and  $n$  that are independent from each other though both numbers are strictly related to the coverage  $\theta$ . The parameter  $m$  and  $n$  correspond to the number of the  $\sqrt{7} \times \sqrt{3}$  and  $\sqrt{3} \times \sqrt{3}$  unit cells respectively and relate them to the coverage. Holding  $m$  parameter and changing the  $n$  number, a whole series of phases can be created. This same rule applies for fixing  $n$  and  $m$  changing. In the phase diagram in fig 2.3 the extreme cases ( $m$ -changing,  $n$ -fixed and  $m$ -fixed,  $n$ -changing) are plotted. The competition between the long range repulsive interaction, which increases with the coverage and the chemical potential of the surface, as well as pile-up of the tension results in the formation of the mentioned DS. This relation can only be explained when the long range periodicity occurs. The reason why this happens is in the coverage difference between two neighboring phases. It has been experimentally shown that from one phase to another, only as much as 0.001ML additional Pb is needed. Reorientation of the surface into completely new periodic arrangements at very low temperatures can only occur when the adatoms have enough energy to move from one site to another and this is accounted to the lowering of the surface potential by a long range interaction.

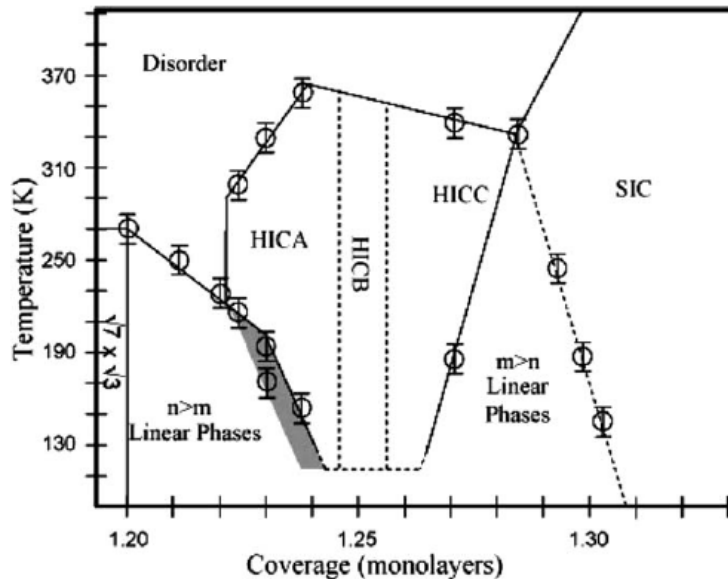


Abbildung 2.3: Phase diagram for Pb/Si(111) system at the coverage between  $\frac{6}{5}$  and  $\frac{4}{3}$  coverage and temperatures range of (130, 370)K [15]

A remarkable observation of the DS on Pb/Si(111) has been made at very low temperatures, i.e. in the temperature range 120-250K. Evaporation of only 0.001ML

already results in a structural change. At this temperature range around 15 different phases could be distinguished as shown in the phase diagram in fig.2.3 illustrated by the points marked with circles. This raises the question about the kinetics of the adsorbate. Intuitively, one would expect higher mobility of atoms at higher temperatures (higher than 120K). However, the Pb atoms have very long diffusion path and form the periodic structure dictated by the DS condition already at 120K as mentioned. This suggests that the periodicity given by DS increases the energy of the adsorbate via electronic configuration at 1D phase of the DS diagram. A similar phenomenon is found for excess Pb coverage on a Pb(223) facets structure, showing long range ordered chain structure (c.f. with chapter 8).

## 2.2 Charge transport theory

In this section, the transport theory will be briefly described. The theory that explains the electron transport in a metal (Drude model) will give an overview of what is expected from a metallic film, that due to its dimension can be considered as a 3D sample. The theory will be extended to be valid also for semiconducting materials. Reducing the dimension of the sample and inducing defects, the conductivity behavior changes dramatically. In the following different scattering and localization effects will be discussed. If the thickness will be reduced to the size where it can be correlated to the wavelength of the electron that is propagating in such a film, the scattering at the interface becomes dominant. The temperature dependency of the conductance for different morphologies will be described. Also, what has been observed within this work, the localization of electrons due to the periodicity of the structure will be presented (Fermi nesting). This is because the thin film of lead destabilizes electronically the substrate surface and forces the vicinal silicon surface to reorient into the new periodicity for which the size of the structure correlates with the Fermi vector causing localization of the electrons in the direction perpendicular to the wires (quasi-1D system).

### 2.2.1 The model of free electrons (Drude model)

The first description of the electrical properties of metals on the atomic scale was given by Drude in 1900, just 3 years after Thompson discovered the electron. The Drude model, often called "Free Electron model", presents a purely classical approach to the finite resistance in metals. Electrons were thought of as charged spheres, moving through a soup of metal ions, with finite probability to scatter. It is the scattering that gives rise to the resistivity, in the form of heat dissipation. The main assumptions of the Drude model are listed below:

- In the absence of an applied electric field (2.4) the electrons move in random directions colliding with random impurities and/or lattice imperfections in

the crystal arising from thermal motion of ions about their equilibrium positions. In this model the inelastic electron-phonon and electron-electron interactions are neglected.

- between collisions, other interactions are neglected.
- carriers of charge  $q$  have an isotropic effective mass  $m$  and scattering time  $\tau$ . This time does not depend on the position and the velocity of the electrons.
- the electric field  $\mathbf{E}$  accelerates electrons (2.4) with a force  $\mathbf{F}$  equal to  $e\mathbf{E}$ .
- the electrons behave as classical particles with energies determined by the temperature of the metal. Any collisions between electrons are instantaneous and lead to scattering.

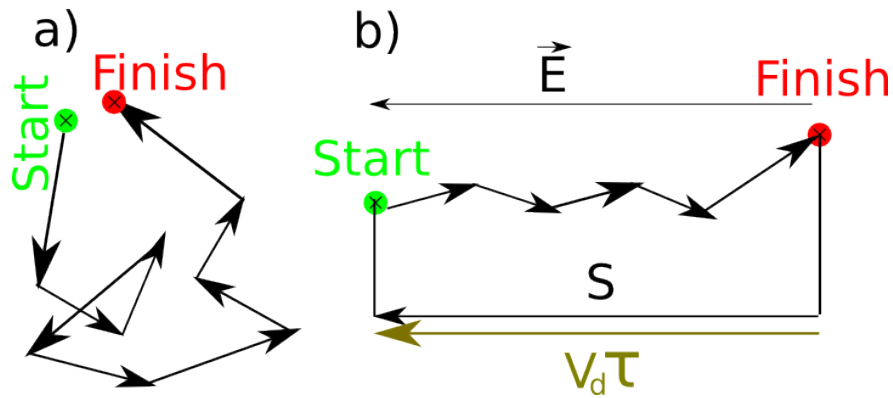


Abbildung 2.4: Electron path in metal solid with (a) and without (b) electric field

The greatest achievement of Drude was the explanation of Ohm's law on the atomic scale. With the assumptions pointed out above one can calculate the conductivity of metals by using Ohm's law:

$$\sigma = \frac{ne^2\tau}{m} \quad (2.1)$$

where

- $n$  : electron density
- $e = 1.6021 \times 10^{-19} \text{C}$  (elementary charge)
- $\tau$  : average time between collisions
- $m = 9.1091 \times 10^{-31} \text{kg}$  (electron rest mass)

In the formula 2.1  $\sigma$  is a scalar and this is valid only for an isotropic case. When the sample is placed e.g., in a external magnetic field, the conductivity has to be expressed as a tensor. Then the electron is moving under influences of the Lorentz force:

$$m \vec{v} = -e \left( \vec{E} + \vec{v} \times \vec{B} \right) - \gamma \vec{v} \quad (2.2)$$

where

$$\begin{aligned} \vec{v} & : \text{electron velocity} \\ \vec{E} & : \text{electrical field} \\ \vec{B} & : \text{magnetic filed} \\ \gamma & = \frac{m}{\tau} : \text{friction factor for collision between electrons and lattice} \end{aligned}$$

From equation 2.2 one can also obtain Ohm's law but in this case it is the resistivity  $\rho = \frac{1}{\sigma}$  and not the conductance that is presented as a tensor:

$$\rho = \rho_0 \begin{pmatrix} 1 & \omega_c \tau & 0 \\ -\omega_c \tau & 1 & 0 \\ 0 & 0 & 1 \end{pmatrix} \quad (2.3)$$

where

$$\begin{aligned} \rho_0 & = \frac{m}{ne^2\tau} \\ \omega_c & = \frac{eB}{m} : \text{cyclotron frequency} \end{aligned}$$

The diagonal elements of matrix in equation 2.3 are equal to 1 and they do not depend on the presence of an magnetic field which is in agreement with the Drude-model which considers the Fermi surface as ideal. However, for the real metal, the Fermi surface deviates from the theoretical sphere. This induces a change in conductance as a responce of a system to an external magnetica field as change of the conductanc. Assuming the difference between the Fermi surface of a real metal and an ideal sphere of free electrons model, the conductivity can be expressed as:

$$\sigma(B) = \frac{\sigma_0}{1 + (\omega_c \tau)^2} \approx \sigma_0 \{1 - (\omega_c \tau)^2\} \quad (2.4)$$

whereby  $\sigma_0$  is the conductivity for the case without a external field and can be calculated from 2.1.  $\omega_c = \frac{eB}{m}$  is the cyclotron frequency.

The next important limitation of the Drude model is that the equation 2.1 does not depend on temperature. The only parameter of the equation 2.1 which is temperature dependent is the relaxation time  $\tau$ . However to be able to explain

this relation between  $\tau$  and temperature, one needs to consider processes which describe electron scattering on the lattice in more detail. The electron in an ideal crystal can be described as a Bloch wave and is not subject to any kind of interaction with the lattice. However, in case of a real crystal, there are always electron interactions with the potential coming from lattice defects and foreign atoms. Beside this, there is also an influence from the interaction between electrons and phonons. If one omits the interaction between these two scattering processes then these two factors are summed up and represented as one factor (Matthiesen's principle) :

$$\rho(T) = \rho_0 + \rho_{Ph}(T) + \dots, \quad (2.5)$$

where the  $\rho_0$  is temperature independent and describes the scattering on lattice defects and  $\rho_{Ph}$  describes the electron-phonon scattering. At higher temperature the other terms of equ. 2.5, e.g. the term describing electron-electron interaction, are so small that they can be neglected.  $\rho_0$ , as one can see in equ. 2.5 is temperature independent and even at  $T=0$  K remains constant. One describes this as a residual resistivity. The factor  $\rho_{Ph}$  is proportional to the phonon concentration at temperatures higher than the Debye temperature ( $\theta_D$ ), which on the other hand is proportional to the temperature. Hence:

$$\rho(T) = \rho_0 + AT \quad (2.6)$$

where A is the temperature coefficient (TCR) and specific for each considered material. This constant does not characterize the defect density.

During the transition to lower temperatures high-energetic phonons freeze out, i.e. the phonon momentum drops to lower values. Due to this fact electrons can scatter into a small angle which significantly reduces the resistivity of metals. Therefore, for the simplest case, below the Debye temperature, the factor of phonon-scattering is formulated as:

$$\rho_{Ph}(T) \sim T^5 \text{ for } T \ll \theta_D \quad (2.7)$$

For  $T \rightarrow 0$  all phonons are frozen therefore,  $\rho_{Ph} \xrightarrow{(T \rightarrow 0)} 0$  too. The contribution of defects remains, therefore one can easily express the residual resistivity.

### 2.2.2 Anderson-localization

So far, all effects connected with charge transport were described by the Drude model. The electrons were considered as free particles moving in well ordered crystal lattices. The effect of localization can be observed when the atomic layers have some defects or the temperature of a sample is very low. In the case of disordered layers where the distance between defects is comparable with the atomic



distance, the classical description cannot be applied anymore. The scattering of electrons at defects plays the main role and quantum mechanical effects show up. Therefore the electrons have to be considered as waves. The first model concerning highly disordered films was given by Anderson [16]. His innovative work has shown that electrons in a crystal lattice can be localized. The electron is localized when the modulus square of a wave function of an electron decreases exponentially i.e.:

$$|\Psi(r)|^2 \sim e^{-\frac{r}{\xi}} \quad (2.8)$$

In equation 2.8  $\xi$  describes the localization length of a system with a volume  $L^3$ . The localization length is a parameter that depends on the disorder of the system or in other words, statistical deviation from the periodic potential. High disorder means short localization length. The small localization length results in localization of electrons. In fact this means that the metal film becomes an insulator while decreasing the temperature. Although this effect takes place there is the possibility of transport within an Anderson-localized film. However, the electron needs additional excitation energy to move from one localization center to another. This kind of effect is called *hopping transport*. The excitation energy is provided as thermal energy. For a certain temperature, the Anderson-localized film has a certain conductivity which drops with temperature until it is equal to zero at  $T = 0K$ . Then all electrons are localized and this state corresponds to a so called *Anderson-insulator*. At the temperatures above  $T \neq 0K$  the electrical transport depicts several limitations. Those limitations are then distinguished as specific model of the conductance that has been proposed.

The first model has been suggested by Mott [17] in 1971. He has discussed the probability of electron hopping from one localization center to the other. The hopping process is supported by interaction with the phonons. The main parameter that has been discussed in this model was the hopping rate that is related to the dimension of the considered metallic film. The conductivity can be described by the formula 2.9 where the relation between the hopping rate and the dimension parameter is expressed. This transport mechanism has been called variable range hopping, because it turns out that the electron can jump over one localization center that energetically is not favorable and occupy one center which is farther distant but has lower energy:

$$\sigma(T) \sim e^{\frac{T_0}{T} \frac{1}{n+1}} \quad (2.9)$$

where the  $n$  is the dimension parameter ( $0 < n < 3$ ), and  $T_0$  is the parameter given by  $\frac{18}{k_B N(E_F) \xi^3}$ . As it can be derived from the eq. 2.9, the different regimes are distinguished as the  $n$  parameter changes. In the case of strongly disordered 3D system eq. 2.9 changes into the form of eq. 2.10.

$$\sigma(T) \sim e^{\frac{T_0}{T} \frac{1}{4}}, \quad (2.10)$$

The eq. 2.10 described the temperature dependency of the hopping process. This temperature dependency has been experimentally shown mainly for measurements below 4K [18, 19, 20]. By reducing the dimensionality parameter down to  $n=1$  the formula presents the temperature dependency of the conductance which is attributed to the filling of the energy levels at Fermi level which in fact changes the electron density at the Fermi energy. This behavior has been observed for the Pb/Si(557) system at the coverage range of 1.3 to 1.4 ML where the decoration of the steps has been observed (c.f. chapter 8). Because of linear changes of the electron density the linear dependency of the log of conductance as a function  $1/T$  is expected.

### 2.2.3 Weak localization

For the systems at low temperatures mainly the scattering processes describe the conductance in the metallic low dimensional structures. The scattering can be distinguished with respect to the type of processes: elastic and inelastic scattering, that are described by the scattering time. In the usual case of a metallic 3D structure the inelastic processes are negligible. However, at reduced dimensions (or as it was observed early [21],[22] in highly disordered 3D systems), the elastically scattered electrons are quite often interfering with the electrons that has been elastically scattered on the scattering centers such as impurities, defects, etc.... Due to the fact that the phase has been conserved after inelastic scattering it is possible to observe such processes. Moreover, it has been shown that at low temperatures [23] the inelastic scattering time can be much higher than the elastic one. These processes lead to non-linear conductance observed at low temperatures. Studying the scattering time of the electrons, one can gain knowledge about the type of the localization that in the process described above is called weak localization. The conductivity as a function of temperature has a logarithmic character and is expressed by the eq. 2.11.

$$\sigma(T) = PL_{00}\ln(T) + constant, \text{ where } L_{00} = \frac{e^2}{2\pi^2\hbar}, \quad (2.11)$$

In the above equation the parameter  $P$  describes the inelastic scattering which also depends on the type of the interaction (electron - electron:  $p=2$  or electron - phonon interaction :  $p=3$  or 4) [24]. During this occurrence the phase coherence can be conserved and for this reason the interference can be observed for back-scattering. For this reason, the conductivity as a function of temperature decreases with decrease of the temperature. The decrease of the temperature is due to the logarithmic correction that has been discussed above. In the presence of weak localization it is possible to destroy the phase coherence of the partial wave by applying external magnetic field. The external magnetic field leads to an increase of the conductance variation as it has been observed for the (1,5) phase of Pb/Si(557) systems. However, additional scattering processes can occur, e.g.

due to the spin-orbit coupling that is characterized by the scattering time  $\tau_{so}$ . The scattering time  $\tau_{so}$  makes the eq. 2.11 invalid because the SO coupling leads to the destructive interference of the electron wave functions [25]. According to the Hikami theory, it was possible to distinguished between all above described processes. A more detailed description can be found in the [25][26] and [27].

The picture of the conductance is accomplished by including the scattering at the magnetic impurities that has been described in [28]. After including all those corrections one obtains the relation for the conductivity as a function of temperature that is expressed as shown in the eq. 2.12

$$\Delta L_{WL} = -L_{00} \left( \ln\left(\frac{B_1}{B_2}\right) - \frac{\ln\left(\frac{B_3}{B_2}\right)}{2} \right) \quad (2.12)$$

where :

$$\begin{aligned} B_1 &= B_0 + B_{SO} + B_S \\ B_2 &= \frac{4}{3}B_{SO} + \frac{2}{3}B_S + B_i \\ B_3 &= B_S + B_i . \end{aligned}$$

and according to the Hikami theory :

$$B_n = \frac{\hbar}{4eD\tau_n}$$

where n is given as follows:

$$\begin{aligned} 0 &= \text{elastic scattering due to applied electric field} \\ i &= \text{inelastic scattering due to the electron-phonon interaction} \\ SO &= \text{Spin-Orbit coupling} \\ S &= \text{scattering on the magnetic impurities.} \end{aligned}$$

## 2.2.4 Size effect

All considerations presented above dealt with three dimensional (3D) films i.e. films thicker than approximately 7 mono-layers. For the films with a thickness greater than 7 ML, the sample behaves like bulk material and the defects influence the conductance as described above. As the thickness of the film is reduced to a size comparable to the mean-free-path  $l$  of conduction electrons in this film, surface diffuse scattering has a considerable contribution to the resistivity. This effect is well known as the classical size effect and it was studied for the first time by Fuchs in 1938 [29].

### Classical size effect

Fuchs in his model was using Boltzmann's transport theory. He concluded that the resistivity of a thin film with thickness  $D$  is given by the following form:

$$\rho(D) = \rho_\infty + \frac{3}{8D} l_\infty \rho_\infty (1 - p) \quad 0 \leq p \leq 1 \quad (2.13)$$

for  $D \gg l_\infty$ , where

- $l_\infty$  : is the mean-free path of the conduction electron in the limit of  $D \rightarrow \infty$
- $l_\infty$  and  $\rho_\infty$  : are the material constants
- $p$  : is a phenomenological parameter, often called the specularly parameter
- $p = 1$  " all electrons are specularly reflected

The specularly parameter  $p$  describes the strength of diffuse scattering of the conduction electrons at the surface-vacuum interface and at the interface to the substrate of the thin film. Thus it is also called a reflection parameter and does not depend on the direction of scattered electrons. According to this theory, a fraction  $(1 - p)$  of the conduction electrons is scattered diffusively at the surface of the thin film, and thus, gives rise to an enhanced resistivity.

After Fuchs had published his theory, Sondheimer [30] developed his own extension of it, because of the fact that the general solution of the Fuchs equation is too complicated and is not complete. According to Sondheimer's extension of Fuchs' theory, from equation 2.13 one can distinguish two different transport equations with respect to the parameter  $\gamma := \frac{D}{l_\infty}$  :

$$\frac{\rho}{\rho_\infty} = 1 + \frac{3}{8}(1 - p) \frac{l_\infty}{D} \quad \text{for } l_\infty \ll D \quad (2.14)$$

and

$$\frac{\rho}{\rho_\infty} = \frac{4}{3} \times \frac{1 - p}{1 + p} \times \frac{l_\infty}{D} \times \frac{1}{\ln(\frac{l_\infty}{D})} \quad \text{for } l_\infty \gg D \quad (2.15)$$

As one can see from equation 2.14 for thick metallic films the resistivity consists of two (bulk and surface state) parts, however, the surface state factor approaches zero and the resistivity of the film is equal to the resistivity of the bulk ( $\rho_\infty = \rho$ ). For other cases the influence of a surface diffuse scattering into the resistivity. The above consideration does not distinguish between the type of surface scattering, therefore it cannot fully describe the charge transport in such systems.

After the Fuchs-Sondheimer transport model, Mayadas and Shatzkes have developed another kind of charge transport as an extension of the Fuchs model [31]. They have discussed the grain boundaries as possible scattering centers within the film. Each of the grain boundaries was regarded as a potential barrier, where

the electrons can be scattered with a probability  $R$ . From this theory, they have calculated the resistivity as follows:

$$\rho = \frac{\rho_{\infty}}{f(\alpha)} \quad (2.16)$$

where

$$f(\alpha) = 1 - \frac{3}{2}\alpha + 3\alpha^2 - 3\alpha^2 \ln \left( 1 + \frac{1}{\alpha} \right) \quad (2.17)$$

and

$$\alpha = \frac{l_{\infty}}{D} \frac{R}{1 - R} \quad (2.18)$$

In this case  $D$  is the distance between the grain boundaries. When now  $\alpha \ll 1$  the equation 2.16 can be expressed in the following form:

$$\rho = \rho_{\infty} \left( 1 + \frac{3}{2}\alpha \right), \quad (2.19)$$

this equation is similar to Fuchs' equation. It also consists of two terms: bulk resistivity  $\rho_{\infty}$  and the resistivity related to grain boundary scattering  $\rho_{\infty} \frac{3}{2}\alpha$ . The Mayadas extension of the Fuch's theory has only application for highly disordered films where the back-scattering at the grain boundaries reduced the conductivity of the metallic films to the given form. This behavior has not been observed for the Pb systems, however it completes the picture of the conductivity at the size effect regime.

### 2.2.5 Electron confinement in 1D

The above description concerns the systems that are described as 3D and 2D, where the electron distribution can be explained within the classical theory of solids and the electron transport is described by Ohm's law. For these systems the band structure has a 3 dimensional character that forms because the particles have wave-like nature and are arranged periodically due to the covalent bonding of their orbitals. This creates a periodic potential where electrons can conducted. The energies of those electrons are related to the  $\mathbf{k}$ -vector via a dispersion relation which is usually represented by the energy-dispersion curve. The wave vector  $\mathbf{k}$  is inversely proportional to the wavelength of an electron. If the crystal's dimension can be reduced to the size of the wavelength  $\lambda$ , the energy band will be affected too, in the manner, that the band structure will loose its periodic in 2 direction and keep the band structure that allows electron transport only in one specific direction. In such a situation one speaks of confinement of an electron. In other words, the confinement consists of a energy band that has been changed by reducing the dimension of the structure. This implies, that the 1D object will be defined as crystal with 2 reduced dimensions and third extremely large. This

sort of sample is normally achieved by using carbon nano-tubes or polymers [32] or [33]. To build a 1D object out of a typical metal like silver, gold or lead, a supporting substrate has to be used. Reducing the dimensions of the structure, the contributions of the surface and neighboring structure are not negligible. In this case one speaks of quasi-1D system or highly anisotropic system. In the sections below those two last examples as well as the typical effects that can be observed in 1D will be discussed.

### 2.2.6 1D system and Charge Density Waves instability

For the simplest 1D metallic structure, like an atomic chain (1 dimensional crystal with a lattice vector  $\mathbf{a}$ ), that is suspended in space, the energy dispersion has a single parabolic form that represents the occupied states as it can be seen in fig. 2.5a. Applying a voltage to such a crystal, one would obtain a current flow which can be described by Ohm's law, as it was mentioned above but only in one direction.

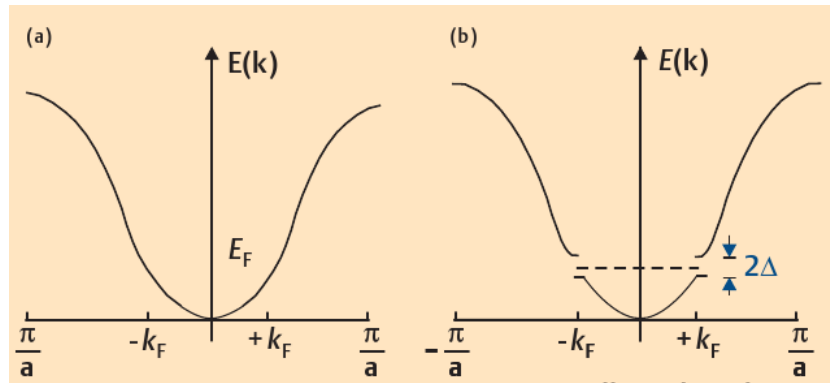


Abbildung 2.5: The band structure of a) 1D crystal b) After CDW formation.

Sometimes however, the current that is observed for such experiments is different than the Ohm's law predicts. This is usually connected with the periodic structure of the crystal that is changing with the temperature. In the normal room temperature condition, the crystal has a periodicity  $a$  and the energy band as shown in 2.5. Due to e.g. temperature lowering, the atomic or electronic configuration in the crystal lattice undergoes a reversible structural phase transition and rearrange its periodicity with the new lattice constant  $b$ . This change firstly has an influence on the band structure as it opens a band gap at the Fermi energy ( $2\Delta$ ) like it is presented on fig. 2.5b, and secondly modulates the electron distribution with a wavelength  $\lambda$  that is proportional to the inverse of Fermi wave vector  $k_f$ . This periodic electron distribution is also called a Charge Density Wave within a Peierls distortion due to electron-phonon coupling.

The modulation of the charge distribution within the anisotropic crystal that influences the electron transport was already known for many years and more detailed description can be found in the [34] where the theory of CDW has been presented. An experimental technique to achieve the periodic charge distribution that is observed as CDW can also be achieved by low coverage of a metal that is incommensurable with the structure of the surface substrate [35]. Now due to the break down of the symmetry, this structure can undergo the modulation in the density of states at lower temperatures. This is known as the ground state of the CDW. The coupling of the electrons with the phonons in the ground state results in the instability at lower temperatures that occurs as a metal-insulator transition. The character of this transition, whether it is first or second type phase transition, strongly depends on the fluctuation between the adjacent structures. Usually, the transition has characteristics of a first type phase transition if the electron density modulation is associated with the periodic change of the crystallographic structure like it was observed for the In/Si(111) system [36]. The transition mentioned above has been described for the first time by R. Peierls [37] and is named after him. The instability that has been predicted by R. Peierls is caused by the gap opening at the double of the period  $\mathbf{a}$  due to electronic reconfiguration that can be induced by e.g. dimerization (like it was observed for In/Si(111) [36]).

### **Fermi nesting**

Special case of Peierls instability can be observed if the periodic arrangement at the surface described by the vector  $g$ , the separation of the neighboring structures, can be correlated with the Fermi wavevector  $k_f$ . This instability cause a gap opening at the Fermi level as described above and the CDW ground state is reached. This results in the insulating behavior of the conductor (metal-insulator transition). This effect is called Fermi nesting because all the occupied states are nested at the Fermi energy. Such behavior is observed very often for the quasi-1D system which are due to their nature unstable. It is characteristic for this systems that electrons that are propagating in such solid due to electron-phonon interaction will undergo so called Umklapp scattering which results in insulating behavior of the system. The localization due to mentioned Umklapp process can be also correlated with the  $4k_f$  CDW phase that has been discussed in more detail in [38].





# Kapitel 3

## Experimental

In the following chapter, the vacuum chamber and the measuring equipment are briefly presented. The measurement equipment include a SPA-LEED, a cryostat, a sample holder, a superconducting magnet and a Pb source. At the end of the chapter a schematic diagram of the electrical connections for the conductivity measurements will be shown and discussed.

### 3.1 Ultra High Vacuum System

The vacuum chamber is made of stainless steel. The main advantages of making the whole chamber out of this material are the non-rusting properties of this material, the high durability and the non-magnetic properties, which are very important for measurement in magnetic field. Additionally, the steel has a low vapor pressure and a low reactivity that allows to heat the whole system up to 200 °C over days in order to reach a vacuum of  $1 \times 10^{-10}$  mbar, which is a necessary condition for sample preparation. The bake-out was performed each time after a new sample has been mounted. Because of the electrical measurements performed on the samples at low temperature, it was not possible to implement the load-lock system for faster sample exchange. A changeable sample holder would have had very poor thermal contact with the cryostat. Thus it would restrict the lowest achievable temperature to 40-70K when using liquid Helium as the cooling agent. Furthermore it would not assure a perfect electrical connection with the sample mounting.

All experiments were performed using two main chambers. The morphology investigations were performed in a first chamber with vertical manipulator mounting system. The sample holder and the manipulator were redesigned for a good sample approach during SPA-LEED measurements. For pumping the manipulator during operation, a differential pumping system was used. The whole system has been pumped by one 160 l/s of  $N_2$  turbo-molecular pump connected together with a rotary valve pump. Additionally, an ion getter pump with titanium sublimati-

on pump was used. Regular titanium sublimation and baking out the chamber allowed to keep the vacuum at the  $10^{-10}$  mbar level also during Pb evaporation. The second chamber, which possessed a horizontal manipulator mounting system,

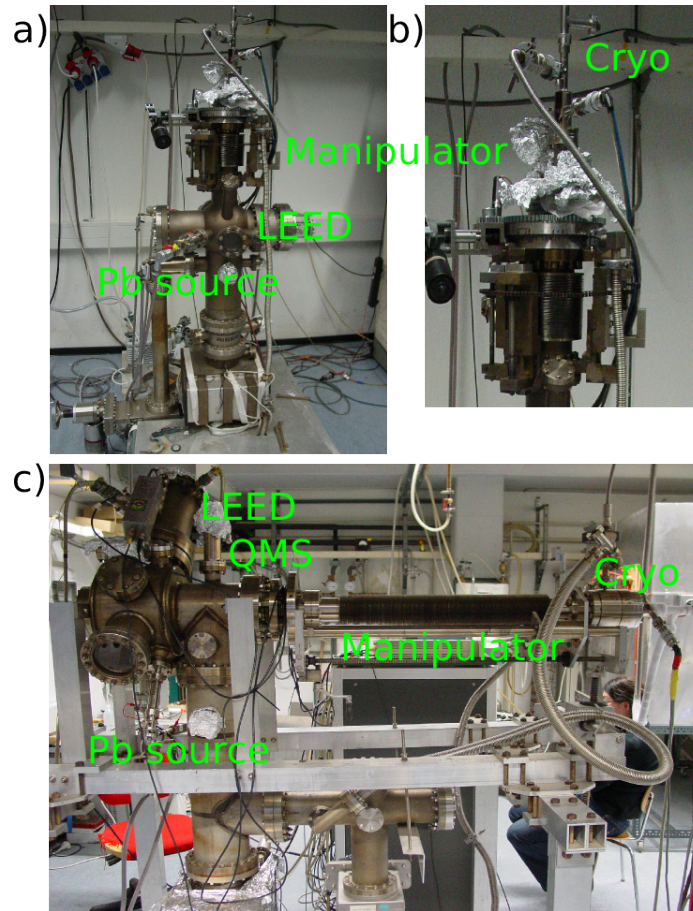


Abbildung 3.1: a) Picture of the chamber for structure measurements as well as conductivity. b) zoom-in of the Manipulator head. The electrical connections and cryostat are visible. c) chamber for conductivity measurements with and without magnetic field. For structure control, it has been equipped with LEED instrument.

was used for conductivity measurements. The horizontal position was chosen for measurements in magnetic field. The entrance of the magnet was placed in front of the magnet barrel as shown on the fig 3.1b. At the conductivity chamber a SPA-LEED was used for surface controlling.

### 3.1.1 SPA - LEED

For the surface analysis the *Spot Profile Analysis - Low Energy Electron Diffractometer* was used. The SPA-LEED instrument is a modified standard LEED

diffractometer with a built-in single electron detector (channeltron). The incident and scattered electrons are deflected by a so called octopole plate deflector. In this case the angle between the electron source and electron detector remains constant as they are mounted in a fixed manner and the angle between incident and scattered beam remains constant as well. The voltage that is applied to the octopole changes at the same time and for this same interval the incident angle and reflexion angle of the electrons. This is schematically shown on fig. 3.2a. The octopole is a system of metal plates connected by a network of very stable and precisely chosen resistors that symmetrically split the voltage on both neighbor plates. The resistors divide the voltages which are applied to the octopole plates, so that the electric field induced by the plates in the SPA-LEED instrument has a homogeneous shape. The ratio between the front and rear sets of the plates is fixed during the measurement but can be changed by the experimentalist if the focus has to be shifted. The ratio of the voltages between the front and the back of the octopole sets the focus point on the sample. By changing the voltage on the front plates one changes the ratio. In this way the focus can be shifted out of the SPA-LEED optics. In the case of a sample holder that cannot approach closer to the LEED-system, the optimal focus can still be obtained. The simulation of the electron path and electrical field distribution has been presented in the diploma thesis of Schmidt [39]. If the voltage applied to the octopole is symmetrically distributed without offset, then the (0,0) reflex is pointed to the channeltron. For standard Leybold SPA-LEED instrument, the angle between incident and scattered beam is set to  $7^\circ$ . On the picture in fig. 3.2 the schematic drawing of the SPA-LEED instrument is presented.

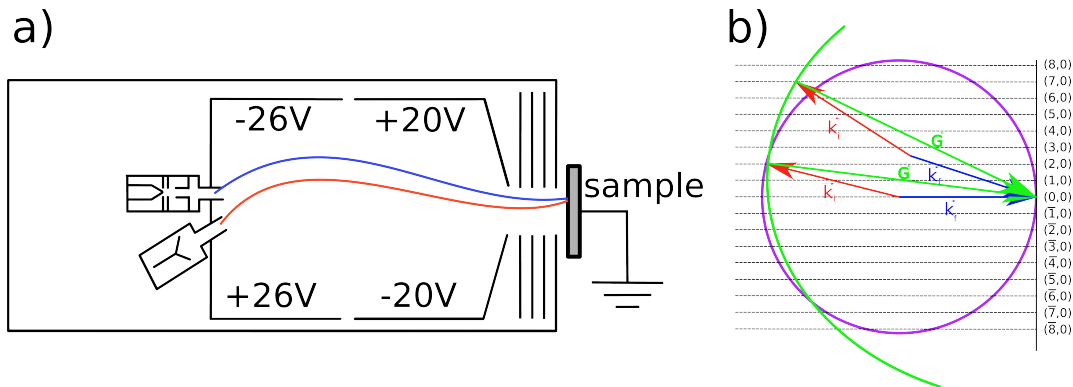


Abbildung 3.2: a) Schematic drawing of SPA-LEED instrument. The octopole plates, the electron gun and channeltron are shown. Red and blue line show possible path of the incident and scattered electron, respectively. b) Modified Ewald sphere for the SPA-LEED experiment.

To focus the electron beam on the sample a system of two electrostatic lenses is used. The lens mounted near the electron gun sets the size and the shape of the

outgoing electron beam. Optimally, the lens focuses the electron-beam coming out of the wehnelt, additionally, so that a point-like electron source is obtained. The distance to the sample is in the case of the SPA-LEED instrument set to 20 cm i.e. the distance between the electron gun and sample surface. The electron waves can therefore be treated as plain waves at the sample. Further focusing of the electron beam is done by a so called crystal lens which is built at the end of the instrument near the sample and is acting on the backscattered electron focusing them on the channeltron.

In the case of standard-optical LEED instruments, the angle between incident and scattered beams are scanned by using a large fluorescence screen right behind the electron gun which keeps the incident angle constant. In case of SPA-LEED as mentioned above, the scattered beam is pointed to the channeltron by a deflection voltage. A computer program recalculates the position into the positions in k-space and plots its intensities as a gray scale picture. The fixed angle between the electron gun and channeltron i.e. constant angle between  $k_i$  and  $k_f$  defines a new Ewald circle (in 3D scattering experiment it is a sphere but due to the surface sensitivity of LEED it is reduced to a circle) which is shown in the fig. 3.2a, as a green arc with a radius equal to  $\vec{G}$  and its center at the (0,0) rod at energy of 0[eV]. By scanning the k-space (changing the incident angle), the intensity distribution on other reciprocal rods are projected. The energy is calculated as  $k_{\perp}$  component of k-vector of the electron wave and is shown as y-axis of discussed picture. The (0,0) rod is also known as specular spot or (0,0) spot.

The instrumental resolution is described by the instrumental response function and the transfer width. The first quantity includes all the errors and inaccuracies of the electron gun, the electrostatic focus and the deflection unit. The diffraction experiment on a perfect crystal will be affected by this restrictions. The minimum of the FWHM of the specular beam is then restricted by the respons function. The transfer width, which is the coherence length of electrons, sets the limit of the structure size that can produce Bragg reflexes. For typical LEED this quantity is at the level of 20nm. As will be shown later, the FWHM is an important quantity in surface analysis. The transfer width (T) is a factor of atomic distance or the periodic structure of the investigated surface multiplied by the distance between two neighboring reflexes and divided by the FWHM of specular spot.

$T = \frac{\Delta k}{k_{01}} a_0$  where the  $\Delta k$  is FWHM of the electron beam,  $k_{01}$  the distance between fundamental spots and  $a_0$  is the lattice constant of the investigated crystal. For the standard SPA-LEED instrument the value of T is on the order of 400nm. The important information that is delivered by measuring the value of T is the size of area that reflects the electron beams coherently.

The diffraction of low energetical electrons are well described by the classical

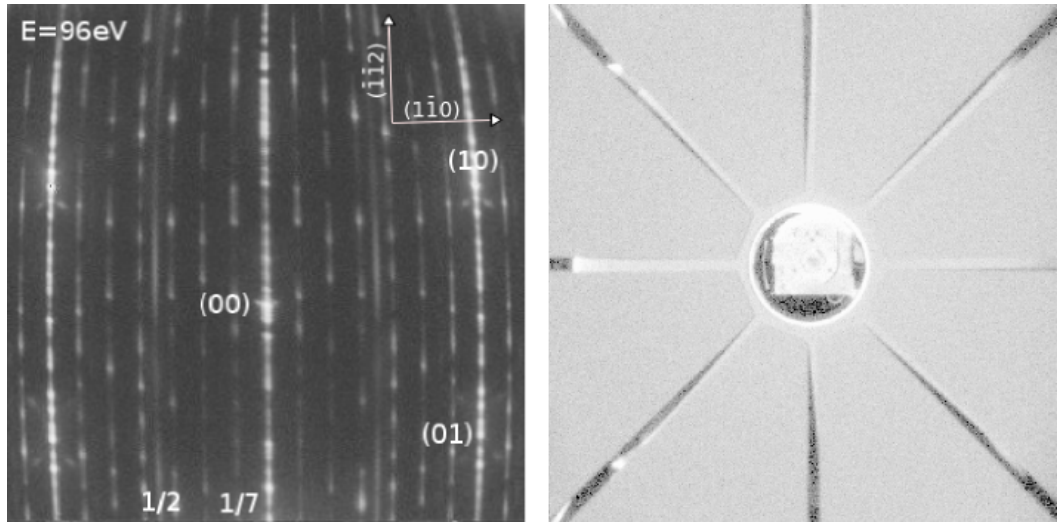


Abbildung 3.3: *Left* LEED pattern of Si(557) surface. 2D mode - reflex intensity converted to gray scale. *Right* SPA-LEED pattern obtain in real mode. The SPA-LEED instrument works as an electron microscope. The electron beam is scanning the real space.

diffraction theory. The electrons are wave-particle with wavelength

$$\lambda = \frac{h}{p},$$

where  $p$  is the momentum of the electron and  $h$  is the Planck constant. Evaluating this equation, one can relate the wavelength to the energy. Taking the energy range of 20-500 eV, the wavelength of the low energy electrons can be calculated. Following the formula:

$$\lambda = \sqrt{\frac{150.4}{E[\text{eV}]}}$$

wavelengths of 0.05-5 Å are obtained. It turns out that these values fit the average atomic distances. The diffraction of low energy electrons can therefore be performed on crystalline samples. Due to the low energy of the electrons, the penetration depth into the crystal is very low (first 3-4 atomic layers contribute to the scattering process), so that the surface sensitivity of LEED is very high. More detailed descriptions of electron diffraction can be found in the literature [40], [41] or [42].

Considering only elastically scattered electrons, the intensity of the diffracted electrons is given by the Bragg equation. The intensity which is the square of the amplitude of the scattering probability can be split into two parts as expressed

in the following equation:

$$I(k_f, k_i) = F(k_f, k_i)G(k_f),$$

where  $k_i$  and  $k_f$  are the incident and scattered wave vectors respectively and  $F$  and  $G$  are dynamic form factor and kinematic reciprocal lattice vector respectively. There are two theoretical approaches of how the LEED can be explained. The kinematic and dynamic approximation theory.

The kinematic theory, which is commonly used to interpret the LEED pattern, assumes that all the form factors are equal and only the first layer scatters the electrons. The dynamic approximation distinguishes between the form factor of the first and second layer as well as the form factors of the scatterer's unit cells. In this work mainly the kinematic approximation will be used because of the fact that the information obtain in this thesis could be well explained by this theory and secondly because the SPA-LEED instrument is too slow for obtaining dynamic information of the scattered beams. Most of the effects that have been observed are well explained within the kinematic approximation. In the case of a perfect surface, all scatterers scatter with equal probability. Now if the single atomic step is present the scattering form factor on the upper and lower terrace of the step differs. The electron beams that are scattered from the surface where two different scattering form factors are present, will have a phase difference. The phase  $S$  (integer  $S$  means in-face condition or Bragg condition) can be calculated as:

$$S = \frac{k_{\perp} d}{2\pi}.$$

Two scattered beams depending on the primary electron energy are shifted in phase while scattered from the atomic step which results in destructive interference (diffusive diffraction spots). Because the above equation presents the relation between the phase  $S$  and the perpendicular component of the wave vector  $k$ , it is possible to rewrite the formula of the lattice factor  $G$  as a function of  $S$ . The  $G(S)$  function which for multi-level system can be written as :

$$G(S) = e^{-\Delta^2(2\pi\delta S)^2}$$

has a Gaussian distribution and its  $\Delta$  factor is directly related to the vertical roughness of the surface (it is expressed in the atomic step height units; for more details see [42]). The information about lateral roughness can also be obtained. Analysis of the full width at half maximum as a function of the scattering phase delivers direct information about the size of coherently scattered object. These kinds of experiments are known as  $H(S)$  analysis and more detailed description can also be found in [42]. In the case of a well defined roughness, like stepped surfaces, an additional splitting of fundamental spots is observed. The splitting is a result of the multiplication of the Fourier transform of the superlattice (the step-periodicity) and the Fourier transform of one single terrace. Such splitting is



presented on the left picture of fig. 3.3. For vicinal surfaces all fundamental spots split up into spots with a separation( $\Delta k$ ) inversely proportional to the terrace width( $\Gamma$ ) (fig. 3.4).

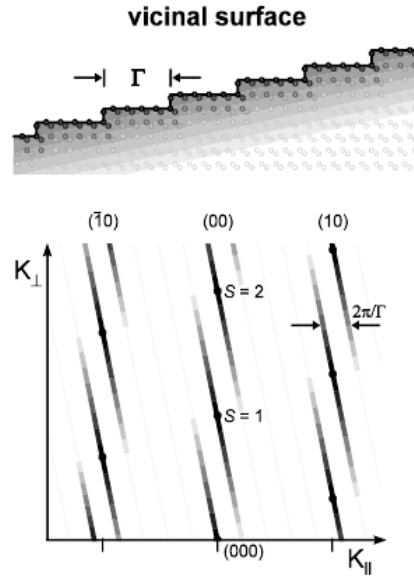


Abbildung 3.4: *Top*: Cross sectional view of a vicinal surface with a terrace width  $\Gamma$ . *Bottom*: The k-space mapping of the vicinal surface results in a fundamental spot splitting which is related to the terrace width  $\Gamma$ .

Due to the kinematic approximation, the intensity modulation of the splitted spots can be expressed as

$$A(k) = \frac{\sin^2(\frac{N}{2}ka_0)}{\sin^2(\frac{1}{2}ka_0)}$$

[42]. Observations of this kind of surface with a LEED instrument result in spot movement while the energy changes. This kind of experiment requires an optimal focus setting to perform such intensity measurements without changing the position of the sample and focus parameters. The optimal focus is achieved by setting the sample position and configuring the electrostatic lenses this way that for various energies the spots are only instrumentally broadened and the specular beam remains at a constant position. These kinds of measurements were often performed for the Pb/Si(557) system to obtain information about re-faceting of the surface.

### 3.1.2 Cryostat

During all experiments, the sample holder was cooled down to either liquid nitrogen or liquid helium temperatures. Low temperatures during operation were necessary due to the presence of temperature sensitive elements and sensors. The electrical connections to the sample were made via very thin copper wires, which were electrically isolated by polyimide film ("kapton" ©). This material has thermal stability up to 400 °C. Also the temperature sensor (commercial Si diode - LakeShore) has its thermal stability below 500K. All of those elements had to be kept at low temperatures during experiments. To ensure this condition, a continuous flow cryostat was mounted on the manipulator. The thermal contact between the tip of the cryostat and the sample holder was made through a copper stamp which has been built between them. To increase the contact surface of the junction, a thin indium layer was printed on the stamp. Additionally, several bridges were mounted for cooling the electrical connections to the sample. The single bridge was made of a copper ring that had two flat outer surfaces covered with small sapphire plates where the cords were glued. The flow of liquid gases was adjustable via a liquid gas valve operator which opens and closes the valve on the bottom of the liquid gas dewar. The flexible transfer line has been isolated via high vacuum reservoir around the transfer line. The cryostat used for the experiments also had a built-in heater on the cryostat finger, for temperature regulation during warming up and cooling down the sample. For this procedure an electronic equipment with a built-in PID regulator and a high precision DC-power supply which are controlled over a GPIB interface were used.

### 3.1.3 Sample holder

The sample holder was screwed in on the UHV side of the cryostat. As it was mentioned above, the heat exchange between the cryostat and sample holder was realized over a cold finger on which the sample holder has been fixed. The shape of the sample holder has no sharp edges to assure homogenous heat distribution over the whole holder and good heat dissipation. The sample mounting fingers were made out of tungsten foil and were itself mounted on two sapphire plates which isolated the sample against the sample holder electrically but at the same time ensure a good thermal coupling of the sample to the cryostat.

The circled tungsten filament for e-beam heating has been mounted behind the sample. In Fig. 3.5 the schematics of sample holder are shown.

The electrical contacts were made of very thin W-clamps. The clamps held the sample on the W-fingers as well as connected electrically the other for  $TiSi_2$ -contacts. The contact-clamps A,B,E and F (as shown on fig. 3.7b) are joined electrically with the fingers over a thin wire (0.1 mm in diameter). The thickness of the wires assures the thermal resistance from the plug side of the whole cryostat to be high. As mentioned in the section 3.1.2, between the plug and the sample



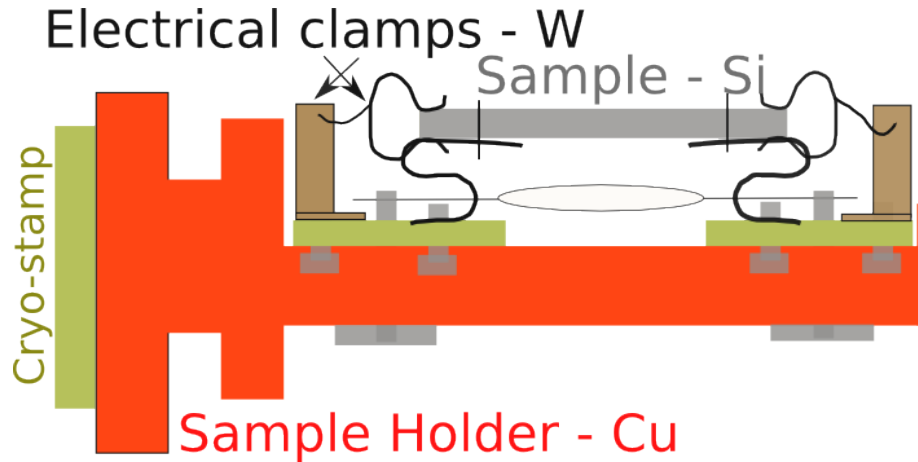


Abbildung 3.5: Schematic of the Sample holder.

holder, the electrical cables were pre-cooled by bridges mounted on the vacuum side of the cryostat. Those bridges were sufficient to assure heat exchange between the wires and cryostat during LN-cooling. At 4K the heat transport over the cables was too big to keep stable temperatures at the sample. For this reason, the last few centimeters of the cable had been made of very thin wires (around 0.1mm in diameter) to increase the heat resistance to the sample. For a better cooling efficiency at LHe<sub>2</sub> operating mode, the sample holder has been shielded via a copper cylinder which is in thermal contact to the cryostat. The surface of the cylinder is covered with a very thin gold film to reflect any radiation from outside (e.g. visible or infrared radiation *etc.*). The sample connection and mounting is described in more detail in section 5.1.

## 3.2 Lead Evaporator

Pb has been evaporated out of a ceramic crucible by heating the ceramic pipe with a filament wrapped around it. The crucible was filled with Pb wire of a very high purity (99.998%). The filament was always warmed up for a certain time to assure the thermal stability of the surrounding and therefore a constant evaporation rate. As shown in Fig.3.6 the crucible and the filament have been placed within a copper cylinder which is connected to a water-cooling pipe. During the operation, the Pb source has been cooled by a constant water flow. In front of the evaporator, a copper screen was mounted. The screen was meant to conceal the light coming out of filament and to mount the quartz micro-balance for flux monitoring. Additionally, the chopper has been built-in to shadow the sample during warming up or degassing and for starting evaporation. After the warming up, evaporated material reaches the temperature of around 600K at the pressure

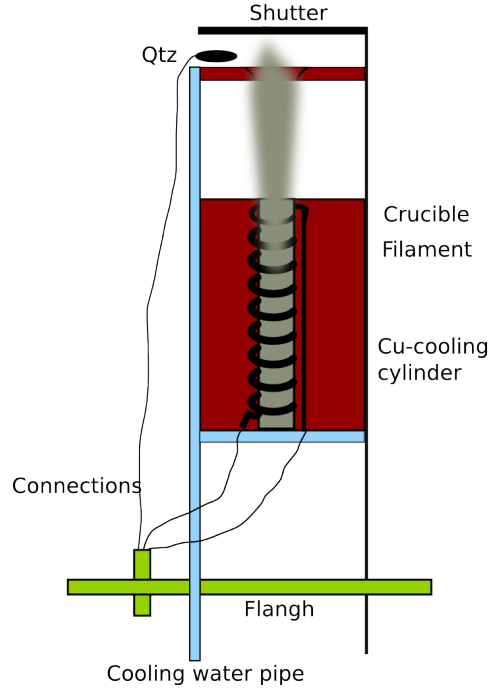


Abbildung 3.6: Schematic of the Pb-source.

of  $2-3 \times 10^{-10} \text{ mbar}$ . At stable temperatures also the quartz micro-balance reaches the thermal stability and the constant flux of lead could be measured. The amount of lead per time unit was calculated from the frequency drop of the 10MHz quartz. The frequency drop is proportional to the density of the atomic mass evaporated onto the surface unit cell of the quartz. The proportionality factor is so called quartz constant and is equal to  $3.764 \frac{\text{Hz}\text{\AA}^2}{\text{amu}}$  From this follows Eq. 3.1:

$$\Delta f = C_{Qtz} \rho \quad (3.1)$$

where  $\rho$  is the atomic mass density given by the atomic mass per surface unit cell. The obtained value has to be corrected by the geometry factor which is given by the ratio of a square of the distance between the crucible and the sample and the distance between the crucible and the quartz. For every system this factor is constant and has to be calculated only once. For the Pb-evaporators used in this thesis  $\Delta f$  was estimated to be 500 Hz per atomic layer. The calculations of the evaporation rate was then calibrated by measurement of the TCR factor of the evaporated mono-layer according to 3.2.

$$TCR_{Pb} = d \cdot \frac{dR}{dT} = 75 \frac{n\Omega \text{cm}}{K} \quad (3.2)$$

To estimate the TCR factor, an atomically flat film of at least 10 Pb-mono-layers had to be prepared. After warming up to a temperature of about 160K

and cooling down again, the Pb-film shows bulk conductivity without healing effects. Adsorbing on top of such a film another mono-layer (epitaxial system - layer-by-layer growth) results in a constant decrease of the sheet resistance. After a certain amount of Pb evaporated on such a system, the resistance has been measured as a function of temperature. According to the Eq. 3.2 the change of the resistance  $dR$  is proportional to the inverse of the Pb-film thickness. The quartz can be calibrated by comparing the frequency difference to the film thickness  $d$  calculated from the eq.3.2.

The calibration has been performed every time a new evaporator has been used or its position was changed and repeated a couple of times to ensure the stability of the source. The stability of the source during different fluxes has been tested as well. The minimal stable flux achieved by this kind of source has been estimated to be 0.01ML/10sec. Minimizing the filament current to achieve lower rate results in lowering the crucible temperature. At this condition, the lead temperature is much too low for sublimation and either no flux could be measured or the deposited amount of lead was not reproducible.

### 3.3 Conductivity measurements

The most important and difficult part of the experiments were the conductivity measurements performed on the samples which were prepared the way described in chapter 5 and placed in the UHV chamber. The difficulty of these measurements lies in the contact stability in the temperature range of 4-1100 K as well as in the sensitivity of the system towards the temperature gradients and current level. Also the Pb deposition on the sample during evaporation is an important factor. Because of the 1D- and 2D-character of the conductivity measurements performed on the Pb/Si(557) systems, also the type of measured conductance had to be taken into account. In addition the conductance of the silicon surface has always a contribution of the silicon bulk and is also influenced by surface states. This fact requires different techniques for conductivity measurements that exclude errors coming from the system like, for instance, contact resistivities. In this chapter the techniques of two-, four- and eight-point measurement will be described.

#### 3.3.1 Two-point measurements

The conductivity measurements performed by the 2 point configuration are the most commonly used. The diagram of the configuration is presented in Fig. 3.7a. Direct current is applied to the sample via two electrodes. The voltage drop measured between those two electrodes is proportional to the resistance of the sample. The main disadvantage of the 2-point measurement is that the resistance measured from the  $\frac{U}{I}$  includes also the resistance of the contacts and cables that are connected. It is not possible to measure the sample's resistivity correctly

without the precise knowledge of the contact-resistivities. The only solution for reducing their influence on the measurements is to choose a sample with a resistance much higher than the contact resistance. Nevertheless the values of the contact resistance were obtained by placing two electrodes on the contact itself (contact - black triangular form on the edge of the sample as shown on the fig.3.7b). This measurement was confirmed afterwards when the sample was coated with a thick Pb film. The advantage and main sense of this kind of measurement is the simplicity and for this reason the speed with what the measurement can be performed. The 2-point measurement was only performed during the evaporation of Pb, where the precision of the measured resistance does not matter. What you get is a qualitative measure to assure that all the contacts are covered by lead during evaporation and that the film is homogeneous and closed.

However, due to the high resistance of the silicon at low temperatures and the relatively low influence of the first mono-layer of Pb on the surface conductance or high defect concentration within the Pb film during evaporation 2-point measurements gave interesting results, e.g. the conductance oscillation measured during evaporation of the first five Pb mono-layers or the observation of the percolation limit *see chapter 5*.

### 3.3.2 Four - point measurements

A more precise measurement is performed by a four contact configuration. The conductivity measurement made by a 4-point system has several advantages. The first and most important feature of the 4-point measurement is the fact that this measurement is not influenced by the resistance of the contacts no matter if the contacts are Ohmic or not. The most popular 4-point configuration is presented in Fig. 3.7b where the contacts are arranged along one line. This configuration is commonly used to measure the so-called sheet conductance. The sheet conductance is a two-dimensional conductance of the surface that is measured in units of Siemens ( $1S = \frac{1}{\Omega} = 1\frac{A}{V}$ ). The requirement for this sort of measurements are point-like contacts. The two electrodes, where the voltage drop is measured, are connected to very small metallic patches evaporated on the sample. Their size is very small in comparison to the large size of the sample and big distance between them, those two inner electrodes can be described as point-like contacts. The realization of point-like junction between the substrate and the contact is done by the generation of silicide spots with well known geometry placing the wires that make electrical connection to the voltmeter. Another possible solution for point-like contacts would be the use of a 4-point probe STM system. However, this system has not been used within the scope of this work so it will not be discussed. However, it is worth to mention that it is the most surface sensitive method for conductivity measured presently [43]. The current supply electrodes are of arbitrary form because they are only used to supply current. Of course, the current that will be applied to the outer contacts is much easier to control

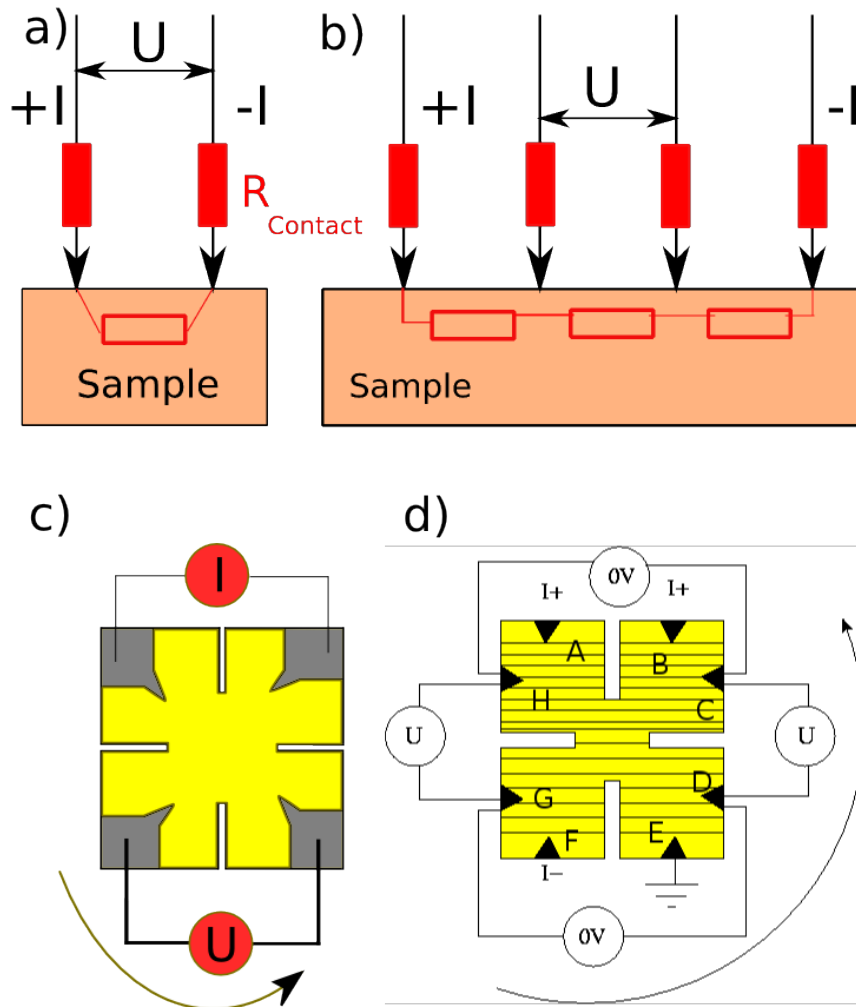


Abbildung 3.7: a) 2-point conductivity measurement. The voltage and the current are applied to this same electrodes. b) 4-point configuration. The voltage measurement is not influenced by the current electrodes. c) The configuration suggested by Van der Pauw. The advantage over other configuration is independency of the sample size. d) Sample connections for the 8 Point configuration. It is a combination of 2 Van der Pauw systems. Explanation is given in the text.

than the applying constant voltage to the sample instead, that changes its resi-

stance during measurement. The precision is only limited by the current source that has a certain resolution (in the case of our experiments, the resolution of the variable DC-current sources had two regimes  $40 \mu A$  and  $1mA$ , both with 16 Bit resolution). The uniaxial four point measurement has an advantage that it is not dependent to the same extend on the form of the sample. The situation could possibly be different (and the influence of the sample could have crucial impact onto measurement) for measurements performed on very thin films where the conductivity of the investigated structure is comparable with the conductance value of the substrate. Another possible case would be the micro 4-point measurement where the current is applied to the micro-contacts on the sample that has size in mm. The current path is then integrated over the line that are radially coming away of the patch. However, for the measurements performed on the Pb/Si(557) samples neither case had to be taken into account because the current leads were placed on the edge of the sample (for making the contacts point-like as mentioned above).

A different form of the 4-point configuration has been suggested by van der Pauw [44]. He concluded from the solution of the Poisson equation for a two-dimensional lamella, that the resistivity is independent of the size and shape of the measured object and depends only on the thickness of the lamella. The only requirements to the system are that point-like contacts are placed on the edge of the sample which itself has to be closed in the mathematical sense. Such a Van-der-Pauw-configuration is shown in fig. 3.7b (lower picture) after one chooses any four of the eight presented contacts and applies some current between two of them and measures the voltage between the two other contacts. The conductivity of a layer can be determined by performing two measurements with a cyclic commutation of the contact arrangement in between. Using these two values, let's call them  $R_{AB,CD}$  and  $R_{BC,DA}$  and a factor  $f$  that includes all the other imperfections, like contact form, sample size, finite distance between the contacts etc... <sup>1</sup> the conductivity of the sample  $\rho$  satisfies the condition:

$$\rho = \frac{\pi d}{\ln 2} \frac{R_{AB,CD}}{R_{BC,DA}} * f \quad (3.3)$$

The factor  $f$  has an exponential form and is derived by solving the Ohm's law for the configuration discussed above in this subsection. From the calculation that has been presented in [44], it turns out that in case of contacts that are point-like the  $f$  factor is equal 1 and thus neglectable. The 4-point measurements have been used for conductance measurement on thin Pb films with and without magnetic films. With this method also the phase transition driven by temperature and the

---

<sup>1</sup>for the samples used in this experiments the factor  $f$  has been chosen to be 1 and always constant because the sample has been structured always with the same procedure as described in the chapter 5.

temperature dependence of conductance for all discovered phases of Pb/Si(557) have been measured.

### 3.3.3 Eight-point measurements

The conductivity measurements performed on large samples are always influenced by the temperature gradient across the sample. To avoid the voltage offset that is due to the temperature difference between e.g. left and right side of the sample a special combination of 2 of 4-point Van der Pauw configurations was developed. The sample connection and measurement principle is shown in Fig. 3.7b. The current is applied at two upper contacts and is taken off on the bottom of the sample at contact that one is grounded and the second is connected to the negative tap of the power supply. The contacts, that were prepared on the same side of the sample, have been separated by a slit to assure no short-circuit between both electrodes. The electrical separation of the contacts allowed to split the current that has been sent through the sample. In this case, the middle of the sample has been treated as Kirschhoff's junction and the current that has been used to calculate the conductivity, it was the current flowing through the sample. The currents that were pointed towards the middle of the sample, were applied from two independent DC-sources, that had common terminal connected to ground. On the upper contacts (A and B) the positive current was applied and on the left lower contact (contact F) the negative electrode of the third DC-power supply was connected. The right lower contact (contact E) was grounded. As mentioned above the current that flowed through the sample has been calculated according to the Kirschhoff's laws. The right upper contact (B) and left lower contacts (B) were connected to the current source that could supply variable current values. The current on those contacts was changed until the voltage measured between left and right side of the sample (pairs of contacts C-H and D-G) was close to zero according to the precision value given at the beginning of the measurement. The full symmetrization has been accomplished when the potential difference between those contacts was minimalized. The measurement of the voltage drop on the sample was performed between the contacts C-D and H-G. To be able to measure the conductivity also in the direction perpendicular to the initial configuration, the connection system was then turned around by  $90^\circ$  and the symmetrization procedure was repeated. Using this technique one is able to put current homogeneously through a very large area in one specific direction. In case of a vicinal surface, where the direction of the measurement is important, this setup allows to fully control the current direction. Also, the offset caused by the thermo-voltage could be reduced to be nearly zero. With this technique, very precise conductivity measurement of the Pb/Si(557) has been made. The disadvantage of this technique is that all 8 contacts have to have comparable quality what in case of Si(557) has not been a trivial thing due to the difficult connecting and larger temperature range that contact had to stand. The imperfection

of a contact results in the unstable behavior during temperature change of the sample. The bad contacts that has non-Ohmic character influence the symmetrization which is based on the Ohmic behavior of the voltage-drop across the sample causing increase of the applied current. As it has been mentioned, the symmetrization had to be performed to increase the accuracy of the conductivity measurement. To assure quick adjustment of the current applied to the contacts B and F, the symmetrization procedure has been developed. The voltage that occurs across the sample can be converted into current assuming the resistivity value of the sample at certain temperature. This value had to be subtracted from the applied current. The described procedure was repeated until the considered voltage was measured below a given precision.



# Kapitel 4

## Silicon (557)

### 4.1 Silicon Bulk

Silicon is one of the most popular semiconductor material. In the undoped state, the band gap has an energy of 1.14 eV. The silicon crystal has a very low reactivity, and this makes it suitable for use as a substrate for epitaxial growth of metals (e.g. for studying transport in thin metal layers). It has a diamond structure which is a composition of two fcc-structures shifted along the cubic space diagonal by a vector  $(\frac{1}{4}, \frac{1}{4}, \frac{1}{4})a_0$  from its (000) position. Every silicon atom has four valence electrons and is bound to four neighboring atoms by a  $sp^3$  tetrahedral bonds. In Tab. 4.1 the some important chemical and physical properties of a silicon mono-crystal are listed:

Chemical properties		Physical Properties	
Electronic configuration	$1s^2 2s^2 2p^6 3s^2 3p^2$	Melting Point	1,683.0 K
Density	2.33 g/cm <sup>3</sup>	Boiling Point	2,630.0 K
Covalent Radius	111.0 pm	Electro-negativity	1.91
Ionic Radius (Charge)	40.0 pm (+4)	Electron affinity	-134.0kJ/mol
Atomic Radius	110.0 pm	1 <sup>st</sup> Ionization energy	1574.58 kJ/mol
Mass	28.0855 u	2 <sup>nd</sup> Ionization energy	3226.44 kJ/mol

Tabelle 4.1: Some chemical and physical properties of Si

The silicon crystals can be cleaved along the following three crystallographic axis (100), (110) and (111). Although the silicon (100) surfaces are widely used for industrial applications, the silicon (111) is often used for scientific experiments because of its unique electronic and crystallographic properties. During the last few years the Si(111) surface become especially popular as a substrate material for the growth of thin metallic films. As a function of the miscut angle these

surfaces can be used to form 2d or even 1d metallic structures showing interesting physical effects like Peierls transitions, Charge Density Waves etc. One of the best investigated systems might be the In/Si(111) system. The In- chains undergo a Peierls distortion as seen by LEED and STM. Furthermore, the signatures of a CDW has been measured also by ARPES. Further applications of Si(111) can be achieved by using silicon surfaces with certain miscut along the direction specified by the vicinity. Those surfaces are decorated by regularly distributed atomic terraces and due to that fact can be used as a matrix for growing 1D objects. In the following sections the silicon(557), silicon (223) and other vicinal surfaces will be presented.

## 4.2 The vicinal silicon (557) surface

The Si(557) is a vicinal Si(111) with a miscut angle of  $9.54^\circ$  with respect to the [111] direction. Instead of an homogeneously terrace length distribution with an average terrace length of  $5\frac{2}{3}a_{Si}$  i.e. 1.92 nm (cf. with lower part in Fig. 4.1), the surface undergoes locally a refacetting. The new periodicity yields 5.7nm, i.e. basically three former unit cells are rearranged into a (111) and (112) facet structure that alternate over the whole crystal as visible STM shown in the fig.4.1. The gray stripes are the silicon (111)-terraces with weakly visible characteristic (7x7) reconstruction. Due to the size of a terrace only the half of the (7x7) unit is presented. However, the (7x7) reconstruction minimizes the surface energy is therefore the driving force for the refacetting of the clean Si(557) surface.



Abbildung 4.1: Si(557) imaged with STM. Periodic arrangement of alternating (111) terraces and (112) facets as suggested by Kirakosian *et al.* [12]. The size of one unit is 5.7 nm i.e. 17 atomic units.

The (112) facets are build of three Si double-steps with the step-step separation of 0.88nm corresponding to the  $2\frac{2}{3}a_{Si}$  surface lattice constants. At first this model has been introduced by Kirakosian *et al.*[12] who suggest that the surface consists of alternative order of a single (111) facets (9 atomic row) and (112) facets with periodicity listed above. The atomic structure of one unit cell of Si(557) is shown in the fig.4.2.

The most interesting part of the Si(557) structure is the atomic arrangement of the (112) facets which will be discussed in more details below in this section. Many experimental and theoretical attempts are made nowadays to explain the

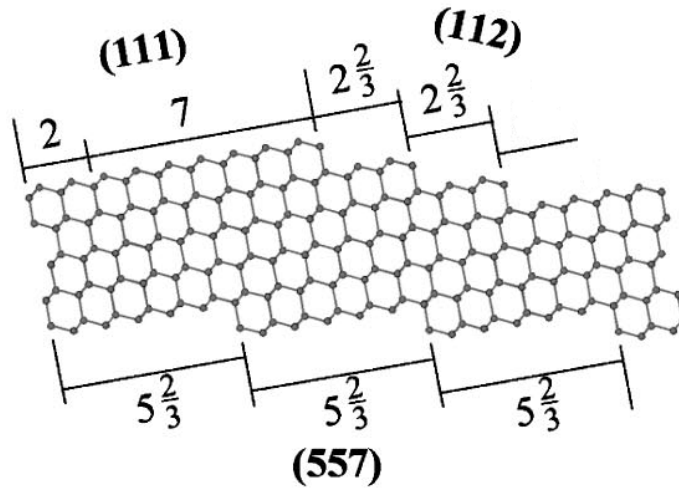


Abbildung 4.2: Side view of Si(557) unit cell. The lower part of this graph shows the equally stepped (557) surface orientation, which is only metastable.

origin of this specific reconstruction in greater detail. From an experimental point of view, the direct inspection with a STM tip is rather difficult due to the small size of the (112)-facets. Nevertheless, recently J.R. Ahn *et. al.* [45] successfully resolved protrusion of (112)-facets on the atomic scale with the STM tip. This group also suggested and discussed the model that has been postulated from first principles calculations and data achieved from angle resolved photoemission spectroscopy of Si(557). The model found by this investigations suggests that an adatom-parallel dimer model with a missing dimer with the bounding network as the Si(111)7x7 surface is the most stable.

Further, the model suggested by Kirakosian [12] and later discussed by Ahn [45] by means of theoretical calculation, ARPES and STM measurement can be confirmed by SPA-LEED measurements which have been performed within the scope of this thesis. In fig.4.3 the usual LEED pattern of clean Si(557) is presented. The 1x1 structure of Si(111) is easily seen. Additionally, the (1x1) structure is superimposed with characteristic step-train reflexes originating from the scattering with respect to the large Si(557) unit cell. Indeed, the (1x1) reconstruction of Si(111), which is equal to the Si lattice constant is split into 17 equal distances (16 spots between the (00) and (01) spots).  $17 \times$  Si lattice constant is equal to  $5.7 \text{ \AA}$ . The spots of the 7x7 reconstruction are elongated in the direction  $(\bar{1}12)$ . This is due to the fact that the single (111) terrace has a finite width. This means that the periodic correlation on the terrace has also finite length. This and the fact that one terrace does not correlate with its neighbors (there are shifted in phase with respect to each other) are responsible for the spot elongation in this direction.

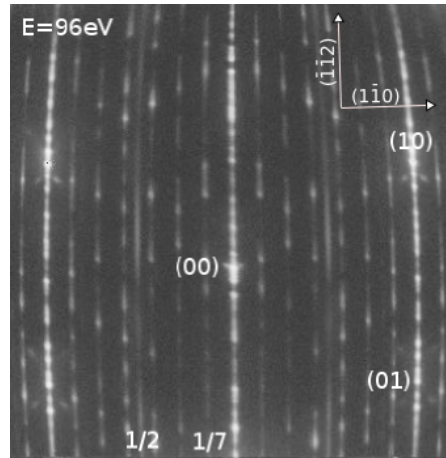


Abbildung 4.3: LEED pattern of clean Si(557) taken at electron energy  $E = 96\text{eV}$  i.e.  $S = 5$  for Si(111). Characteristic step train reflexes, elongated (7x7) spots and (2x1) reconstruction. Further explanation *see text*.

Another feature of a Si(557) diffraction pattern is the 2x1 reconstruction which shall be discussed in the following. In the LEED pattern, the (2x1) superstructure is visible as long stripes between the 3<sup>rd</sup> and the 4<sup>th</sup> reflex of the (7x7) structure. As suggested above, the (2x1) structure originates from the dimerization of the Si atoms at step sites. In the recent study carried out by group of Ahn *et al.* two different dimer configurations have been discussed and the atomic resolution of protrusion of (112) facets was successfully imaged. From their study they conclude that the protrusion of (112) facet has a  $\times 7$  reconstruction in the direction parallel to the step edge and it is composed of two rows of bright protrusions. Those protrusions were located at the step edge and within the terrace. From the geometry of Si(111)7x7 structure, the  $\frac{2}{3}a_{Si}$  broad terrace of (112) facet has to consist of one atom at the step edge. The second and the fourth atoms which are located within the terrace move downward along the  $[\bar{1}11]$  direction.

### 4.3 Other vicinal silicon surfaces

The vicinal of a silicon surface can be tuned by variation of the miscut angle. Next to Si(557) also Si(223) and Si(779) surfaces have been used for the experiment with Pb. In particular, the Si(223) orientation is interesting as the Si(557) surface undergoes refaceting upon the adsorption of Pb (see chapter 6). The Si(223) with miscut angle of  $11.4^\circ$  should give ideally a regularly stepped surface with an average terrace width of  $4\frac{2}{3}a_{Si}$ . The Si(223) has been prepared using this same method as Si(557). Unfortunately, the Si(223) surface seems to be only metastable, because strong refaceting has been observed after flashing the samples.

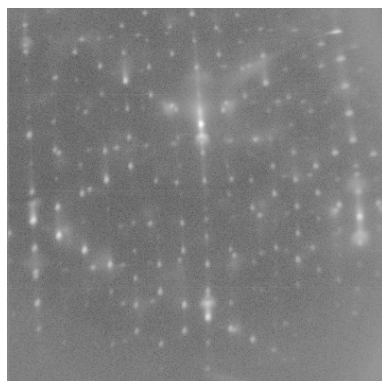


Abbildung 4.4: The LEED pattern of Si(223) taken at 80K for primary electron energy of 99.6 [eV].

Although the samples were clamped in a similar way than the Si(557) surfaces, residual stress by the clamps may cause this instability. A typical LEED picture of Si(223) is presented in Fig.4.4, taken for 96 eV primary electron energy and at the temperature of 80K. The picture shows a very strong signal of Si(111) surface with its characteristic 7x7 reconstruction and weakly visible (5x6) periodicity on top. The strong signal of large Si(111) traces indicates the mentioned refaceting. The lack of the anisotropic character (like in case of Si(557) ) can be explained by local distribution of vicinal crystal dominated by larger Si(111) terraces. But due to the lack of Pb the surface was unstable and the vicinal profile could not remain. The silicon crystal with (779) orientation have much wider terrace width and the effects that had been observed on Si(557) could not take place.



# Kapitel 5

## Sample preparation and characterization

In the following chapter the preparation of the clean Si samples and of the contacts for electrical measurements shall be presented. The first part deals with the ex-situ preparation of  $TiSi_2$  pads on the Si(557) substrate while in the second part their electrical characterization is more closely inspected. Finally, in the third part, the adsorption of thicker metallic films is characterized by transport measurements as well in order to check the homogeneous evaporation and the contacts. Technical details about the transport measurements can be found in chapter 3.3

### 5.1 Preparation of Si(557) and $TiSi_2$ -contacts

The sample has been cut into small pieces out of a 4 inch industrial wafer. Since surface transport measurements are performed a special geometry of the samples is needed. In order to protect the sample surfaces against contamination during the laser-cutting process, the samples were covered with PMMA (poly(methyl 2-methylpropenoate) plastic (synthetic polymer of methyl methacrylate) - acid). Usually, PMMA is widely used in the semiconductor industry for electron beam lithography. Its advantage in comparison to other protecting materials is its easy handling and removing as well as its stability during mechanical treatments. Moreover the PMMA is inert against humidity. The wafers covered by PMMA were cut with a laser from Meko company located in Sarstedt near Hannover. After the laser cut, the dimension of the sample was  $15 \times 15$ mm and it had four characteristic slits on every side as shown in Fig.5.1. The slits were necessary to prevent charge flow on a side of the sample between two neighboring contacts. The length of the slits is 4 mm which reduces the effective area of the sample to around  $150\text{mm}^2$ . However, this area is large enough for LEED investigation as well as conductivity measurements. According to the principle of Van der Pauw

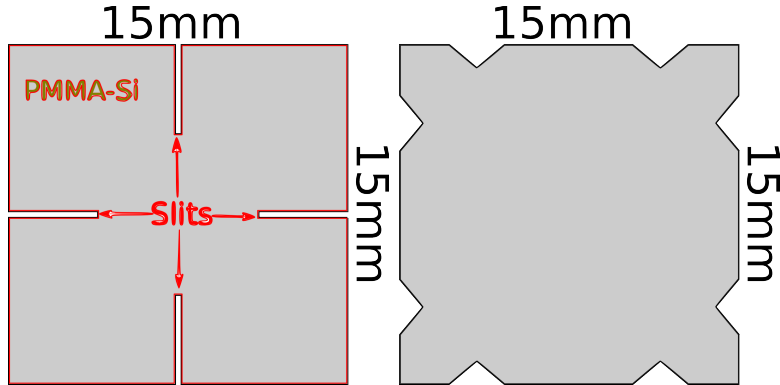


Abbildung 5.1: Schematic of the Si-sample *left* after the cutting process and removal of the PMMA. *right*: Mask used for Ti evaporation on the Si samples. After annealing to 870K stable and metallic  $TiSi_2$  contacts are formed.

method [44], the contacts have to be point-like. To achieve this requirement, a molybdenum mask has been prepared with 8 triangular cuts on its edges (*see* fig.5.1). The mask has been made with the laser beam cutting as well, to ensure that the shape of the  $TiSi_2$ -pads are as perfect as possible. The mask has been placed on top of the sample during Ti evaporation.

After cutting the samples were cleaned chemically again. The chemical preparation has been performed in a flow-box equipped with highly purified chemicals. The following methods were developed especially for this kind of samples by modifying the parameters of the chemical concentration for the used solutions as well as the time and the temperature for every step performed during the cleaning procedure.

Before evaporation the remaining PMMA was removed with acetone in ultra-sonic bath for around 5 min followed by 5 min ultra-sonic bath in purified water. In the next step hydrofluoric acid (HF) was used to remove the native oxide, but only at those parts of the sample where the  $TiSi_2$ -contacts were going to be evaporated. The duration at which every corner of the sample had been exposed to 1% HF-solution had been empirically estimated and set to 45 sec for each edge of the sample. During this procedure, the center of the sample was kept away from HF-solution. This ensures that the central part of the sample was protected during the Ti-evaporation. The native oxide is a perfect protection for any carbon contamination which is not desired on the sample during further preparation and it is a protection against  $Ti$  atoms as well.

In early experiments, the samples were treated with  $H_2SO_4 + H_2O + H_2O_2$  (in 5:6 ratio) solutions (piranha) to remove any carbon contamination. This step was skipped as soon as it was seen that piranha solutions etch silicon steps effectively as well, causing the formation of large Si(111) areas. This in fact destroyed the vicinity of the Si(557). The step of piranha was followed by HF-tip to remove



any remaining chemical contaminations. Thereafter, the oxide has been rebuilt again by ultra-sonic bath in the so called CP1 solution ( $HCL + H_2O_2 + H_2O$  (in 1:1:6 ratio)) at  $60^\circ C$  for 10 min. However, these steps disturb the order of Si(557) and additionally increase a risk of contamination of the sample.

The sample prepared for LEED experiments (where no conductivity experiments were performed) were cut out from a thin wafer ( $450\mu m$  thick) with a standard diamond cutter and cleaned only with purified acetone to removed the dust before being placed in the UHV-chamber. Those samples were prepared by a technique called flash-cleaning widely used in research laboratories for sample preparation. Details about this procedure are described in chapter 3.1.

In order to demonstrate the effect on the sample due to the wrong preparation (slightly contaminated chemicals, bad pressure during flashing etc.) LEED patterns of two surfaces are presented in Fig.5.2. More details about the silicon LEED diffraction patterns are given in section 4.

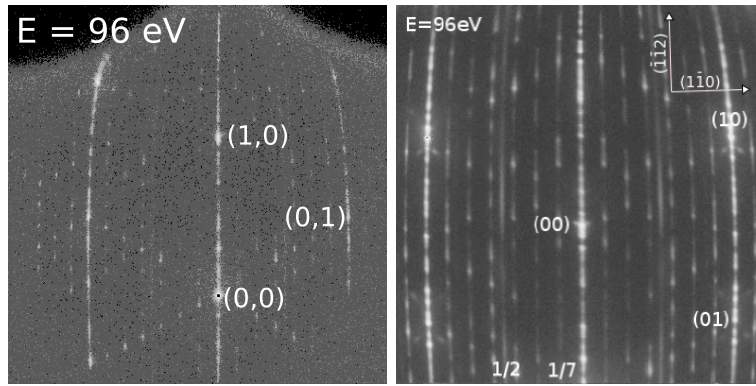


Abbildung 5.2: *left* LEED pattern of an imperfect Si(557) surface. The picture shows high level of noise signal and very sharp (7x7) reconstruction. (*right*) LEED pattern of an ideally stepped Si(557) surface. High anisotropic features of vicinal surface indicated by step train reflexes, elongated (7x7) reconstruction, low signal/noise ratio and high intensity of the (2x1) reconstruction.

The LEED pattern of the refaceted surface (left of Fig. 5.2) is showing a low signal-to-noise ratio, indicating a high roughness of the surface. Also the spotty reflexes of the (7x7) reconstruction indicate the existence of large (111) terraces. Contrary, the perfect LEED pattern of the Si(557) shown in the right part of Fig.5.2 these signatures are not visible, but the anisotropic features of the reflexes appeared. For greater reproducibility of the results obtained on the investigated structure, the quality of the silicon substrate was always taken into account, because the transport measurements are performed on a macroscopic scale.

After cleaning the samples in the way described above they have been placed into a high vacuum chamber. The top of the sample has been covered with the mask

and placed on an additional silicon piece which is electrically contacted for direct current (DC)-heating. The mask and the sample were clamped together to avoid the shifting of either the sample or the mask. The contacts have been evaporated from a Ti wire (0.25mm in diameter) by putting exactly 2.01 A for 15 min while the sample was heated up to 650°C. After 15 min the wire burned through and the amount of Ti evaporated onto the uncovered Si surface corresponds to round about 100 nm as checked with AFM and STM. By applying temperatures around 920K to the sample, the silicide process is enabled. After the wire burned through, the sample has been post-annealed for another 30 min to make sure that all the Ti atoms reacted with underlying silicon. The thin oxide layer remaining after HF-treatment (*see above*) protect the silicon from uncontrolled oxidation in air during sample mounting and was completely removed at that temperature allowing Ti to react. After Ti evaporation the sample had 8 characteristic triangular structures at the edges of the silicon crystal. The thickness of around 100 nm is necessary to obtain a metallic characteristic of the contacts as well as the thermal stability especially at higher temperatures. After the sample had been removed from the contact preparation chamber, the metallicity of the contacts has been checked by a simple two point measurement 3.3. In all cases the resistance of the contacts were the same and varies only within 10%. The typical value for the contact resistivity is below 100  $\Omega cm$ . The picture of structured sample is shown in the fig.5.3.

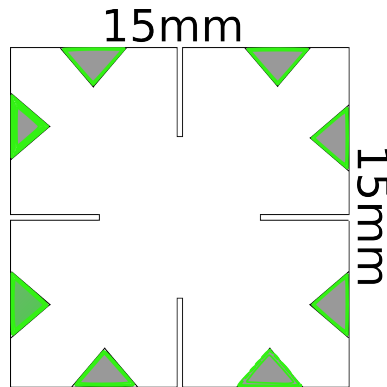


Abbildung 5.3: Si sample with eight  $TiSi_2$  contacts.

## 5.2 Electrical characterization of the contacts

The quality of the contacts is highly important for the transport measurements. Therefore, after the bake-out of the UHV chamber and degassing of the sample, the contacts have been checked with respect to their stability at different temperatures (room temperature (**RT**) down to 4K). The contacts have to be also

stable and chemically intact after the flashing-cleaning procedure. The conductivity of the clean Si(557) surface has therefore been measured both to check the quality of the contacts and also to measure the conductance contributions of the bulk at low temperatures in order to correct the data for the Pb/Si(557) system. The conductance of silicon samples depends strongly on temperature, the doping level and the kind of doping. Also the step structure of the surface has a influence on the conductance measured along and across the step edges. The silicon sample used within this work was always P - doped (Boron) silicon. The resistivity of the silicon at **RT** was 1500-3000  $\Omega cm$  depending on the wafer. The typical conductance as a function of temperature is presented in Fig. 5.4. The increase of the conductance at around 150K is due to an increase of charge carriers by ionization of the doping levels. [26]. On the other hand the mobility of charge carriers that are back-scattered on acoustic phonons is exponentially decreasing with the temperature. The combination of those two processes and taking into account the temperature dependent ionization energy of the impurities (in presence of Boron - it is an Acceptor level  $E_A$ ), gives the pronounced peak in the conductance curve as shown in Fig.5.4. The difference in height of the observed peaks at 180K is attributed to the electron back-scattering at the surface of the silicon substrate. The vicinal Si surface has a well defined roughness in the direction perpendicular to the steps. This fact suggests that the dopant segregation at the surface is also influenced by the surface steps. It is expected for the Boron atoms to cause higher conductance in the direction parallel to the steps.

The position of the peak is strongly depend on the number of charged impurities ( $N_A$ ). The increase of the level of doping results in a shift of the observed peak to lower temperatures and causes higher value of it. In the case of the sample that has been used for the experiments, the doping was very low which results in a higher peak temperature. A more detailed investigation of the intrinsic conductance of the SI crystal can be found in [26]. At temperatures below 120 K the resistance of the silicon sample has a very low value (less than  $1\mu S$  at temperatures below 80K) and has nearly no influence on the conductance measured for the Pb structures that are thicker than 3ML. In case of the conductance measured across the steps at the coverage of 1.3ML, the finite conductivity is mainly due to the bulk conductance. On the other hand, the conductivity measured along the step edges for the coverages in range of 0-1.3 ML has the contribution of both an electronic states of the silicon surface and the Pb atoms that are percolating or wetting (depends on the treatment of the sample). This can be observed as off-set value of the relative conductance measured during warming up.

An additional effect that has been observed on the vicinal samples is the anisotropy of the conductance between the two directions along and perpendicular direction to the silicon steps. The 8 points conductivity method described in the chapter 3.3 allowed to reduce the influence of the thermo-voltage across the sample which occurrence is normal for the large samples and it can induce 1-10 % distortions (depending on many factors like e.g. sample mounting) in the signal.

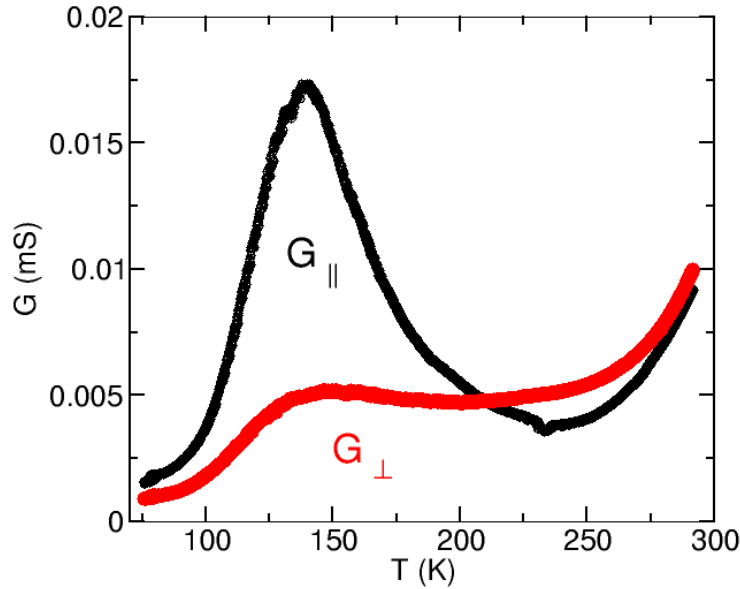


Abbildung 5.4: The conductance  $G$  of clean Si(557) measured along ( $L_{\parallel}$ ) and across ( $L_{\perp}$ ) the step direction as a function of temperature  $T$ , using 8 point configuration.

The lower conductance in the direction perpendicular to the step direction is simply explained by an enhanced backscattering of the charge carriers at modified potentials at the step edges sites as it is observed in the size effect experiments on the metallic films grown on the flat silicon surfaces. The peak position of higher mobility charge carriers at 150K is independent of the direction in which the conductance has been measured (parallel or perpendicular to the steps)[26].

### 5.3 Electrical characterization of Pb films on Si(557)

Thick Pb films deposited on the vicinal silicon samples have been electrically characterized by means of 2-, 4-, and 8-point conductivity measurements. The first conductance measurements during evaporation have been performed with 8-point contacts configuration and with the Pb-source set to low evaporation rate to avoid the conductance variation due to the light coming from the crucible. The films have been prepared at 2 different temperatures and with different coverages. Films of at least 10 ML have been used to calibrate the evaporator. Transport measurements of Pb films below 10 ML have been used to check again the quality of the contacts and homogeneity of the evaporation process.

The first monolayer does not reduce the anisotropy factor (which in case of Si

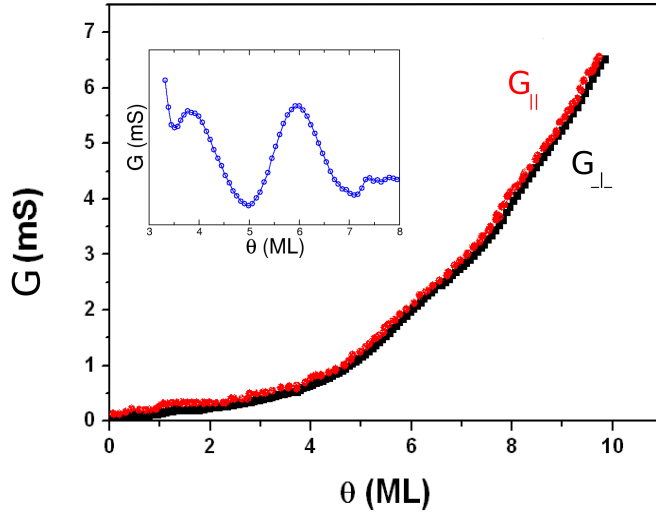


Abbildung 5.5: Conductance  $G$  measured during lead evaporation on Si(557) along and across the step directions. The small anisotropy between both direction is due to scaling hardly visible. Inset shows the oscillation of the conductance due to the size effect. The sample temperature during evaporation was kept at 78K and the flux has been set to 0.2 (ML/min).

surface is around 1.6 ) between the perpendicular and parallel direction to the step orientation. When the first layer is completed the second layer starts to grow and a higher slope of the conductance curve is observed as can be seen in the picture 5.5. The small oscillations visible in the inset of the fig.5.5 are the so-called classical size effect [46] and similar to what has been observed for Pb/Si(111)[26]. However, here obviously a smoothing of the surface at the vacuum interface occurs every second monolayer which is obviously a consequence of the vicinality. For Pb/Si(111) the conductance reaches a maximum after completion of every layer. The coverage range between 1 to 4 ML has been studied by means of conductivity measurement as a function of temperature and no 1-dimensional signature has been observed. In the case of Pb, using vicinal surface is not sufficient to generate 1-dimensional structures (i.e. structure that width and height are comparable small with the length of the structure like it has been observed for Pt/Ge(100) [3] and In/Si(111) systems [1]) because the energy that lead atoms have at temperatures around 70K is not enough. Evaporation at temperature range from 70K up to 300K did not increase the anisotropy of the Pb films. As it will be shown below, only the annealing to 640K generates a species which show a 1d transport behavior. In consistency with the isotropic transport regime presented above is the structure of the Pb films, which does not show any anisotropic features at all. As can be seen in the picture 5.6, a closed Pb film which consists of islands rotated with respect to each other by a small

angle as been generated. The rotation is due to the small lattice mismatch and the position at which the Pb atoms from the first monolayer occupy the unite cell of the silicon substrate. The detailed mechanism has been explained in the PhD thesis of A. Petkova [47].

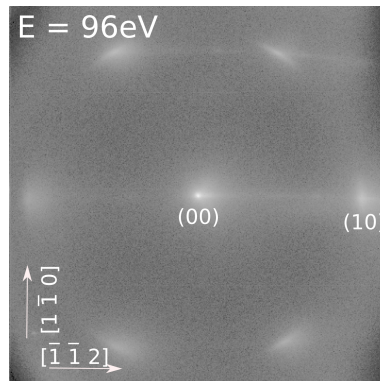


Abbildung 5.6: LEED pattern of a 6ML thin Pb film on Si(557). No signal from the underlying silicon substrate is visible pointing towards the growth of a closed Pb film. The elongated spots are due to the small rotation angle of Pb islands. The film was evaporated at 80K and post-annealed to 180K. The LEED pattern was taken at 80K.

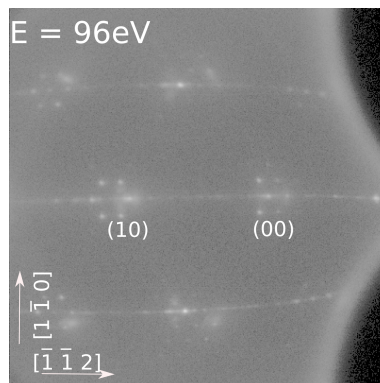


Abbildung 5.7: LEED pattern of 6ML of Pb/Si(557) heated up above 200K. The LEED pattern was taken at 80K.

Annealing the film to temperatures above 180K causes the whole film to break up. This results in lowering of the conductance down to the silicon bulk value. In the LEED pattern the spots of the  $7 \times 7$  reconstruction appear again as can be seen in Fig.5.7. The first and the sixth order spots are visible in parallel to the spots stemming from the Pb non-coalesced Pb islands (small bow-like reflexes 10 % BZ

away from the main order spots of silicon). Films that have been overheated were not used for further experiments. The broken adsorbate structure as described above and heated up to higher temperatures shows in LEED only  $\sqrt{3} \times \sqrt{3}$  an indication of a coverage below 1ML. The conductance shows only silicon-like transport as presented in Fig.5.4.





# Kapitel 6

## Pb-coverage phase diagram

This chapter contains systematic investigations of different Pb phases on Si(557). In particular, this investigation was important in order to calibrate the coverage accurately. The results have been published in the New Journal of Physics as: *Adsorbate induced refaceting: Pb chains on Si(557)*., **NJP 9 (2007) 338**. In this chapter only a short summary will be given. The original version of this publication is included thereafter. At the end, additional experimental results will be presented and discussed. All presented data were measured with SPA-LEED. Included STM data have been acquired in a different chamber but under comparable conditions. With those methods it was possible to investigate both the structure on a local-atomic scale and the periodic distribution.

Pb growth modes have been studied with respect to the average step separation which is related to the vicinal surface orientation, as well as the structure of growth films as a function of annealing temperature. First the most stable surface structure of 1.3 ML of Pb and its influence on the Si substrate have been discussed. In chapter 4.2 the structure of the clean vicinal silicon surface with (557) orientation is presented and the diffraction data are discussed in detail. As it was shown, the Si(557) surface consists of regularly distributed unit cells of 5.7 nm width, i.e a spot splitting of 5.9% SBZ in the  $[\bar{1}\bar{1}2]$  direction is observed in LEED. This picture changes drastically when the surface is covered by Pb and post-annealed to 640K. In the case of 1.3 ML Pb (which corresponds to the physical Pb monolayer on Si) the splitting in the  $[\bar{1}\bar{1}2]$ -direction at temperatures below 80K is 21.3% SBZ. As revealed further by LEED, the (7x7) reconstruction is completely destroyed. These two facts already give evidence that the Pb atoms destabilize the Si(557) surface and lead to refaceting of the initial surface. The direction of the facets has been determined by a so-called  $(k_{\perp}, k_{\parallel})$ -analysis. Interestingly upon Pb adsorption the Si(557) surface changes its crystallographic orientation to [223]-facets. That has been possible because the former electronic stabilization due to the (7x7) reconstruction is not present anymore. The energy gain is obtained by saturating the dangling bonds with Pb atoms. The second part of the article considers the lateral structure of Pb-layers on the mini-(111)

terraces. Within a very narrow coverage range, numerous phases have been observed, and, as it is presented in chapter 2.1, they can be explained as a combination of regularly redistributed unit cells of  $\sqrt{7} \times \sqrt{3}$  and  $\sqrt{3} \times \sqrt{3}$ . The combination of both units gives a so-called linear structure on the Si(111) terraces and the lateral periodicity is expressed by a periodic sequence of  $n \sqrt{7} \times \sqrt{3}$  units followed by  $m$  units of  $\sqrt{3} \times \sqrt{3}$ . The numbers  $m$  and  $n$  can easily be deduced from the domain wall splitting (see chapter 2.1) in LEED around the  $\sqrt{3}$  reflexes. As an example, the coverage of 1.3ML corresponds to the (1,5) phase ( $m=1$ ,  $n=5$ , the splitting is equal to 10%SBZ, in real space this has the periodicity of  $10 a_{Si}$ ). For the case where  $m > n$  the spot splitting at the  $\sqrt{3}$  position corresponds to the Pb concentration of less than 1.3 ML and can only be built on large Si(111) terraces because, as will be shown later, the small Si(111) terraces of Si(112) facets are too narrow. In case of  $m < n$  the concentration is either 1.3ML or greater and the splitting at the  $\sqrt{3}$  has only one domain in the  $[1\bar{1}0]$ -direction. Successive increase of the Pb concentration in steps of 0.002ML results in different splitting as shown in the publication. This fact was used for precise coverage calibration. At 1.314ML the splitting reaches the value of 8% (1,6-phase) and remains constant while the Pb coverage increases. In the last part of this publication, it is shown that the average step separation becomes unstable and different inclinations of the initial Si(557) surface are found. By adsorption and desorption of Pb atoms close to the melting point of Pb, it was possible to create one after another (112), (335), and finally (223) surface inclinations. Those changes were observed as spot splitting of main order spots in the  $[\bar{1}\bar{1}2]$  direction. An important observation is the reflexes along the half order streaks that indicated the dimerization at the step edge. After reaching the (1,5) phase the periodicity changes again to streaks. This supports the theory of an electronic stabilization by Pb atoms. More evidence is given in chapter 8, showing recent transport measurements. In particular for the (1,5) phase a pronounced phase transition has been found at 78K and will be discussed in the next chapter.

## Adsorbate induced refacetting: Pb chains on Si(557)

M Czubanowski, A Schuster, S Akbari, H Pfnür  
and C Tegenkamp<sup>1</sup>

Institut für Festkörperphysik, Leibniz-Universität Hannover, Appelstrasse 2,  
30167 Hannover, Germany

E-mail: [tegenkamp@fkp.uni-hannover.de](mailto:tegenkamp@fkp.uni-hannover.de)

*New Journal of Physics* **9** (2007) 338

Received 13 June 2007

Published 20 September 2007

Online at <http://www.njp.org/>

doi:10.1088/1367-2630/9/9/338

**Abstract.** The structure on the atomic and mesoscopic scale of Pb adsorbed on Si(557) has been investigated by high-resolution low energy electron diffraction (SPA-LEED). Depending on Pb coverage in the range between 1.2 and 1.6 monolayers (ML), formation of various facets [(112), (335), (223), and a meta-stable (557) orientation] is induced by the Pb layers. The facet orientation in general does not coincide with the macroscopic orientation of the (557) surface. After an initial annealing step to 600 K, starting with 1.2 ML of Pb, this new vicinality can be tuned gradually and reversibly even at temperatures below 180 K by further adsorption, but also by desorption of Pb. Superstructures of the Pb layers on the terraces were identified on the most stable (223) facets. Here parts of the devil's staircase and the stripe-incommensurate (SIC) phases known from Si(111) surfaces (Yakes *et al* 2004 *Phys. Rev. B* **69** 224103) develop. A new mechanism for facet formation with different orientations, based on avoidance of step decoration by adsorbed Pb, is proposed.

<sup>1</sup> Author to whom any correspondence should be addressed.

**Contents**

<b>1. Introduction</b>	<b>2</b>
<b>2. Experimental set-up</b>	<b>3</b>
<b>3. Results</b>	<b>4</b>
3.1. Clean Si(557) surface . . . . .	4
3.2. Facet stabilization by a Pb monolayer . . . . .	4
3.3. Devil's staircase phases . . . . .	8
3.4. Coverage-dependent step trains . . . . .	10
<b>4. Discussion</b>	<b>13</b>
<b>5. Summary</b>	<b>15</b>
<b>References</b>	<b>15</b>

**1. Introduction**

The growth of well-defined metallic overlayer structures on semiconductors has attracted much interest within the last few years. Low-doped semiconductor material is used in these cases, which acts as an effective insulator below room temperature. In the multilayer regime, these layers represent prototypes for the observation of quantum size effects (QSE), since they can be grown in some cases almost perfectly layer by layer with an atomically sharp interface [1]. Especially for metallic Pb layers, these quantum well states are responsible for the formation of 'magic' island heights [2]. Multiple changes of sign as a function of layer thickness in the Hall coefficient for Pb layers on Si(111) [3] turn out to be due to the thickness-dependent formation of the two-dimensional (2D) band structure, and are thus also related to the QSE.

Some of these systems can also be used to study (1D) structural and even electronic properties at concentrations below 1 monolayer (ML), which has recently opened a new field of study. However, instabilities are inherent in 1D systems and complicate the situation. The interplay between adsorbate and substrate interactions may allow to overcome part of these problems.

The 2D symmetry is either broken spontaneously as for In/Si(111) [4], e.g., and extremely anisotropic properties result from the combined lateral interactions between In and Si close to 1 ML. Alternatively, anisotropy is produced directly by use of a vicinal surface, and 1D metallic structures are generated far below monolayer concentration on each of the small terraces of the vicinal surface. An example is Au/Si(557), in which single Au chains on each small terrace are spontaneously formed at a concentration of only 0.2 ML. They exhibit the signature of almost 1D metallic bands in spectroscopy [5]. Using different vicinalities, e.g. (223), (335) and (557) the interaction between those metallic bands can be changed gradually [5, 6]. At these low concentrations only the local structure of the surface is rearranged, whereas the step-step distances do not or only weakly depend on coverage.

In this paper, we go to the other extreme, the situation of strongly coupled terraces in the coverage range around one physical monolayer and concentrate on structural aspects. With respect to the Si surface concentration of atoms, one physical monolayer corresponds to 1.33 ML on flat (111)-oriented Si surfaces. This assignment, neglecting the concentration adsorbed at step edges, will be used throughout this paper. As we show, the surface energy of the combined Pb/Si(557) system becomes strongly concentration dependent in the range between

1.2 and 1.4 ML, which leads to a Pb coverage-dependent refacetting of the whole surface to facet orientations that differ from the macroscopically given orientation.

This has important consequences also for the electronic properties of this surface. Recently, we have found that the formation of Pb chains on the Si(557) surface that is locally refaceted to a (223) orientation after adsorption of roughly one monolayer of Pb [7] (1.31 ML according to our calibration in this paper, see below) has quasi-1D properties of electrical conductance along these chains below a surface temperature of 80 K [8, 9]. Recent angle resolved photoemission spectroscopic (ARPES) measurements on these Pb monolayer chain structures demonstrate that at first glance the system electronically looks like an anisotropic, but 2D Fermi gas [10]. Conductance is obtained by Pb-modified surface bands that do not overlap with bulk Si bands so that pure surface conductance is observed [10]. Very close to the Fermi level, however, the periodicity of the Pb induced (223) facets normal to the steps plays a crucial role. It turns out that for this facet orientation the Fermi wavevector  $k_F$  in the direction normal to the steps corresponds exactly to half the reciprocal vector  $g = 2\pi/d$  ( $d$  is the average step separation). Thus  $k_F$  coincides with the Brillouin zone boundary in this direction, which results in gap opening and nesting of the Fermi surface. As a result, no conductance can be found in this direction for the perfectly ordered facets. This new mechanism for 1D conductance is a result of 2D coupling between the individual terraces and the Pb-induced stabilization of a certain step-step separation. Thus not only the typical instabilities inherent to 1D systems are avoided. This system also demonstrates the intriguing possibilities to tailor surface structure by adsorbate concentration together with electronic properties.

Therefore, in order to elucidate these possibilities in more detail, we investigate hereby an analysis with high resolution low energy electron diffraction (SPA-LEED), how the interchain distance can be tuned gradually by varying Pb concentrations up to 1.6 ML starting at 1.2 ML. This includes step decoration, which occurs only at concentrations above 1.33 ML. For the Pb concentrations between 1.2 and 1.33 ML, the main field of investigation here, our results and the structural models are partly at variance with recently published suggestions, based on a much less complete data set [11].

## 2. Experimental set-up

The experiments were performed in an UHV chamber equipped with SPA-LEED and Auger spectroscopy. The base pressure was  $1 \times 10^{-9}$  Pa and better than  $3 \times 10^{-8}$  Pa during evaporation. Pb was evaporated out of a ceramic crucible heated by a tungsten filament. A microbalance was used to control the amount of Pb. The monolayer ( $1 \text{ ML} = 7.84 \times 10^{14} \text{ atoms cm}^{-2}$ ) of Pb in this paper is given with respect to the Si(111) surface and the coverage was calibrated by LEED oscillations and thickness-dependent conductivity measurements. For the final calibration, we used the phase diagram for Pb/Si(111) measured in detail by Tringides and co-workers, see e.g. [12, 13]. In particular the DS-regime ('devil's staircase') was used to determine the coverage within 1% of a monolayer (for justification, see below). The Si(557) samples ( $1 \times 1 \text{ cm}^2$ ) were mounted on a manipulator, which was cooled by  $\ell\text{He}$ . Perfect Si(557) surfaces were prepared by degassing the sample for many hours until the pressure was below  $1 \times 10^{-8}$  Pa at  $600^\circ\text{C}$ . The removal of the oxide was done by heating the sample several times up to  $1100^\circ\text{C}$ . Higher flash temperatures rearrange the metastable (557) surface into large (111) domains separated by step bunches. The high-temperature steps were all performed by electron bombardment from the rear of the sample. For LEED and also for macroscopic transport measurements

a uniform phase distribution over the sample is of high importance, especially for Pb on Si substrates in the monolayer regime, as this paper demonstrates. Therefore, a uniform heating, i.e. temperature gradients of less than 5 K on the sample is necessary. This was achieved by a ring-shaped filament. The temperatures were measured pyrometrically and calibrated by Ni/NiCr thermocouples on dummy samples.

LEED measurements were typically done with a He-cooled sample close to 4 K, whereas adsorption and annealing was carried out at the temperatures indicated in the text.

### 3. Results

#### 3.1. Clean Si(557) surface

Figure 1(a) shows the diffraction pattern within the first SBZ (surface Brillouin zone) of a clean Si(557) surface at an in-phase condition for the (00)-beam ( $S = 5$ , the scattering phases are given with respect to double steps of Si(111)). Besides the integer spots as marked, the miscut towards the  $[\bar{1}\bar{1}2]$  direction reveals further signatures in the diffraction pattern: the integer spots are split along the mirror plane of the uniaxial surface (vertical direction). A  $(7 \times 7)$  reconstruction with strongly elongated spots in  $[\bar{1}\bar{1}2]$  direction characteristic for strongly anisotropic Si(111) terraces appears in between. In addition, streaks at 43% SBZ (corresponding to half the distance between the step train of integer order spots) along the  $[1\bar{1}0]$  direction are visible, indicating period doubling along the step edges. Whereas the split  $(1 \times 1)$  spots are fairly sharp, a signature of strong periodicity and correlation along the step train, little correlation between different terraces exists for the  $(7 \times 7)$  structure. As we show below by comparison with STM, this is a direct consequence of the equilibrium structure of the Si(557) surface.

This LEED image is a consequence of the fact that the (557) surface is not homogeneously stepped [14] with respect to steps of single atomic height. The equilibrium structure of Si(557) consists of triple steps [15]. A homogeneous step density implies a nominal terrace width of  $5\frac{2}{3}a_0$  (row distance  $a_0 = 3.32 \text{ \AA}$ ) with a spot splitting of 21.3% SBZ, contrary to our observation. Instead, the surface consists of minifacets with (111) and (112) orientations, as seen in the STM picture shown in figure 1(c) and schematically modeled in figure 1(b). The length of the unit cell is therefore  $17a_0$ , i.e. 16 diffraction spots appear in between the integer spots along the  $[\bar{1}\bar{1}2]$  direction.

Obviously for clean Si(557) the surface energy is minimized by the formation of  $(7 \times 7)$  reconstructions on one half of the unit cell. The Si atoms of atomic steps from vicinal Si(111) surfaces with inclinations towards the  $[\bar{1}\bar{1}2]$  direction have two unsaturated dangling bonds. These dimerize and explain the period doubling along the step edges. Recent high resolution STM experiments have shown that additional adatom structures on the mini (111) facets are present, stabilizing the triple step configuration of the Si(557) surface further [16].

#### 3.2. Facet stabilization by a Pb monolayer

In this subsection, we show that the situation changes completely when coverages close to a physical monolayer Pb (1.2 ML with respect to the Si(111) surface density) are adsorbed on

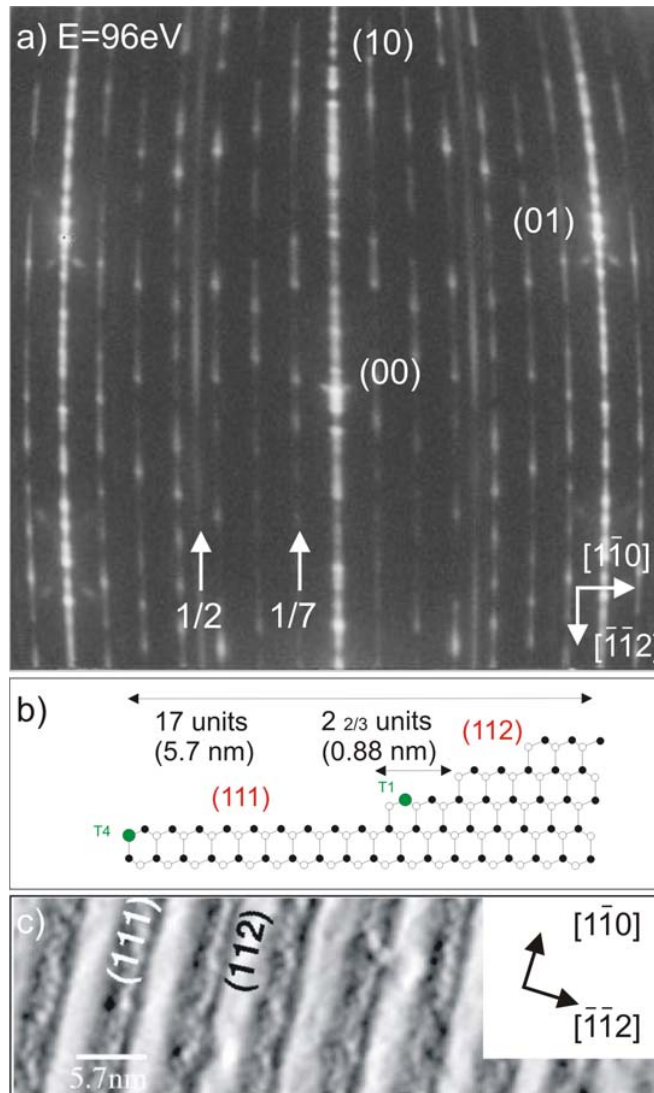


**Figure 1.** (a) Low energy electron diffraction (SPA-LEED) image of the clean Si(557) surface. (b) Sketch (side view) of the (557) unit cell. The clean Si(557) surface transforms into (111) and (112) facets. The alternating arrangements of these mini-facets are seen by STM shown in (c) ( $T = 40$  K).

Si(557). As will be demonstrated, new terrace widths are stabilized and can even be modified by Pb concentration. We start with the most stable structure at 1.3 ML, and then demonstrate in the next subsection changes of step densities induced by small changes of Pb concentrations.

The diffraction pattern obtained after the deposition of 1.3 ML at  $T = 80$  K followed by annealing to 600 K is shown in figure 2. Systematic annealing experiments have shown, that the  $(7 \times 7)$  reconstruction is destroyed by annealing at 570 K (as judged by LEED). However, small partial units of  $(7 \times 7)$  seem to remain, because an effective step mobility is only obtained for temperatures above 600 K [17]. Please note that once this destruction of  $(7 \times 7)$  units is



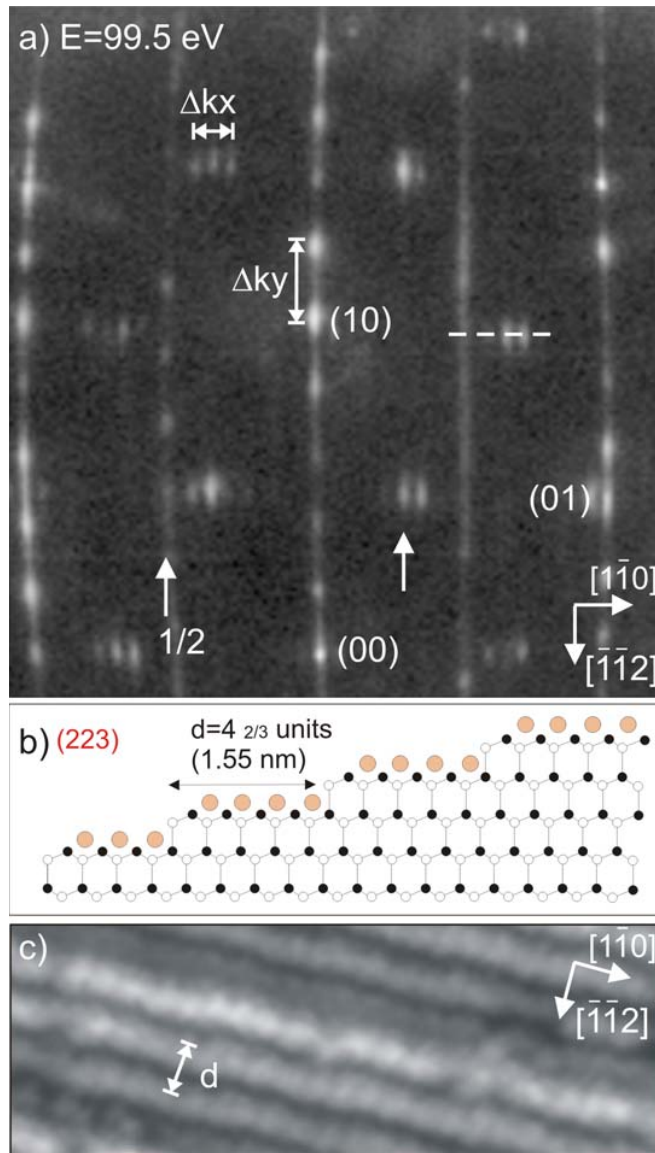


**Figure 2.** (a) LEED pattern after adsorption of 1.3 ML Pb and annealing to 600 K. The formation of an equally stepped surface with an average step–step distance of 1.55 nm results, as seen by the spot splitting of 21.3% SBZ, in agreement with STM (c) taken at  $T = 40$  K. A schematic side view is shown in (b). The small circles denote Si atoms, the larger grey (orange) ones Pb atoms within the first monolayer.

complete, step mobilities can be observed at temperatures as low as 80 K (see below). In this first step, even better order is obtained when multilayers of Pb are first adsorbed and subsequently desorbed at 640 K leaving the same residual coverage on the surface, as explicitly checked by Auger spectroscopy for both preparation methods.



The most obvious change compared with the clean surface is the spot splitting along the  $[\bar{1}\bar{1}2]$  direction. Only four spots appear in between (00) and (10) spots. The splitting of  $k_y = 21.3\%$  SBZ (compared with 5.9% on the clean surface) corresponds to a periodically stepped surface with an average step distance of  $4\frac{2}{3}a_0 (= 1.55 \text{ nm})$ . This phase has been found recently with STM, too (see figure 2(c) [8]). In addition, the  $(7 \times 7)$  reconstruction is not visible any longer in figure 2(a). Instead a new superstructure at the  $\sqrt{3}$  positions appears, which shows a spot splitting of 10% SBZ in the  $[1\bar{1}0]$  direction, i.e. along the terraces.

This result shows that a coverage of one physical monolayer of Pb is able to destabilize even the most stable (111) facet by modifying the surface energy. This is an activated process, since it occurs only by an annealing step close to the desorption temperature of Pb. The alternating (111) and (112) facets are now replaced by a homogeneously stepped surface. But, different from what is expected for repulsive step–step interactions, the resulting average terrace width does *not* correspond to that of the macroscopically cut (557) surface with an average terrace width of  $5\frac{2}{3}a_0$ . Instead, the initial step structure transforms into a (223) facet structure with an average terrace width of only  $4\frac{2}{3}a_0$  as depicted in figure 2(b). These results are in agreement with recent ARPES investigations carried out by us [10], which reveal a nested Fermi surface.

The validity of the model and the quality of the new Pb stabilized (223) facet is directly demonstrated by the  $(k_{\perp}, k_{\parallel})$ -plot shown in figure 3. For this graph, scans along the  $[\bar{1}\bar{1}2]$  direction were taken at electron energies between 80 and 230 eV in steps of 1 eV and their intensities were mapped onto a grey scale coded image. The circles denote the Bragg-points of the Si(111) surface. The rods measured over five 3D Bragg conditions demonstrate the macroscopic rearrangement of the (557) surface into a (223) facet structure. The mismatch between the macroscopically oriented (557) surface and the (223) facets is compensated most likely by small facets with opposite inclination angles, e.g. (331) facets. Indications of them are seen within the transfer widths of the SPA-LEED instrument only by faint intensity streaks at some Bragg-points (see arrow in figure 3). Furthermore, also wider (111) terraces may be formed locally to maintain the macroscopic orientation of the sample. A remarkable feature in figure 3 is the uniform width of the rods, which means a small variance in the terrace size distribution [18]. The largest full widths at half maximum (FWHM) of these rods between the Bragg points is around 5% SBZ.

The possibility that the steps of the initial (557) surface are simply overgrown by Pb, forming a homogeneously stepped metallic surface on top, can be safely excluded for several reasons. Firstly, a much higher coverage than one physical monolayer would be needed, which is far outside the uncertainty of our coverage calibration. Secondly, since the size distribution is very narrow, a change of the step density by additional Pb requires the addition of a sequence of 1, 2, 3...Pb chains on subsequent terraces in order to change the step density on a larger scale. This arrangement cannot be stabilized for simple entropic reasons. It further requires the local formation of a second Pb layer, which would be unstable to high temperature annealing. Thirdly, the  $(2 \times 1)$  reconstruction from the Si-step sites disappears by overgrowth at coverages above 1.4 ML (see below). Therefore the coverage must be smaller.

These results already demonstrate that the interface as a whole is transformed by a Pb monolayer into a regularly stepped surface with a step density different from the clean Si(557) surface. This is obviously the energetically favored configuration of this metal/semiconductor system.

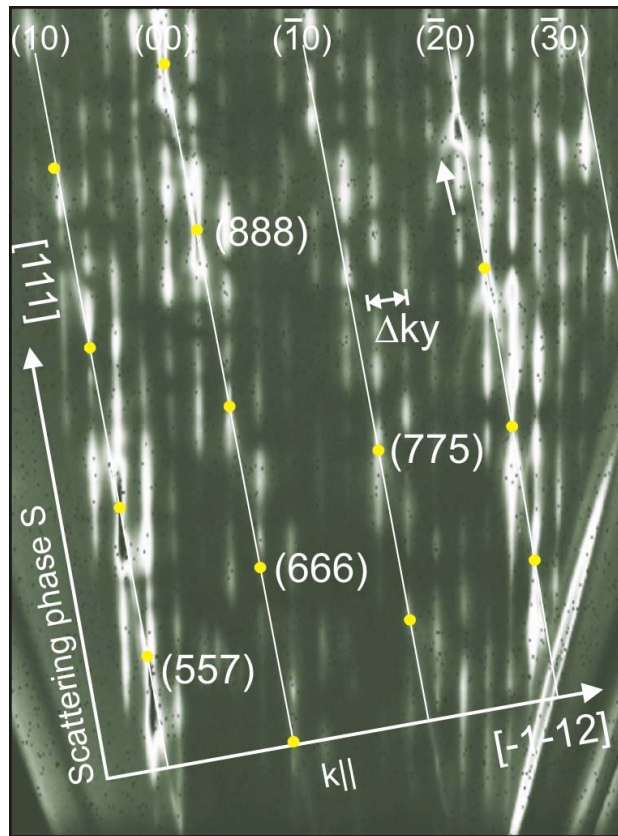


**Figure 3.**  $(k_{\perp}, k_{\parallel})$  plot of 1.3 ML Pb on Si(557). Scans along the  $[\bar{1}\bar{1}2]$  direction were taken for electron energies between 80 and 230 eV in steps of 1 eV. Their intensities are shown as a grey scale coded image (white means high intensity). The grey (yellow) circles mark the Bragg-points of the Si(111) surface for better orientation. The graph shows nicely the rods of the (223) facets.

### 3.3. Devil's staircase phases

Before we investigate changes of the surface morphology by varying Pb concentrations in the range between 1.2 and 1.3 ML, we will focus in the following on the lateral arrangement of Pb at coverages above 1.30 ML. As will be shown, they resemble closely the devil's staircase phases found on Pb/Si(111) [12]. In this range of coverage, the (223) orientation of facets remains unchanged.

The spot splitting of the superstructures seen in figure 2 can be explained by formation of so-called linear  $(m,n)$ -phases, a combination of  $m\sqrt{7} \times \sqrt{3}$  and  $n\sqrt{3} \times \sqrt{3}$  units, which appear in our case only as a single domain structure along the terraces. The combination of all possible  $(m,n)$  values forms a devil's staircase. A structural model of a (1,5) phase, which was most easily formed in our case, is shown in figure 4. According to the model outlined for the monolayer regime of Pb/Si(111) [12], the unit cell of the  $\sqrt{3} \times \sqrt{3}$  phase consists of four Pb atoms (one on the centered H3 and three on off-centered T1 places), i.e. the coverage is  $\frac{4}{3}$  ML, whereas the

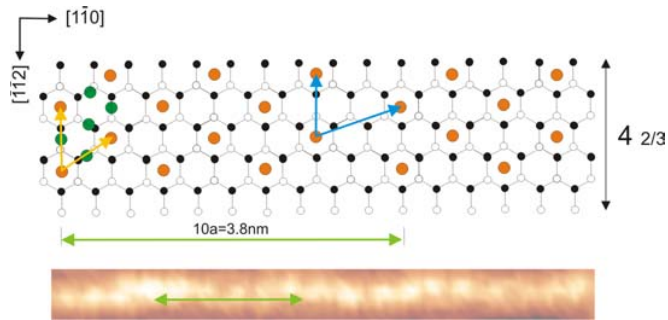


**Figure 4.** Model of the (1,5) phase of 1.31 ML Pb on Si(557). The closed and open small circles denote Si atoms of the first and second substrate layer, respectively. The light grey (orange) filled circles represent Pb atoms on H3 positions. The dark grey filled (green) circles are Pb atoms on off-centered T1 positions, exemplarily shown only for first  $\sqrt{3} \times \sqrt{3}$  unit cell. This linear phase can be seen as a 10-fold periodicity within a single Pb-chain by STM [7].

( $\sqrt{7} \times \sqrt{3}$ ) cell contains six Pb atoms (one on H3, five on off-centered T1) per five Si atoms. The coverage of a (1,5) phase is therefore 1.31 ML.

In diffraction experiments these linear phases are seen as spots appearing with different splitting around  $\sqrt{3}$ -sites. The splitting of  $k_x \approx 10\%$  SBZ corresponds to a 10-fold periodicity along the Pb-chain direction and is in good agreement with our STM results, which have revealed a modulation along the Pb chain. A magnification of such a modulated Pb chain is shown at the bottom of figure 4 [7]. It should be noted that the terraces of the (223) facets have sufficient width to form ordered  $\sqrt{3}$ -units on these terraces. This is different for other facet orientations, as we will show below.

Proof that the (1,5) phase mentioned above is indeed part of a devil's staircase is shown in figure 5, where line scans through the (00) spot along the  $[1\bar{1}0]$  direction, i.e. parallel to the step edges around the  $\sqrt{3}$ -positions are shown. Varying the coverage by subsequent addition of small amounts of Pb between 1.30 and 1.314 ML at a surface temperature of 80 K (LEED measurements at 4 K), the splitting of the  $\sqrt{3}$  spots changes from 14.2 to 8.1% SBZ. This corresponds to a change from a (1,3) to a (1,6) phase. Ordering of these phases requires some diffusion of Pb even at 80 K. Such low activation barriers are typical and have been reported also for the Pb/Si(111) system within the devil's staircase coverage regime [12]. The accompanied ultra-fast kinetics of these phases have been discussed recently in terms of a collective diffusion coefficient with singularities at distinct coverages, i.e. at the devil's staircase phases [19]. In fact, the phases ranging from (1,3) to (1,6) have been used to calibrate the Pb coverage most precisely.

For a Pb coverage of 1.42 ML the splitting is around 8% SBZ and remains constant up to 1.62 ML. This phase is comparable to a stripe-incommensurate (SIC) phase, seen for Pb/Si(111) at coverages higher than 1.34 ML [19]. The periodicity of this SIC phase is ( $12 \times \sqrt{3}$ ), slightly smaller than the ( $13 \times \sqrt{3}$ ) and ( $14 \times \sqrt{3}$ ) structures suggested in [20, 21] for Pb on Si(111). This small difference may be due to an influence of the steps on ultra-short (111) terraces. It should also be mentioned that in contrast to the Pb/Si(111) system, the linear phases and the SIC-structures can be distinguished only by the spot splitting of the superstructures along the  $[1\bar{1}0]$  direction.

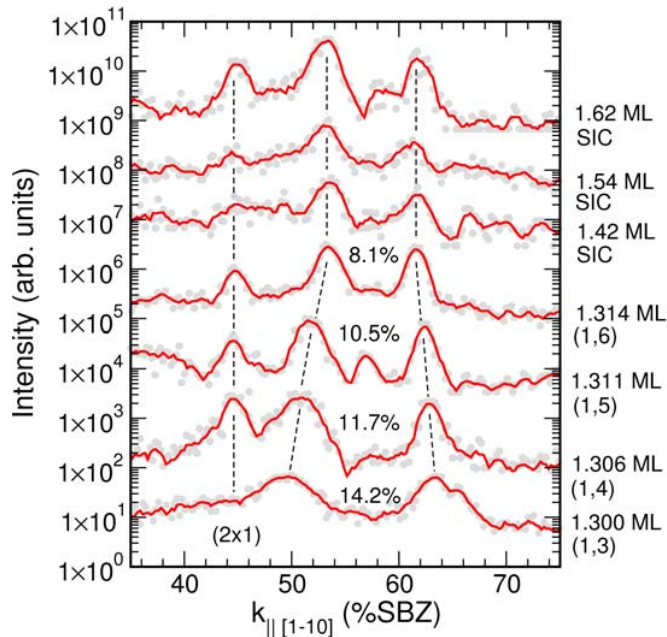


**Figure 5.** Line scans taken along the  $[1\bar{1}0]$  direction at  $E = 99.5$  eV ( $S = 5.1$ ). Shown is the region around the  $\sqrt{3}$  positions (cf with dashed line in figure 2(a)). The gradually shrinking spot splitting with increasing coverage is the signature for different linear phases  $(m,n)$ . For coverages between 1.4 and 1.6 ML the SIC phase is found with a constant spot splitting of 8% SBZ (solid curve = 5-pt averaging).

In the LEED pattern of figure 2 at a Pb coverage of 1.30 ML the streaks at half order positions of the clean (557) surface have developed into clear spots with a separation again of 21.3% SBZ, i.e. the separation of the steps at this Pb concentration. This not only shows that the dimerization at the step edges still survives after Pb adsorption of 1.30 ML, there must also be a strong correlation between the step edges. Otherwise the spot would again appear as streaks along the  $[\bar{1}\bar{1}2]$  direction.

This  $(2 \times 1)$  reconstruction along the step edges shows a characteristic coverage dependence. It disappears for coverages between 1.4 and 1.5 ML, which indicates a step decoration by excess Pb atoms. For higher coverages, the  $(2 \times 1)$  intensity appears again, i.e. after completion of the decoration process. Obviously, Pb first covers the terraces, then fills the step sites at coverages around 1.4 ML, but leaves the dimerization of the Si step structure unchanged once all step sites are filled by Pb.

### 3.4. Coverage-dependent step trains

In this subsection, we show that, unlike the situation for the physical monolayer coverage and above ( $\Theta > 1.33$ ), where the (223) facet structure is conserved, the average step separation becomes unstable at smaller Pb concentrations between 1.2 and 1.3 ML. As a consequence, other inclinations of the initial (557) surface are found.

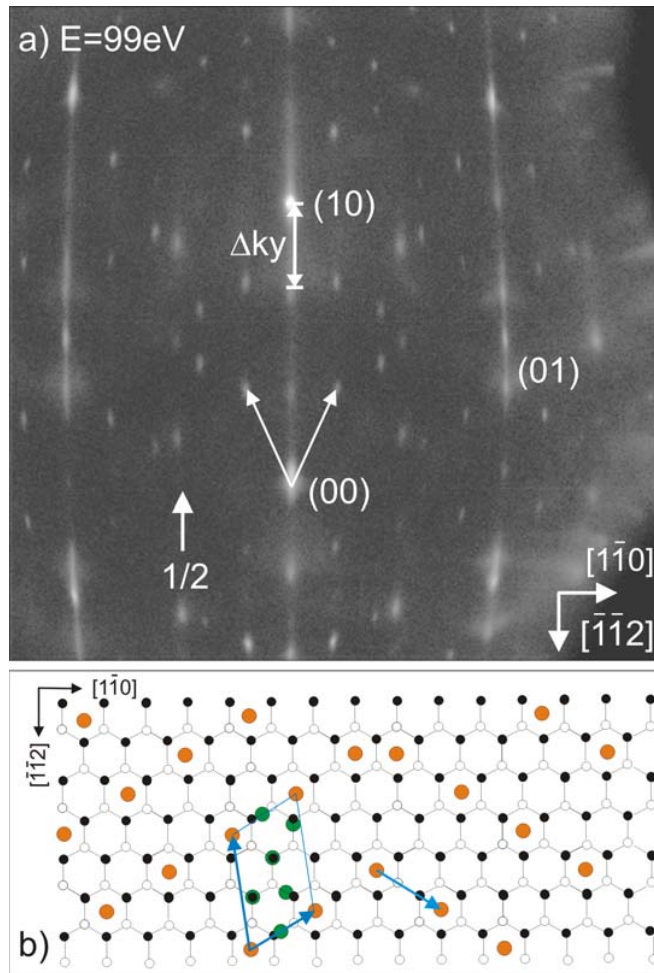


**Figure 6.** (a) LEED pattern obtained for 1.22 ML Pb/Si(557) ( $T = 40$  K). (b) Shows the mirror domain ( $\sqrt{7} \times \sqrt{3}$ ) structure on (111) terraces. Larger grey (orange) circles denote Pb atoms on the H3 positions. The dark grey (green) larger circles are Pb atoms adsorbed at off-centered T1 sites. The only superstructures from the (112) facets are the half order spots.

The pattern shown in figure 6 was obtained by partial desorption of Pb at a surface temperature of 640 K, starting from, e.g., 1.3 ML coverage. The remaining Pb coverage is 1.20 ML as judged from the two domains of pure  $\sqrt{7} \times \sqrt{3}$  LEED structure seen in this figure. Since the spots are not elongated, this structure must be formed on portions of the surface with large (111) terraces. The same structure can also be obtained by adding Pb to a lower coverage after the high temperature annealing step has taken place.

In addition, the step structure, visible from the spot splitting of integer order spots, has significantly changed compared with the 1.3 ML phase, although the difference in Pb coverage is only 0.1 ML. The separation of  $k_y = 37.3\%$  SBZ belongs to a step train of (112) facets, with (111) terraces that are only  $2\frac{2}{3}a_0$  wide. These facets are too small to allow formation of a



$(\sqrt{7} \times \sqrt{3})$  superstructure. It can only form on larger (111) terraces, which compensate for the high inclination of the (112) facets. As depicted in figure 6(b), a  $(\sqrt{7} \times \sqrt{3})$  mirror domain structure can be formed on these larger terraces, in perfect agreement with the LEED pattern. All atoms of Pb in this phase are shown exemplarily only in one of the unit cells. Due to the vicinality of the surface, the third domain is missing, i.e. only faint intensity features are seen sometimes.

According to the LEED and STM investigations for Pb/Si(111) [12], the coverage of this  $(\sqrt{7} \times \sqrt{3})$  structure is 1.20 ML. Again, and similar to the (1,5) linear phase of figure 2(a), the half order spots for this Pb coverage have the same spot splitting as the integer spots. This supports the assumption from above that this reconstruction stems indeed from the step sites of the surface.

Together with changes in the lateral structures on the (111) terraces as a function of Pb concentration, the step train structure can be further tuned from (112), (335) to (223) facets and finally even to steps trains, which correspond to equally stepped (557) substrates, by increasing the Pb concentration gradually between 1.20 and 1.35 ML. The homogeneously stepped (557) orientation with 18% SBZ spot splitting is the least stable of these phases and is visible only for adsorption temperatures below 80 K and a coverage around  $1.34 \pm 0.02$  ML. At higher temperatures it transforms back to the (223) facets described above.

This sequence (apart from the homogeneously stepped (557) surface) was found in evaporation experiments at a surface temperature of 180 K, in which small concentrations of Pb were added. After evaporation, the samples were always cooled to 4 K for the LEED observations. Figure 7 shows a sequence of line scans taken across the step direction for coverages ranging from 1.2 ML to 1.62 ML. The addition of 0.04 ML to the 1.2 ML shown in figure 5 results in a (4,1) linear phase structure (again on larger (111) terraces). The spot splitting in the direction normal to the steps is  $k_y = 27.3\%$  SBZ, characteristic of a (335) facet orientation. The high mismatch between these phases and the original (557) inclination is manifested by the high FWHM value, which is larger than 10% SBZ. Finally, further adsorption of 0.06 ML leads to the formation of the already known (223) facet orientation. The 21.3% SBZ splitting is clearly visible and remains visible for coverages up to 1.62 ML.

We emphasize here that the morphological changes resulting from the variation of the step density in presence of a monolayer of Pb are already possible at deposition temperatures as low as 180 K (and in the case of (557) even around 80 K!). This shows that monolayer adsorption of Pb has strongly weakened the Si bonds particularly at step edges so that Pb–Si complexes can diffuse effectively and rearrange the step structure already at these low temperatures. There is still an activation barrier, however, since better ordering is obtained after annealing to 600 K, slightly below the desorption threshold.

From the profile in figure 7 taken at 1.42 ML coverage, it seems that the step train can also be modified at Pb coverages higher than one physical monolayer. The addition of 0.1 ML of Pb at 180 K to the linear phases with a coverage around 1.32 ML, e.g. (1,5), results in period doubling along the  $[\bar{1}\bar{1}2]$  direction, whereas the splitting along the [110] remains at 8% SBZ (cf with figure 6). Adding once more 0.1 ML of Pb results in complete removal of this periodicity doubling, and the well known 21.3% SBZ splitting of the (223) reappears.

Therefore, morphological changes of the step train are unlikely in this case. In fact, this finding is fully compatible with the assumption already made above that up to a coverage of 1.32 ML the step edges are not covered by Pb. The addition of approximately 0.1 ML of Pb suffices to decorate every second step. It corresponds well with the average step density of

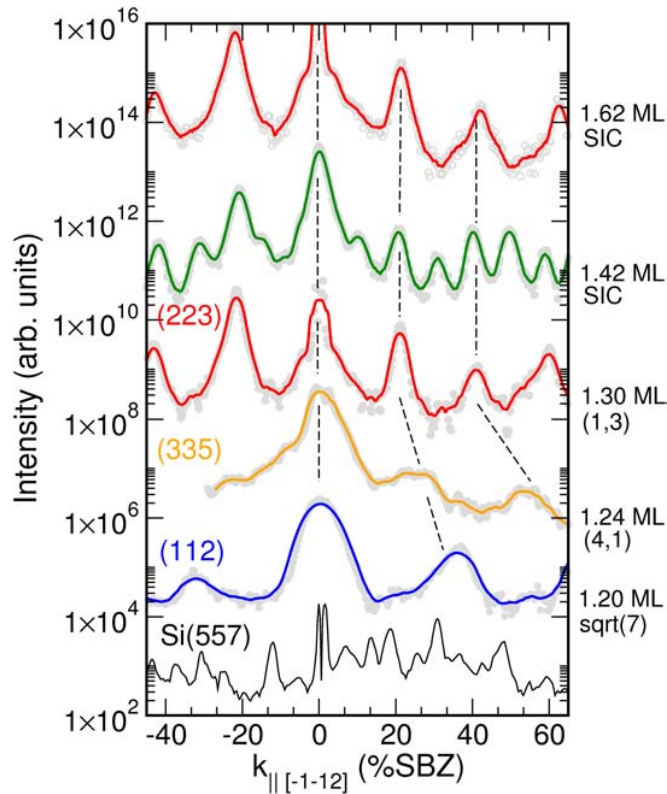


**Figure 7.** (a) Line scans along the  $[\bar{1}\bar{1}2]$  direction for coverages between 1.20 and 1.62 ML. The deposition was carried out at 180 K, whereas the measurement was done at 4 K at an electron energy of 99.5 eV.

$2 \times 4\frac{2}{3}$  unit cells. The second addition of the same amount of Pb fills all step edges, and the original periodicity reappears.

#### 4. Discussion

Our results show that Pb coverages in the monolayer regime between 1.2 and 1.3 ML are able to destabilize the macroscopically cut vicinal Si(557) surface and to readjust the step density depending on Pb coverage. This happens already at temperatures below 180 K, and for a small range of concentration even at 80 K once the Si(7 × 7) order is removed. Fairly high diffusion coefficients are necessary even at these low temperatures, which at first glance seems to be surprising. However, as shown recently by Yakes *et al* [22] for the monolayer regime of Pb/Si(111), at which the devil's staircase phases appear, temperatures as low as 40 K suffice to make Pb mobile, with typical singularities in the (calculated) diffusion coefficients at the completion of ordered phases. While these results are not directly transferable to our system, where the diffusion of both Pb and Si atoms is necessary, they show that low activation energies for diffusion are involved in the Pb/Si system, especially at critical concentrations that lead to structural changes.

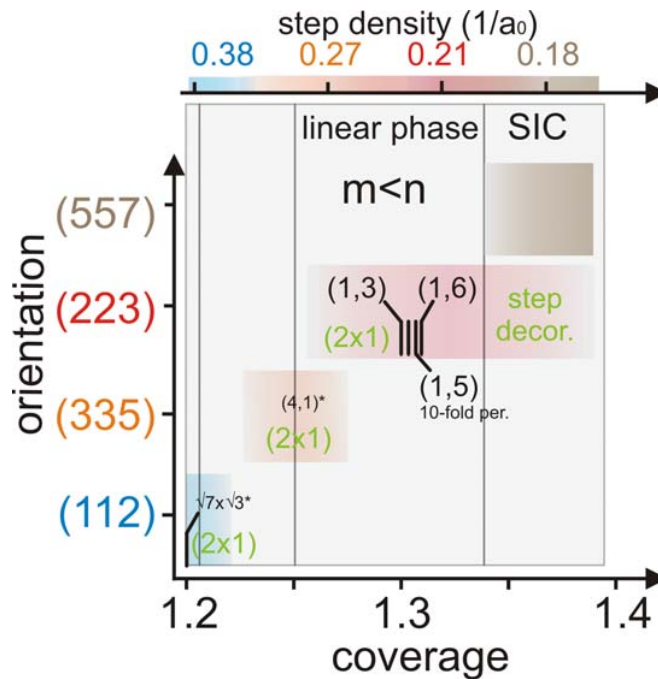


**Figure 8.** Phase diagram for Pb/Si(557). The (\*) marked phases appear only on larger (111) terraces. For further details see text.

The steps in this system play a particularly important role, since their density changes dramatically with Pb concentration. Contrary to what might be expected, the steps themselves cannot act as nucleation sites on these stepped surfaces, since the periodic step train structure, irrespective of the orientation of the facets, always maintains the  $(2 \times 1)$  reconstruction that already exists for the clean (557) surface. That the Si dimers of the clean surface are not replaced by, e.g. Pb-dimers is consistent with STM results for Pb/Si(100) [23]. These results show that the Pb–Si bond on the dimerized surface is so weak that it is not able to lift Si–Si dimerization. Therefore, it seems reasonable to assume that Pb covers predominantly only the small (111) terraces without occupying the step edges.

We can go even one step further: local monolayer formation ( $\Theta = 1.33$  ML) on small terraces seems to be the most stable configuration on these stepped surfaces, even at the expense of creating additional step edges. This seems to be the case for a coverage of 1.2 ML, at which (112) facets are formed with an extremely high step density. Following this argument as a function of increasing Pb concentration, additional Pb should be adsorbed on (111) terrace sites, not on step edges. This can only be managed by increasing the terrace widths, thereby reducing the step density.

Indeed, this model works almost quantitatively, as figure 8 shows. Here, we plotted the ranges of stability of the various facets as a function of Pb concentration (bottom axis) and simultaneously as a function of decreasing step density. The decreasing step density corresponds well to the increment of Pb concentration starting at 1.2 ML and corroborates our model. Thus, the driving force for the facetting is the Pb adsorption energy that depends strongly on local configuration and coordination. It is interesting to note that the (223) facet in presence of Pb



turns out to be the most stable configuration that finally survives. Only at higher concentrations, where second Pb layer formation starts, can steps also be decorated on these most stable (223) facets.

The electronic consequences have so far been only explored for the (223) facet orientation. As known for other systems, e.g. Ag and Au adsorbed on Si(111) [24, 25], the stability of surface phases depends strongly on the filling factors of the surface band structure, i.e. on the coverage of the adatoms. For these (223)-facets, with a terrace width of  $4\frac{2}{3}a_0$  we found indeed [10], that the Fermi wavevector  $k_F$  is half a reciprocal lattice vector  $g = 2\pi/d$  with  $d = 4\frac{2}{3}a_0$ , which results in Fermi nesting and in gap opening. Thus, there may also be an electronic contribution to the stabilization of this structure, whereas any step–step interaction does not play an important role.

## 5. Summary

We have shown in this SPA-LEED analysis that adsorption of Pb in the monolayer regime on vicinal Si(111) leads to the formation of several uniformly faceted surfaces. Generally, the equilibrium structure of vicinal surfaces is determined by both the terraces and the steps. With adsorbed Pb, the differences in surface energies between terraces and steps are strongly enhanced in the monolayer regime.

Depending on the exact coverage, different Pb-phases as well as different step–step distances, i.e. (112), (335), (223) and (557) orientations, have been found. Furthermore, the lateral Pb–phase *and* the vicinality can be tuned gradually and reversibly by changing the Pb coverage. Whereas for  $T = 80$  K only terrace diffusion is effective, the Ehrlich–Schwoebel barrier between the terraces is overcome for substrate temperatures already below 180 K.

Parts of devil’s staircase phases can only develop on the larger (223) terraces close to 1.3 ML.

Because of the strong sensitivity of the Pb adsorption energy to local coordination, the main mechanism for stabilization of the facets by monolayers of Pb seems to be the avoidance of step occupation. Therefore the step density is adjusted so that all Pb atoms can be adsorbed on (111) oriented terrace sites.

## References

- [1] Dil J H, Kampen T U, Hülsen B, Seyller T and Horn K 2007 *Phys. Rev. B* **75** 161401
- [2] Yeh V, Berbil-Bautista L, Wang C Z, Ho K M and Tringides M C 2000 *Phys. Rev. Lett.* **85** 5158
- [3] Vilfan I and Pfnür H 2003 *Eur. Phys. J. B* **36** 2817
- [4] Yeom H W *et al* 1999 *Phys. Rev. Lett.* **82** 4898
- [5] Crain J N, Kirakosian A, Altmann K N, Bromberger C, Erwin S C, McChesney J L, Lin J-L and Himpsel F J 2003 *Phys. Rev. Lett.* **90** 176805
- [6] Crain J N and Himpsel F J 2006 *Appl. Phys. A* **82** 431
- [7] Tegenkamp C and Pfnür H 2007 *Surf. Sci.* **601** 2641
- [8] Tegenkamp C, Kallassy Z, Guenter H-L, Zielasek V and Pfnür H 2005 *Eur. Phys. J. B* **43** 557
- [9] Tegenkamp C, Kallassy Z, Pfnür H, Günter H-L, Zielasek V and Henzler M 2005 *Phys. Rev. Lett.* **95** 176804
- [10] Tegenkamp C, Ohta T, McChesney J L, Pfnür H and Horn K submitted
- [11] Kim K S, Choi H and Yeom H W 2007 *Phys. Rev. B* **75** 195324
- [12] Yakes M, Yeh V, Hupalo M and Tringides M C 2004 *Phys. Rev. B* **69** 224103

- [13] Stepanovsky S, Yakes M, Yeh V, Hupalo M and Tringides M C 2006 *Surf. Sci.* **600** 1417
- [14] Kirakosian A, Bennewitz R, Crain J N, Fauster Th, Lin J-L, Petrovykh D Y and Himpsel F J 2001 *Appl. Phys. Lett.* **79** 1608
- [15] Phaneuf R J and Williams E D 1990 *Phys. Rev. B* **41** 2991
- [16] Tey S A, Romanyuk K N, Zhachuk R A and Olshanetsky B Z 2006 *Surf. Sci.* **600** 4878
- [17] Schuster A, Czubanowski M, Pfnür H and Tegenkamp C to be published
- [18] Tong X and Bennett P A 1991 *Phys. Rev. Lett.* **67** 101  
Tegenkamp C *et al* 2002 *Phys. Rev. B* **65** 235316
- [19] Yakes M, Hupalo M, Zaluska-Kotur M A, Gortel Z W and Tringides M C 2007 *Phys. Rev. Lett.* **98** 135504
- [20] Choi W H, Koh H, Rotenberg E and Yeom H W 2007 *Phys. Rev. B* **75** 075329
- [21] Hoque E, Petkova A and Henzler M 2002 *Surf. Sci.* **515** 312
- [22] Yakes M, Hupalo M, Zaluska-Kotur M A, Gortel Z W and Tringides M C 2007 *Phys. Rev. Lett.* **98** 135504
- [23] Dong Z-C, Fujita D and Nejoh H 2001 *Phys. Rev. B* **63** 115402
- [24] Crain J N, Altmann K N, Bromberger C and Himpsel F J 2002 *Phys. Rev. B* **66** 205302
- [25] Crain J N, Gallagher M C, McChesney J L, Bissen M and Himpsel F J 2005 *Phys. Rev. B* **72** 045312

## 6.1 Supplement

In addition to the experimental evidences presented in the publication, a more detailed characterization of the phase diagram has been performed in the meanwhile for the coverage range between 1.3 and 1.4ML. It has been found that additional Pb coverage of 0.04ML in excess of 1.3 ML, decorate the step edges what can be seen by the appearance of an extra periodicity in the  $[\bar{1}\bar{1}2]$  direction in LEED. The new periodicity is commensurate with the average step-step separation for the Pb/Si - (223) surface with the periodicity equal to the even number of  $\mathbf{g} = 4\frac{2}{3}$ . The situation that appeared at coverages above 1.3ML suggests that Pb atoms that are bounded at the step edge (the low energy adsorption site) create chains of atoms with the separation given by the periodicity observed in the LEED. The picture 6.1 presents line scans taken along  $[\bar{1}\bar{1}2]$  direction above transition temperature  $T_c$  for different coverages, where the mentioned periodicity has been observed. As it will be shown later in chapter 8, this new periodicity suppresses gradually the perfect nesting condition that has been observed for the 1.3 phase in conductance as well as in LEED by introducing periodically higher electron density with  $k = n \times 2k_f$ .

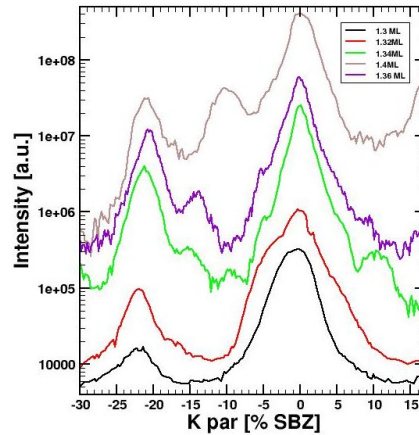


Abbildung 6.1: Line scans taken along the  $[\bar{1}\bar{1}2]$  direction for different coverages above the transition temperature.

The periodic decoration of the step edges has devil's staircase nature as observed for the chain structure of (1,5) phase. The fact that despite Ehrlich-Schwobel barriers, a long ordered phase can evolve points towards a strong electron-electron correlation across the step direction. For instance, the coverage of 1.32ML every 8<sup>th</sup> step is decorated i.e. the separation of the wires is  $8 \times 4\frac{2}{3}$  of Si lattice constant. Secondly, the periodicity induced new band gap at position of the  $n \times 2k_f$  - vector. The influence on the electronic configuration and thermal stability of the

decorated steps will be discussed in more detail together with the conductivity and/or spectroscopy data in the last chapter.

# Kapitel 7

## Temperature driven phase transition

Evaporation of Pb onto Si(557) at low temperatures followed by annealing to 640K results in the formation of one-dimensional structures, as has been shown in chapter 6. At least 1.2 ML of Pb is needed to generate linear phases of  $\sqrt{7} \times \sqrt{3}$  units on Si(111) mini-terraces. According to the coverage estimation presented before, all phases have been studied for structural changes as a function of temperature. It has been found that the 1.3ML Pb phase on Si(557), which forms a linear (1,5) phase and undergoes the 1d/2d phase transition in conductance, shows also reversible changes in structure as a function of the temperature. The observed phase transition in conductance at 78K has been already reported in ref. [5]. In the following chapter the publication concerning the structure of the (1,5)-phase and its structural phase transition will be presented and discussed in more detail. The thermally driven phase transition on the 1.3ML of Pb/Si(557) is due to structural changes at 78K along the  $[\bar{1}\bar{1}2]$  direction. For this direction, at low temperatures the Fermi nesting conditions are fulfilled as reported in [6]. The article has been published in Physical Review B in 2008 under the title: *Temperature-driven refacetting phase transition in Pb chains on Si(557)*. The experimental description will be extended below. A copy of this publication is attached hereafter.

The structure of the (1,5)-phase is the subject of this chapter. It is characterized by a chain structure, as reported by STM and confirmed with LEED analysis. The chains have a specific width of 1.55nm at temperatures below  $T_c = 78\text{K}$  and are oriented in the  $[1\bar{1}0]$  direction i.e. along the step edges. The whole surface is homogeneously covered by this wire-like structure, as revealed by SPA-LEED studies. In the following, the temperature driven changes within this structure, that has been found in the LEED pattern, are discussed. By changing the temperature of the sample, the splitting of step train reflexes (that is 21.3 % SBZ at lower temperatures - LHe) changes to 20.5 % SBZ. The transition has a first order character, occurs at exactly 78K and is reversible. The temperature at which the

transition occurs is correlated with the transition observed in conductivity. In the second part of this paper, the splitting of the reflexes will be discussed in more details. The splitting in the  $[\bar{1}\bar{1}2]$  direction is equal to inverse of the wire separation. The change from 21.3 to 20.5 % SBZ indicates deviation from the initial (223) orientation. From the energy dependency of the step train reflexes measured for both structures, the orientation of the new facet direction was estimated to be close to  $[17\ 17\ 25]$ . From the spot analysis, it turns out that after rising the temperature above  $T_c$ , the step train not only shifts relative to the (10) diffraction spot, but additionally splits into smaller (around 3 % SBZ) periodicity as the new structure appears. The new periodicity does not fulfill the nesting conditions and transport across the wires is possible. At the temperatures as low as 80 K the Pb atoms have enough energy to deffuse from the step edges and in this sense electronically destabilize the system. The structure along the wires is also influenced by the thermally activated Pb atoms. The changes in the domain wall periodicity has been also observed. This investigation has given clear evidence for electronic and structural coupling in the Pb/Si(557) system.

# Temperature-driven refacetting phase transition in Pb chains on Si(557)

M. Czubanowski, A. Schuster, H. Pfnür, and C. Tegenkamp

*Institut für Festkörperphysik, Leibniz-Universität Hannover, 30167 Hannover, Germany*

(Received 11 February 2008; revised manuscript received 1 April 2008; published 13 May 2008)

By using quantitative low energy electron diffraction, we have studied the temperature-driven phase transition of Pb chains grown on Si(557) substrates at a surface concentration of 1.3 ML. This concentration, which is still below one physical monolayer, exhibits a unique switching of electrical conductance from one dimensional to two dimensional above 78 K, which is coupled to this phase transition, and was investigated for this reason. Annealing to 640 K causes a concentration-driven refacetting of the whole surface into large (223) facets at low temperatures, while along the chains a so-called (1,5) linear phase is formed, causing a tenfold periodicity. At  $T_c=78$  K, we analyze a *temperature-driven* order-order transition along the  $[\bar{1}\bar{1}2]$  direction in detail, which again turns out to be a refacetting transition. The two-dimensional character of this transition was seen by corresponding structural changes along the  $[1\bar{1}0]$  direction as well. Refacetting causes a change in periodicity and destroys the conditions of Fermi nesting necessary for one-dimensional conductance.

DOI: [10.1103/PhysRevB.77.174108](https://doi.org/10.1103/PhysRevB.77.174108)

PACS number(s): 73.20.At, 73.21.-b, 68.65.-k, 73.25.+i

## I. INTRODUCTION

Confinement effects give rise to fundamental changes in the electronic structure and transport properties in low-dimensional systems. Enhanced correlations between electrons and phonons result in the formation of new quasiparticles, e.g., holons and spinons.<sup>1,2</sup>

As physical model systems in two dimensions, many examples from surface science have been reported in recent years that use, in particular, semiconductor surfaces as templates for the growth of metallic overlayers. In general, this approach allows the control of the morphology, the electronic structure, and the manipulation by, e.g., coadsorption experiments. Characteristic interactions between the adsorbates and the surface reveal the development of metallic surface states. Low dopant concentrations and formation of Schottky barriers at the surface spatially and electronically separate the surface from any bulk and space charge layer contributions. The growth of atomic wires as typical one-dimensional (1D) systems has been found for a variety of materials, such as, e.g., In, Au, Ag, Pt as mono- or submonolayers on Si, and Ge surfaces with different orientations and vicinalities.<sup>3-7</sup> They were generated by self-assembling processes. The 1D character for these systems has been proven by scanning tunneling microscopy (STM) in combination with spectroscopy, revealing a dispersion only along the atomic wires. By using vicinal substrates, even the interchain interaction is tunable and 1D to two-dimensional (2D) transitions can be studied.

Inherent to such low-dimensional systems, however, are instabilities, which lead to metal-insulator transitions for the electronic properties, as, e.g., in Pt/Ge(100).<sup>7,8</sup> These are coupled with structural changes, such as, e.g., period doubling in the simplest case.<sup>9</sup> There are, however, more complicated situations, and the structural nature of transition in low-dimensional systems has been clarified only for very few examples. E.g., for In/Si(111), the  $(4 \times 1) \rightarrow (8 \times 2)$  transition is close to a displacive phase transition,<sup>10,11</sup> whereas the  $(2 \times 1) \rightarrow c(4 \times 2)$  transitions of the reconstructed Si(100) and Ge(100) surfaces have an order-disorder character.<sup>12</sup> The

$\sqrt{3} \times \sqrt{3} \rightarrow (3 \times 3)$  transition found for the Sn/Ge(111) system is, however, still under debate.<sup>13</sup>

The Pb system on vicinal Si(557) is not just another example of such transitions, but it turned out to give insight into the properties between one and two dimensions. The adsorption of Pb on this surface leads to a coverage dependent change in step densities that is close to one physical monolayer, coupled with the formation of small Pb covered miniterraces that can be considered as atomic wires.<sup>14</sup> The annealed coverage of 1.3 ML Pb is particularly interesting because electrical conductance in this system reversibly switches from a 2D transport regime into a 1D regime below  $T_c=78$  K, where only along the wire conductance can be measured, while in the perpendicular direction a metal-insulator transition is seen.<sup>15,16</sup> This Pb concentration stabilizes the (223) facet orientation, which corresponds to formation of atomic wires that are four atoms wide with a mesoscopic interchain distance of 1.55 nm.<sup>14,15,17,18</sup> Furthermore, the wires themselves are modulated due to Pb reconstructions on mini-(111) terraces (for details, see Sec. III A). A clear signature for a phase transition has been found not only by transport measurements but also by angle resolved photoemission spectroscopy (ARPES) experiments. Interestingly, ARPES has shown that these wires, contrary to, e.g., Au/Si(557), are two dimensionally coupled and the 1D transport regime is caused by perfect nesting of the Fermi surface at temperatures below  $T_c=78$  K rather than by confinement effects.<sup>19</sup> Due to this strong coupling, it is obvious that any structural change will have drastic consequences toward the electronic properties, but the temperature-driven structural transition has not been identified yet. This is the purpose of this paper.

Former measurements seemed to suggest an order-disorder type of transition, as judged from STM measurements at temperatures well below and above  $T_c$ . However, as we will demonstrate below, small changes in average lattice constants and extremely large periodicities are involved, for which spot profile analysis (SPA)-low energy electron diffraction (LEED) turns out to be a much more powerful method than local methods, since long-range correlations can



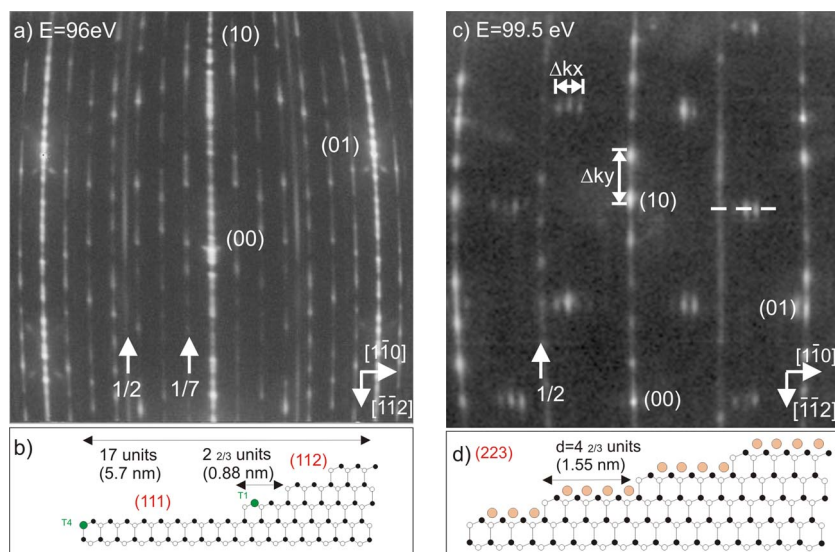


FIG. 1. (Color online) LEED picture of the clean Si(557) surface (a) and after adsorption and thermal annealing of 1.3 ML Pb (c). At the bottom, schematics of the clean (b) and the surface covered by 1.3 ML of Pb are shown (d). The measurements were performed at 40 K.

be still monitored despite strong fluctuations at the atomic scale, expected for these systems above  $T_c$ .

In this paper, we present SPA-LEED results that indeed show a clear phase transition at exactly  $T_c=78$  K. Induced by thermal activation, the average terrace length is increased; therefore, we call it a refacetting phase transition. The impact of this structural phase transition will be discussed in context with the phase transition seen in conductivity.

## II. EXPERIMENTAL SETUP

The sample preparation has been carried out in an UHV chamber operating at a base pressure of  $1 \times 10^{-9}$  Pa. After careful outgassing of the low-doped Si(557) sample, final heating cycles up to 1100 °C have been performed by electron beam heating from the rear of the sample until the Si(557) surface showed a clear LEED pattern of the alternating arrangement of (111) and (112) facets with  $7 \times 7$  and  $2 \times 1$  reconstructions, respectively, with the characteristic 17-fold splitting of the spots normal to the step direction. Pb was adsorbed out of a ceramic crucible and the coverage was detected by a quartz microbalance. The exact Pb coverage has been calibrated by using the spot splitting of the domain wall phase formed by the  $\sqrt{3} \times \sqrt{3}$  order on the terraces with  $\sqrt{7} \times \sqrt{3}$  domain walls, which is also known from Pb/Si(111).<sup>14,20</sup> In a first step, the Pb layers were annealed to 640 K in order to remove the original  $7 \times 7$  Si structure of the clean terraces and to allow the reordering of the step structure. Further details for the Pb/Si(557) system can be found in Ref. 14.

The sample was mounted on a shielded cryostat so that it could be cooled down to about 4 K by  $\ell$ He. The low temperature regime of up to 300 K was measured by a diode within the cryostat bath, whereas higher temperatures were measured pyrometrically direct on the sample. Both temperature regimes were calibrated in advance by using Ni/NiCr thermocouples on dummy samples. In addition, a power calibration versus steady-state temperatures was carried out.

## III. RESULTS

### A. Pb-induced chain formation

In order to make the LEED results on the temperature-driven phase transition understandable, which is presented in Sec. III B in detail, we briefly review the essentials obtained around a Pb coverage of 1.30 ML, which is of main importance here. It corresponds to slightly less than one physical monolayer on the terraces.

The clean Si(557) is an unequally stepped surface, which locally consists of (111) and (112) facets, yielding an overall unit cell of 17 a.u. along the  $[\bar{1}\bar{1}2]$  direction (5.7 nm) [compare to Fig. 1(b)]. Owing to the (111) miniterrace, LEED reveals uniaxially elongated seventh-order spots, while the half-order spots stem from dimerization at the step edges of the (112) facets. The large unit cell is best seen by the spot splitting of 5.8% surface Brillouin zone (SBZ) of the integer spots in the  $[\bar{1}\bar{1}2]$  direction. A LEED pattern taken at 96 eV (scattering phase  $S=5$  and step height  $d=3.14$  Å) is shown in Fig. 1(a). Details about further reconstructions at step edges and terrace sites were recently obtained by STM measurements.<sup>21</sup>

The adsorption of 1.3 ML Pb on Si(557) followed by annealing to 640 K leads to fundamental changes in the surface structure. As evident from the LEED pattern shown in Fig. 1(c), the most striking feature is the spot splitting with a distance between the spots of  $\Delta k_y=21.3\%$  SBZ in the  $[\bar{1}\bar{1}2]$  direction at temperatures below 78 K. The analysis of the spot profiles has revealed that this splitting corresponds to a (223) facet orientation rather than to a (557) orientation. As schematically depicted in Fig. 1(d), the steps are homogeneously distributed and the terraces are now  $4\frac{2}{3}$  a.u., i.e., 1.55 nm wide. The mismatch between both orientations is compensated by terraces with the opposite inclination angle, which do not form larger facets and are, therefore, not visible in LEED. This result of refacetting on a mesoscopic scale is fully supported by recent STM measurements.<sup>17</sup> This phase has been identified as the one responsible for one-dimensional conductance. We will characterize its



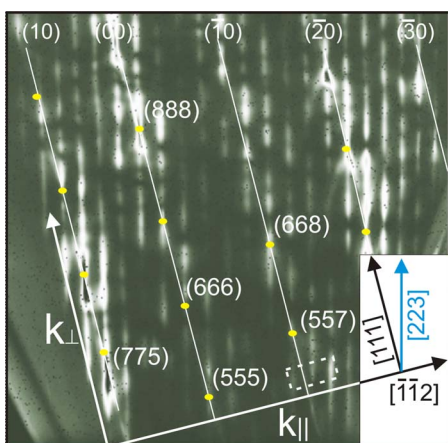


FIG. 2. (Color online)  $(k_{\perp}, k_{\parallel})$  plot along the  $[\bar{1}\bar{1}\bar{2}]$  direction showing the regular step train of a (223) facet after adsorption of 1.3 ML Pb on Si(557) and annealing to 640 K. This figure was generated by taking line scans along the central vertical spots of Fig. 1(c) at constant electron energies between 80 and 230 eV. The measurements are taken at  $T=40$  K. The dashed square marks the scattering condition, where the step structure has been analyzed as a function of temperature (compare to Fig. 3).

temperature-driven phase transition in Sec. III B.

As is also obvious from Fig. 1(c), superstructure spots at  $\sqrt{3} \times \sqrt{3}$  positions appear, which are split by  $k_x \approx 10\%$  SBZ in the  $[1\bar{1}\bar{0}]$  direction. We have recently shown that this periodicity is caused by regularly arranged domain walls. On each terrace, this so-called (1,5) linear phase consists of  $5\sqrt{3} \times \sqrt{3}$ , separated by a  $\sqrt{7} \times \sqrt{3}$  domain wall. In agreement with previous STM measurements, the chains on adjacent terraces are correlated because the full width at half maximum (FWHM) of these spots periodically varies as a function of the scattering phase.<sup>22</sup>

By varying the Pb concentration on the surface, the interchain distance and the modulation periodicity can be gradually tuned as a function of coverage between 1.2 and 1.6 ML. A detailed phase diagram of the Pb/Si(557) system can be found in Ref. 14. Interestingly, the (557) orientation itself is metastable in the presence of Pb. Among these different Pb phases on Si(557), only the (223) facet structure reveals a nearly equally distributed step structure and only this turns out to be energetically favored, as shown by latest ARPES results.<sup>19</sup> The perfectness of the Pb-induced vicinality is demonstrated in Fig. 2, showing a  $(k_{\perp}, k_{\parallel})$  plot, i.e., line scans along the  $[\bar{1}\bar{1}\bar{2}]$  direction were taken at different electron energies and plotted as a grayscale coded image.

Not surprisingly, this particular step structure that strongly deviates from the clean (111) surface is stabilized by the Pb layer. This means that, although STM sees a wirelike structure,<sup>17</sup> these wires must be strongly coupled in two dimensions, which is in agreement with results from a Fermi surface mapping of Pb/Si(557) in the monolayer regime.<sup>19,23</sup> The one-dimensional conductance found for this layer at low temperature below 78 K is thus caused by this particular array of periodic wires resulting in perfect Fermi nesting rather than by localization due to confinement in single wires. The abrupt switching in conductance to a weakly an-

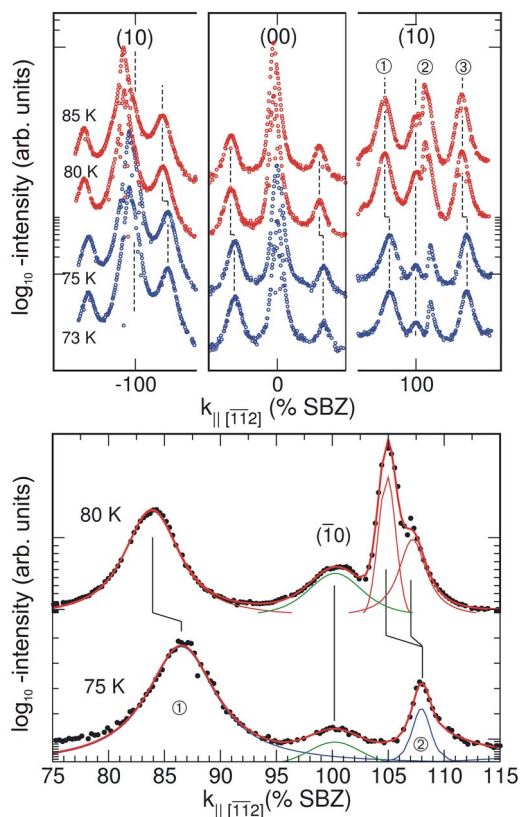


FIG. 3. (Color online) Line scans around the (10), (00), and  $(\bar{1}\bar{0})$  spots and adjacent diffraction peaks of the step structure along the  $[\bar{1}\bar{1}\bar{2}]$  direction at constant energy ( $S=5.1$ ) but different temperatures around the transition temperature  $T_c=78$  K. A magnification of the peak profile of the  $(\bar{1}\bar{0})$  spot close to the phase transition is shown in the bottom part.

isotropic two-dimensional system at higher temperature is due to a breakdown of these perfect nesting conditions due to structural changes upon annealing, as we show in Sec. IV. Here, we analyze changes in spot profiles as a function of temperature in detail.

## B. Temperature dependent changes in the diffraction pattern

As mentioned, we concentrate on the coverage of 1.30 ML of Pb, i.e., on the (1,5) phase. The upper part of Fig. 3 shows profiles taken at 96 eV around the (10), (00), and  $(\bar{1}\bar{0})$  spots, respectively, at various temperatures below and above the phase transition observed in conductance. The satellite peaks around these spots are due to the step train of the (223) facet structure. Starting at low surface temperature, changes become obvious in diffraction, when crossing the transition temperature around 78 K. As can be seen there, peaks shift as a whole, which is most obvious at the  $(\bar{1}\bar{0})$  spot, and partly change shape, while the separation between peaks, in general, is slightly reduced. This indicates that either the facet orientation of the surface changes again upon thermal excitation, or that a phase equilibrium between different facet orientations is established above the phase transition.

In order to understand the nature of this phase transition in more detail, we first test the hypothesis that the average inclination of the surface can also be changed by temperature. For that purpose, we investigated the spot profiles in those parts of  $k$  space in more detail where the changes are most prominent.

This is the case for the  $(\bar{1}0)$  spot, for which a magnification of the line scans close to  $T_c$  is shown in the lower part of Fig. 3. Below  $T_c$ , the part of the profiles shown there can be well described by three diffraction peaks (blue curves, denoted by 1 and 2). The electron energy of 96 eV is almost an out-of-phase scattering condition for the first-order spot with respect to a step height of 3.14 Å between (111) terraces (green curve), as can be seen by the almost symmetric relative positions of the step train peaks with respect to the  $(\bar{1}0)$  peak. This small  $(\bar{1}0)$  peak would not be present for a homogeneously stepped surface but exists due to small inhomogeneities on the surface or pinned steps yielding larger and uncorrelated (111) terraces. A comparison of intensities at many different electron energies shows that these larger (111) terraces cover less than 10% of the surface area. For the present purpose, however, their  $(\bar{1}0)$  diffraction peak, which is fixed in  $k$  space, serves as a calibration point in reciprocal space.

The varying FWHMs of peaks 1 and 3 compared to peak 2 directly reflect the finite variance of the terrace length distribution.<sup>24</sup> Assuming a Poisson distribution for the terrace length around a mean value, the FWHM of the diffraction peaks depends on the variance, but also on the distance,  $\Delta k$ , to the next Bragg point as  $\text{FWHM} \propto (\Delta k)^2$ . The detailed analysis of the broadening of the FWHM with respect to the scattering phase relative to the next in-phase condition allows us to calculate the variance. Following the analysis described in Ref. 24, the average variance is  $\sigma \approx 0.2a$ , assuming a FWHM of 5% SBZ of the broad peaks at a scattering phase difference of around  $\pi$  with respect to the (557) Bragg point.

Above  $T_c$ , the diffraction peaks of the step train shift relative to the  $(\bar{1}0)$  diffraction peak, but are also split or broadened. Examples for these two cases are again seen at the bottom of Fig. 3. Peak 2 shifts closer to the Bragg peak so that splitting into two peaks can be observed. The splitting is around 3% SBZ. On the other hand, a splitting of peak 1 cannot be resolved due to broadening. These shifts, splitting, and broadenings are reversible and no further changes in shape or position were found while changing the substrate temperature between 4 and 100 K. All changes in positions, temperature dependent splittings, and associated changes of half-widths are compatible with a transition from the (223) facets to an average (17 17 25) orientation, as will be demonstrated below.

A schematic of the Ewald construction for the (223) and (17 17 25) facet structures is shown in Fig. 4(a). The parts that correspond to the scattering conditions of the line scans presented in Fig. 3 are enlarged in Fig. 4(b) for below  $T_c$  and in Fig. 4(c) for above  $T_c$ . As shown in this schematic, the shift and spot splitting of peak 2 in Fig. 3 above the phase transition is caused by the transition to a high index surface with an inclination in between the (557) and the (223) orien-

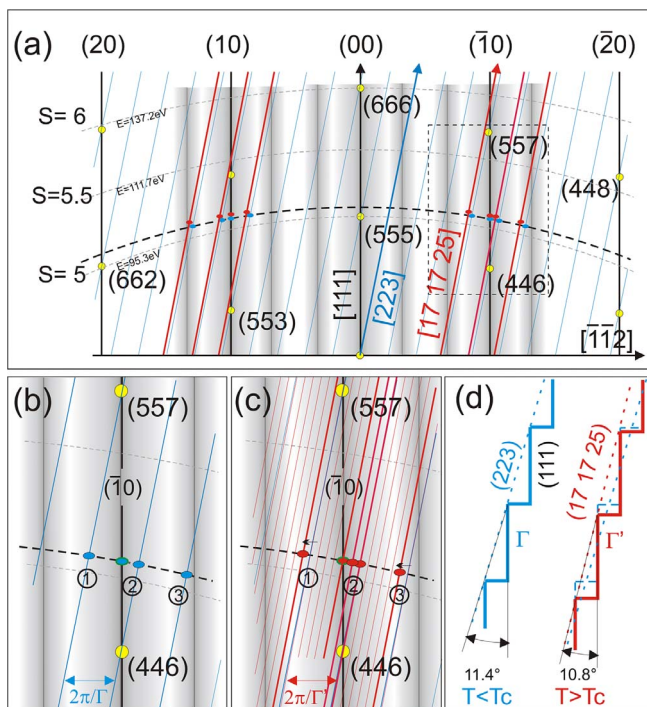


FIG. 4. (Color online) (a) Ewald construction of the diffraction rods as seen by experiments shown in Fig. 2. The blue lines represent the (223) facet structure below  $T_c$ , while the facet rods of the high index commensurate (17 17 25) orientation are marked in red. (b) and (c) show magnifications of the area in (a) marked by dashed lines below and above  $T_c$  for the (223) and (17 17 25) facet structures, respectively. The numbers correspond to the numbers in Fig. 3. The intensity modulation of the step train spots by the form factor of a single terrace is indicated by the shaded intensity oscillations implying that only the thick red lines in (c) can be observed at the scattering conditions of Fig. 3. (d) Schematic drawing of the two step configurations illustrating the increase in the average terrace lengths above  $T_c$ .

tation of the clean and the Pb covered surface at low temperatures, respectively. A (17 17 25) facet structure yields a splitting between two (17 17 25) rods of  $\frac{1}{6} \frac{1}{\Gamma_{223}} = 3.5\% \text{SBZ}$ , very close to our finding.

As can be seen from Figs. 4(b) and 4(c), the rods nicely explain the shifts of the step diffraction peaks and even the splitting of the step peak denoted by 2 and changes of half-widths at others. Because of the chosen scattering condition, this diffraction peak shifts to a condition close to in-phase scattering, i.e., the influence of the variance in the terrace size distribution is small enough so that the peaks can be resolved. In contrast, step diffraction spots of higher order appear only broadened (1 and 3) and a substructure cannot be resolved. Furthermore, the modulation of the intensity distribution by the form factor of the (111) miniterraces suppresses further diffraction peaks of the high index facet structure.

Although the general behavior of the changes in the diffraction pattern can be explained by this change of average facet orientation, a direct measurement of the change of inclination angle can only be obtained by energy dependent measurements. Therefore, we have measured the spot split-

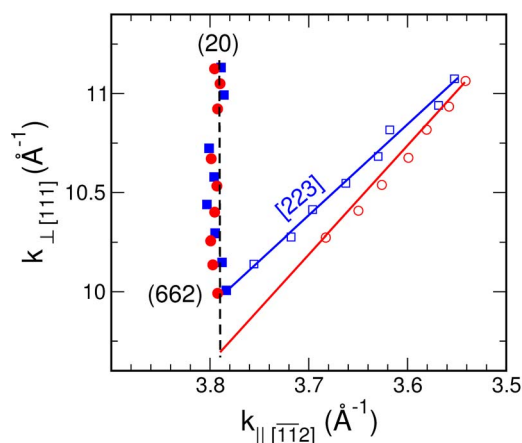


FIG. 5. (Color online) Peak positions of (223) step spot (open symbols) with respect to the (111) rod (closed symbols) measured at 4 (squares) and 80 K (circles) at the (662) Bragg point.

ting as a function of energy for two different temperatures. Exemplarily, the energy dependent splitting of the (20) rod around the (662) Bragg point and the adjacent step train peak are plotted in Fig. 5 for below and above  $T_c$ . The scattering conditions are given in  $\text{\AA}^{-1}$  to directly allow the determination of the facet orientation via  $\tan(\theta) = \frac{k_{\parallel}}{k_{\perp}}$ . The electron energy was varied between 96 and 127 eV, which correspond to phases  $S=5$  and  $S=5.75$ , respectively. For the measurement at 4 K, the angle between the rods is  $\theta = 11.4^\circ \pm 0.3^\circ$ , which is in almost perfect agreement with a (223) facet as already judged from the spot splitting  $\Delta k_y$ . At 80 K, this angle changes to  $10.5^\circ \pm 0.3^\circ$ , which is within error bars compatible with a (17 17 25) orientation. This directly proves the temperature dependent reorientation of the whole surface and excludes demixing of different facet orientations on the surface.

To further prove our model and to determine the exact phase temperature, we have analyzed the spot separation as a function of substrate temperature for step-induced diffraction spots for which splitting is not resolvable [see Fig. 6(a)]. This is the case for the majority of spots. However, if the (223) facet orientation is replaced by a high index orientation, the nonresolved peak must contain more than one diffraction spot so that their FWHM must increase. This is exactly what we see. An example is shown in Fig. 6(b). These plots directly demonstrate that both the changes in peak separation and in half-width are directly related to the phase transition at 78 K. Both results qualitatively agree for the FWHM and for the peak splitting even quantitatively with our suggested model: The spot splitting  $\Delta k_y = 2\pi/\Gamma$  of 21.3% SBZ, i.e., of the (223) step train structure, remains constant up to a temperature of 75 K, while above 78 K it changes to 20.5% SBZ, i.e., close to five unit cells per terrace on average. The clean Si(557) surface has a nominal terrace width of  $5\frac{2}{3}$  unit cells, which corresponds to 17.6% SBZ spot splitting and therefore can be well discriminated. This small decrease in the spot splitting is fully consistent with the model schematically sketched in Fig. 4(d).

Since diffraction reveals only the average of a quantity, the obviously incommensurate value for the spot splitting

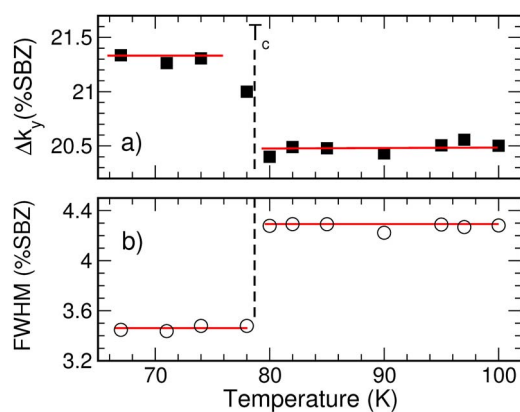


FIG. 6. (Color online) (a) Variation in spot separation as a function of temperature for step-induced diffraction peaks taken at 96 eV (splitting not resolvable here). (b) FWHM of a step diffraction peak around the  $\bar{2}0$  spot vs temperature. In both cases, the discontinuity at  $T_c$  is clearly visible.

above  $T_c$  is the effect of measuring the Fourier transform of a terrace size distribution on a discrete lattice. On average, one row of atoms is added to six (223) terraces, and this correlation must be maintained over several of these large units in order to identify separated diffraction peaks. Both static disorder and thermal fluctuations reduce this order. Consequently, not all diffraction rods of the high index commensurate phase can be detected but only those close to Bragg points, as demonstrated by the spot splitting seen in Fig. 3. For other scattering conditions, this structural transition is seen only by a change in the FWHM due to the finite variance in the terrace size distribution. Exactly at  $T_c$ , the FWHM changes to a higher value and remains constant up to 100 K. Fluctuations around the phase transition temperature should cause higher FWHM values only at  $T_c$ . The abrupt change seen in Fig. 6 points toward a first-order phase transition, as one might intuitively expect also from the transport measurements, although the conductance itself is not directly related to the order parameter.

The observed changes at the structural phase transition at 78 K are not limited to the average terrace width. We also observed small changes in the domain wall separation of the original Pb-induced (1,5) phase along the terraces, which demonstrate that couplings between terraces and the associated phase transitions cannot be treated as one dimensional, in agreement with latest ARPES measurements.<sup>19</sup> Figure 7(a) shows the spot splitting of the domain wall spots *along the*  $[1\bar{1}0]$  *direction* as a function of temperature revealing a 4% increase of the average domain wall separation at  $T_c$ . In Fig. 7(b), we have plotted the peak position of the simultaneously measured  $\sqrt{3}$  spot. The fact that the position does not shift with temperature excludes any instrumental effects upon annealing the sample.

#### IV. DISCUSSION

Our results that we have just presented show that for the physical monolayer of Pb [1.30 ML Pb with respect to the Si(111) surface concentration], a prominent phase transition



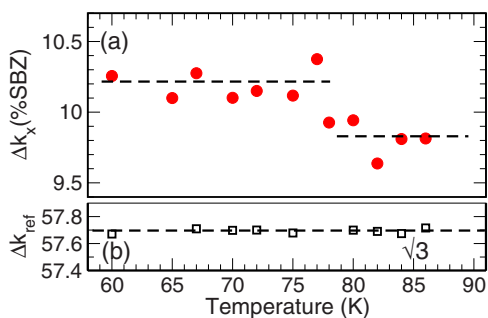


FIG. 7. (Color online) (a) The domain wall splitting  $\Delta k_x$  along the  $[\bar{1}\bar{1}0]$  direction as a function of temperature. (b) Peak position of the  $\sqrt{3}$  position vs temperature.

occurs at  $T_c = 78$  K, where both the distances of adjacent steps and of domain walls in the direction along the steps abruptly increase by about 4% on average. It is worth pointing out, however, that no local expansions of lattice constant are involved in this phase transition and all atoms remain on their crystalline sites. It is thus a type of order-order phase transition, in which only the average inclination of the facets on the surface changes at  $T_c$ . We call this a refacetting surface phase transition. From the small background intensity and the absence of clear fluctuation-induced contributions to the diffraction profiles, we conclude that this phase transition is of first order. This fits to the abrupt change of the ordering parameter, i.e., of the average terrace length.

Due to the large periodic (average) units and their small changes involved in this phase transition, it would be extremely difficult to detect such a transition with a local method, such as tunneling microscopy, and has indeed not been seen.<sup>15,17</sup> It means to add one row of atoms every six terraces *on average* in a fluctuating system. Therefore, averages over several hundred terraces are necessary to safely detect such a small change, which in addition is not static on STM time scales. The present study has nicely demonstrated that such a clarification of the nature of a phase transition on a mesoscopic scale can be reliably done only by diffraction.

Pb in the monolayer regime on the Si(557) surface has the intriguing effect that it stabilizes step formation and, thus, the formation of facets with step densities higher than that of the macroscopic orientation.<sup>14</sup> The coverage dependent variation in step density is compatible with a model that assumes that step decoration, however, is avoided, so that an increase in Pb concentration leads to a reduction in step density until formation of a second layer starts and the steps are also filled with Pb at concentrations above 1.4 ML. As concluded from recent ARPES measurements for the 1.30 ML concentration of Pb,<sup>19</sup> there is a clear electronic component in the stabilization of enhanced step densities, at this concentration of the (223) facet orientation. At  $E_F$ , a gap of around 20 meV is opened in the  $[\bar{1}\bar{1}2]$  direction for the Pb-induced (223) facets due to perfect Fermi nesting for exactly this orientation. A gap of this size is expected for a transition temperature of 78 K seen here and also in conductance measurements.

Excitation of electrons across this gap is obviously coupled with a destabilization of the (223) facet in favor of

the (17 17 25) facet with a lower step density. While this small change in periodicity leads to a breakdown of the Fermi nesting condition and to a transformation of one-dimensional to two-dimensional conductance, it directly demonstrates the strong coupling between electronic and vibrational degrees of freedom.

Therefore, lattice entropic effects are also not negligible. The increase in the average interterrace distance by about 4% can be interpreted as a result of an increased entropic repulsion due to an enhanced meandering of steps.<sup>25</sup> Strong fluctuations are indeed expected for Pb at upper step sites because of the low Debye temperature and are supported by recently performed STM measurements that showed the  $3 \times 3 \rightarrow \sqrt{3} \times \sqrt{3}$  transition for the Pb/Si(111) system.<sup>26</sup> On the other hand, this entropic contribution is monotonously increasing with temperature and does not account for the preferred average terrace length at high temperature seen in our experiments.

To some extent, however, an increase in temperature acts in the same direction as an increase in Pb concentration, since both an increase of concentration and the temperature enhanced entropic interactions lead to an increase in step-step repulsion. This is seen from measured changes in the vicinality as a function of coverage at a constant temperature of 70 K. Starting with the (1,5) phase, the Pb coverage was increased up to 1.42 ML in steps of 0.01 ML, which resulted in the same change in the vicinality of the (223) facet as that found above by increasing  $T$  above  $T_c$  at the constant coverage of 1.3 ML.<sup>22</sup>

In contrast, the decrease in the domain wall splitting along the terraces by approximately 4% above  $T_c$  would correspond, according to our coverage calibration,<sup>14</sup> to a change by only 0.01 ML Pb. This puzzling finding is consistent with the coverage dependent changes in the  $[\bar{1}\bar{1}2]$  direction, assuming that only the (light) domain walls suffer from the excess Pb, whereas the  $\sqrt{3} \times \sqrt{3}$  are left unchanged, supposing a homogeneous distribution along the  $[\bar{1}\bar{1}0]$  direction.

## V. SUMMARY

Summarizing, we studied a temperature-driven structural phase transition observed for 1.3 ML Pb adsorbed on Si(557), which was identified as a refacetting phase transition. The annealed Pb layer causes a refacetting of the initial inclination into a (223) facet structure at low temperatures. Increasing the temperature leads to the formation of high index facets, which we identified as (17 17 25) facets. These results demonstrate the close electronic and lattice vibrational coupling in these low-dimensional systems. Both electronic and entropic contributions that lead to an order-order transition were identified. Furthermore, from a mesoscopic point of view, the energetics might be described in terms of surface stress, i.e., the difference in surface stress of the (223) faceted areas and larger (111) terraces may lead, in addition, to a reduction of the free energy. However, to elucidate the precise interplay of these different energetic contributions, theoretical calculations are necessary.

## ACKNOWLEDGMENTS

The financial support by the Deutsche Forschungsgemeinschaft is gratefully acknowledged.

- <sup>1</sup>J. Voit, Rep. Prog. Phys. **58**, 977 (1995).
- <sup>2</sup>S. Roth and C. Caroll, *One Dimensional Metals* (Wiley-VCH, Weinheim, 2004).
- <sup>3</sup>J. R. Ahn, H. W. Yeom, H. S. Yoon, and I.-W. Lyo, Phys. Rev. Lett. **91**, 196403 (2003).
- <sup>4</sup>J. N. Crain, A. Kirakosian, K. N. Altmann, C. Bromberger, S. C. Erwin, J. L. McChesney, J.-L. Lin, and F. J. Himpsel, Phys. Rev. Lett. **90**, 176805 (2003).
- <sup>5</sup>J. N. Crain and F. J. Himpsel, Appl. Phys. A: Mater. Sci. Process. **82**, 431 (2006).
- <sup>6</sup>U. Schwingenschlöggl and C. Schuster, Europhys. Lett. **81**, 26001 (2008).
- <sup>7</sup>O. Gurlu, O. A. O. Adam, H. J. W. Zandvliet, and B. Poelsema, Appl. Phys. Lett. **83**, 4610 (2003).
- <sup>8</sup>N. Oncel, A. van Houselt, J. Huijben, A.-S. Hallbäck, O. Gurlu, H. J. W. Zandvliet, and B. Poelsema, Phys. Rev. Lett. **95**, 116801 (2005).
- <sup>9</sup>E. Peierls, *Quantum Theory of Solids* (Clarendon, Oxford, 1955), p. 108.
- <sup>10</sup>H. W. Yeom, S. Takeda, E. Rotenberg, I. Matsuda, K. Horikoshi, J. Schaefer, C. M. Lee, S. D. Kevan, T. Ohta, T. Nagao, and S. Hasegawa, Phys. Rev. Lett. **82**, 4898 (1999).
- <sup>11</sup>J. R. Ahn, J. H. Byun, H. Koh, E. Rotenberg, S. D. Kevan, and H. W. Yeom, Phys. Rev. Lett. **93**, 106401 (2004).
- <sup>12</sup>Y. Nakamura, H. Kawai, and M. Nakayama, Phys. Rev. B **55**, 10549 (1997).
- <sup>13</sup>J. M. Carpinelli, H. H. Weitering, E. W. Plummer, and R. Stumpf, Nature (London) **381**, 398 (1996).
- <sup>14</sup>M. Czubanowski, A. Schuster, S. Akbari, H. Pfnür, and C. Tegenkamp, New J. Phys. **9**, 338 (2007).
- <sup>15</sup>C. Tegenkamp, Z. Kallassy, H. Pfnür, H.-L. Günter, V. Zielasek, and M. Henzler, Phys. Rev. Lett. **95**, 176804 (2005).
- <sup>16</sup>C. Tegenkamp, Z. Kallassy, H.-L. Guenter, V. Zielasek, and H. Pfnür, Eur. Phys. J. B **43**, 557 (2005).
- <sup>17</sup>H. Morikawa, K. S. Kim, D. Y. Jung, and H. W. Yeom, Phys. Rev. B **76**, 165406 (2007).
- <sup>18</sup>C. Tegenkamp and H. Pfnür, Surf. Sci. **601**, 2641 (2007).
- <sup>19</sup>C. Tegenkamp, T. Ohta, J. L. McChesney, H. Dil, E. Rotenberg, H. Pfnür, and K. Horn, Phys. Rev. Lett. **100**, 076802 (2008).
- <sup>20</sup>K. Budde, E. Abram, V. Yeh, and M. C. Tringides, Phys. Rev. B **61**, R10602 (2000).
- <sup>21</sup>S. A. Teys, K. N. Romanyuk, R. A. Zhachuk, and B. Z. Olshansky, Surf. Sci. **600**, 4878 (2006).
- <sup>22</sup>A. Schuster, M. Czubanowski, H. Pfnür, and C. Tegenkamp (unpublished).
- <sup>23</sup>K. S. Kim, H. Morikawa, W. H. Choi, and H. W. Yeom, Phys. Rev. Lett. **99**, 196804 (2007).
- <sup>24</sup>J. Wollschläger and C. Tegenkamp, Phys. Rev. B **75**, 245439 (2007).
- <sup>25</sup>X. S. Wang, J. L. Goldberg, N. C. Bartelt, T. L. Einstein, and E. D. Williams, Phys. Rev. Lett. **65**, 2430 (1990).
- <sup>26</sup>I. Brihuega, O. Custance, R. Perez, and J. M. Gomez-Rodriguez, Phys. Rev. Lett. **94**, 046101 (2005).



# Kapitel 8

## Metal insulator transition: Influence of excess coverage and B-field

As seen in chapter 6, Pb monolayers form a variety of different structural phases. In particular our detailed LEED study has shown, that the initial vicinality of the Si(557) substrate can be changed from (112),(335),(223) to (557) for Pb coverages between 1.2 and 1.6 ML. The most striking result, however, is that the (557) orientation is only metastable. Instead, the (223) facet with a terrace lengths of  $4\frac{2}{3}$  atomic units along the  $[\bar{1}\bar{1}2]$  direction is found. Along the  $[1\bar{1}0]$  direction characteristic Pb  $\sqrt{3} \times \sqrt{3}$  were found, separated by  $\sqrt{7} \times \sqrt{3}$  domain walls. For a coverage of 1.31 ML, where the transport reveals a 1D regime and which is considered as the starting point for the following discussion, a so-called (1,5) phase is formed, i.e five  $\sqrt{3} \times \sqrt{3}$  units are separated by one domain wall, yielding the 10-fold periodicity seen in STM and LEED.

The stabilization of the (223) facet structure has been explained by Fermi nesting in this highly anisotropic phase. The detailed analysis of the band structure along the  $[\bar{1}\bar{1}2]$  direction has revealed, that the Fermi wave vector  $k_F$  is related via  $2k_F = g$  with a reciprocal lattice vector  $g$  defined by the inter chain distance  $d$ . This finding has dramatic consequences towards the electronic structure and hence for the transport properties. This nesting at the Fermi surface is accompanied with the opening of a mini-band gap in the order of 20meV, i.e. the system becomes insulating along the  $[\bar{1}\bar{1}2]$  direction. This is just a more sensational description for any insulator. In our case a 2D metallic, but mesoscopically modulated surface becomes insulating.

As mentioned, the insulating regime in the direction perpendicular to the step direction is a consequence of the perfect Fermi nesting condition. However, the gap is not fundamental, i.e. in the direction along the wires split-off states appear, which intersects the Fermi energy and are responsible for the high metallic conductance found in transport measurements. As shown in the last section, the

nesting condition can be destroyed by increasing the substrate temperature. The emphasis of this section is towards the impact of excess coverage. Starting with 1.31ML as the ideal coverage for 1D transport, additional coverage up to 0.1 ML leads to the formation of a charge density wave (CDW). As will be shown, the adsorption even smallest amount of excess coverage leads to a long range ordered decoration of the step structure. The gradual shrinking of the former gap of 20 meV is supported by transport measurements across the step direction. Finally, first magnetotransport results will be presented. Besides the finding that the 1D regime can be destroyed also by applying a magnetic field, a resonance in conductance as a function of the external magnetic field has been found, which demonstrates that the magnetic energy, which is usually not considered in purely 2D systems, play a role in these confined systems.

## 8.1 Suppression of the phase transition

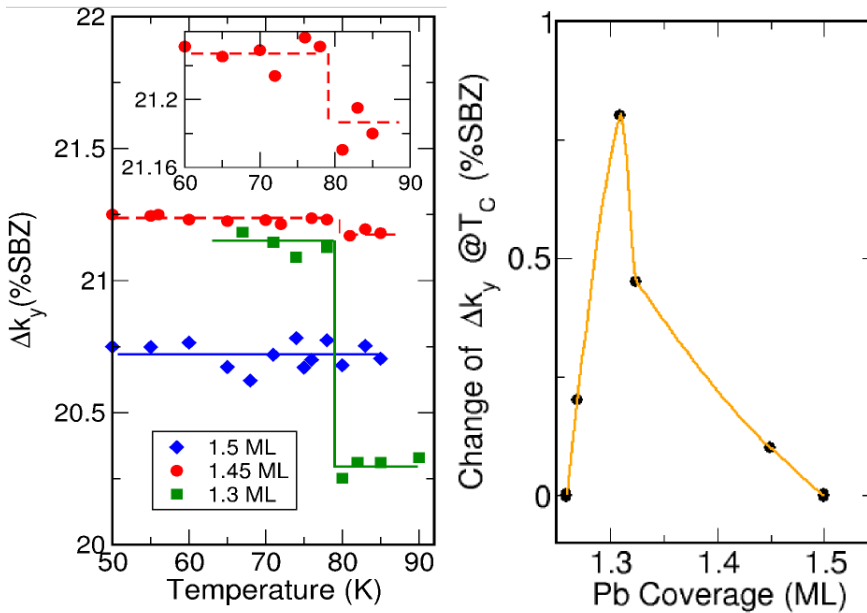


Abbildung 8.1: a) Change of  $\Delta k_y$  as a function of temperature for three different initial Pb coverages. Inset shows magnification of the measurement for 1.45ML b) The  $\Delta k_y(76K) - \Delta k_y(82K)$  as a function of Pb coverage. The structural phase transition is seen most intense for 1.31 ML.

Starting with the (1,5) linear phase corresponding to 1.31 ML Pb, we have deposited excess Pb at 80 K. For the new phases, the facet orientation as a function of the substrate temperature has been analyzed by measuring the spot splitting  $\Delta k_y$  of the former (223) facet along the  $[\bar{1}\bar{1}2]$  direction. The results for 1.31 ML, 1.45 ML and 1.5 ML are shown in Fig. 8.1a). The strong phase transition at 78 K



for the 1.31 ML coverage, as discussed in detail in chapter 7, vanishes gradually by increasing the Pb coverage. For the 1.5 ML phase, where according the results of chapter 6 nearly every step of the former (223) facet is decorated, the absolute value of the spot splitting decreases, too, i.e. the average terrace lengths is slightly increasing. The additional Pb concentration obviously destabilizes the nested (223) facet orientation. In general, this trend is consistent with the metastable (557) facet found for coverages above 1.5ML (cf. with chapter 6).

This suppression of the refacetting is intimately related with the transport properties. In Fig. 8.2 are shown conductivity measurements for both directions as a function of the substrate temperature for  $\Theta = 1.31ML$  and  $\Theta = 1.32ML$ . Clearly visible here is that the switching between the 1D- and 2D transport regime is less pronounced as the coverage is slightly increased. It should be noted, that for 1.4ML Pb the switching is totally suppressed in transport. In Fig. 8.2b) is plotted the the change of the 1D/2D switching in the  $[\bar{1}\bar{1}2]$  direction for different coverages. The similarity with Fig. 8.1b) is obvious and supports the strong correlation between structure and transport.

As shown in the supplement of chapter 6, additional Pb starts to decorate the steps. From the findings in chapter 6 and 7, the (111) mini facets are covered by a full physical mono layer, neglecting the  $\sqrt{7} \times \sqrt{3}$  domain walls. The previous investigation has shown, that the domain splitting saturates at 8%SBZ for 1.34 ML, i.e. due to the lattice mismatch between Pb and Si the stripe incommensurate phase (SIC) is the most dense covering. Therefore, any excess coverage will grow on top, presumably at the high coordinated step edge sites. This decoration causes the breakdown of the former nesting condition.

Evidence that the nesting is destroyed for higher Pb coverages, is supported by the increase seen in conductance shown in Fig. 8.3 for the conductivity  $\sigma_{\perp}$  measured along the  $[\bar{1}\bar{1}2]$  direction. All data were taken at 30K. Whereas for 1.31ML the conductance is almost zero, i.e. is determined by the residual conductivity of the substrate, the values increase slightly and has a comparably high value at 1.4 ML. Moreover, the logarithmic dependency that is linear with increasing coverage support the theory of band filling and effectively reducing the band gap.

## 8.2 Formation of superlattices on vicinal surfaces

Any excess coverage of Pb on top of the (1,5)–linear phase starts to decorate the steps forming superlattices even at low deposition temperatures. In this case the substrate temperature was around 75 K. The additional ordering along the  $[\bar{1}\bar{1}2]$  direction can be seen by satellite peaks around the step diffraction peaks of the (223) facet structure. According to the average terrace length of  $4\frac{2}{3}$  atomic units in the  $[\bar{1}\bar{1}2]$  direction the spot splitting of the (1,5)–phase amounts to 21.3 %

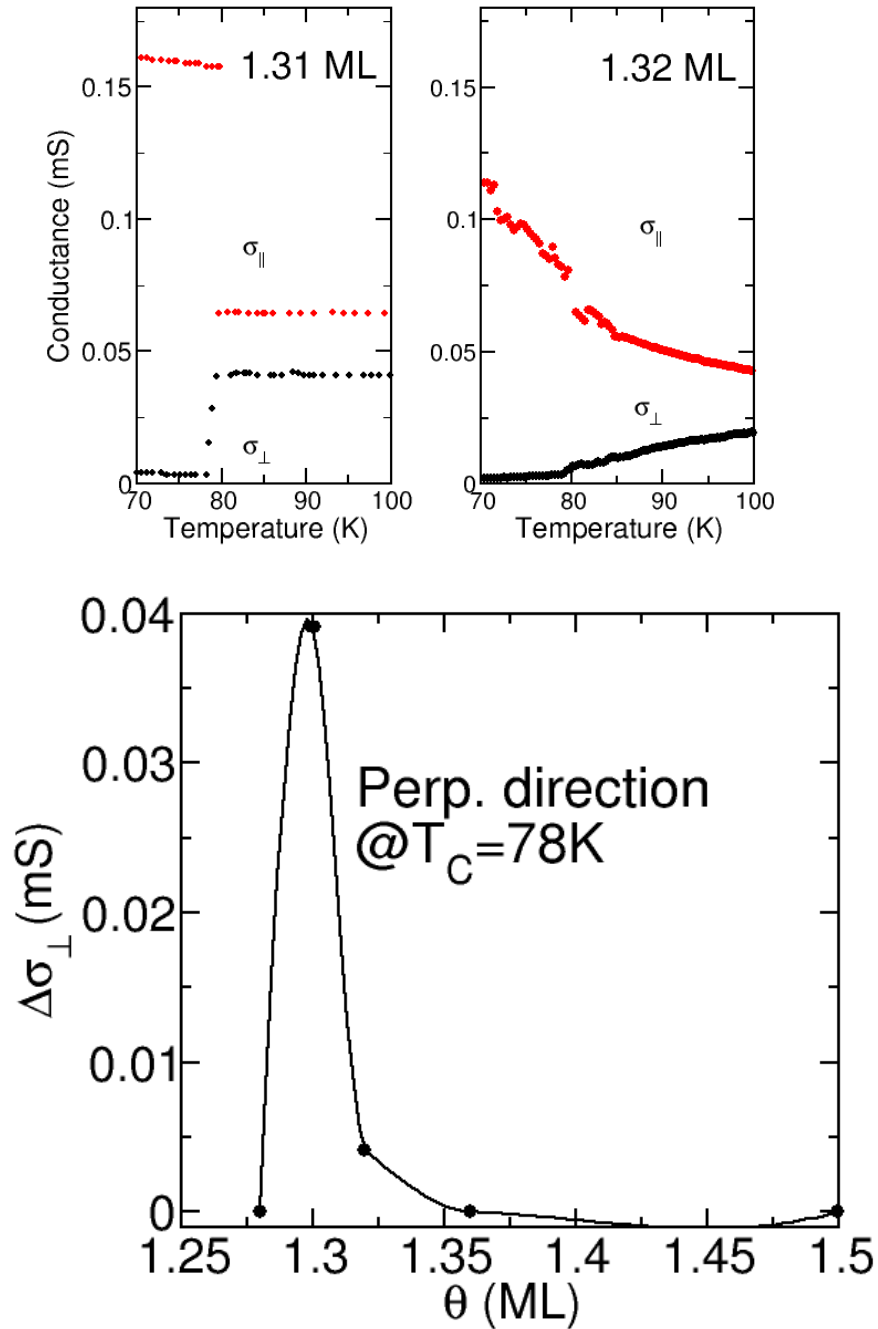


Abbildung 8.2: a) Conductivity measured along and across the wires as a function of temperature for two different coverages. b)  $\sigma_{\perp}(T = 82\text{K}) - \sigma_{\perp}(70\text{K})$ .

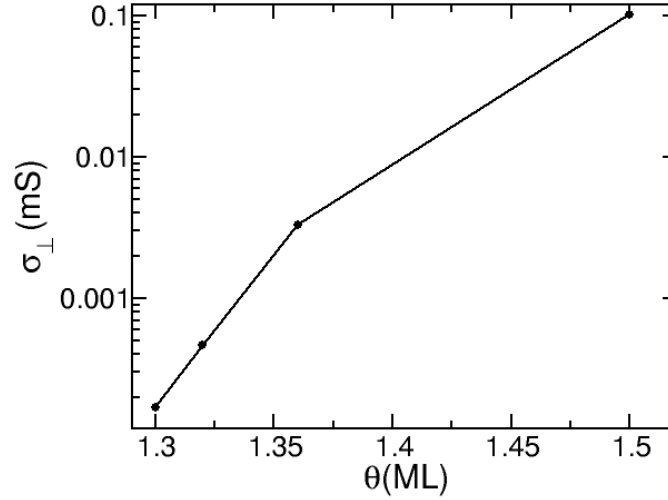


Abbildung 8.3: (color online) log of  $\sigma_{\perp}$  as a function of coverage. The conductivity data were taken at 30 K.

SBZ (below 80K). As obvious from Fig. 8.4a) additional peaks appear while excess coverage is deposited. Furthermore, the satellite peaks change in position as the coverage is changed indicating that the additional ordering is induced by the excess coverage. However, the peaks stemming from the (223) facet structure, do not change in position. Assuming a simple rigid band model, unoccupied states should be filled up by electrons stemming from the excess coverage and, finally, destabilize this phase as the Fermi nesting breaks down.

Quantitatively, the peak positions of the satellites ( $\Delta k_{deco}$ ) corresponds to multiples of the average terrace length. E.g., for 1.34ML Pb coverage, the splitting is 5.3% SBZ, i.e. the lattice factor is modulated by  $4\Gamma_{223}$ . The spot profiles have been evaluated as shown in Fig. 8.4b) exemplarily for 1.34 ML coverage. Qualitative agreement has been obtained using gaussian functions (shaded peaks in Fig. 8.4b) in addition to the (dashed marked) functions representing the (223) facet structure. However, two further functions (solid marked) were needed in order to stabilize the fit. The functions are exactly in between the (00)-peak and the first order peaks of the  $4\Gamma_{223}$  periodicity and, thus, decoration of only every eighth step might be reasonable, because the coverage of 0.04 ML is somewhat too low to decorate all step sites. Because of this remaining uncertainty with respect to the absolute coverage, the comparably broad peak structure of the nominally perfect (223) facet structure (cf. with broken arrow in lowest curve in Fig. 8.2a)

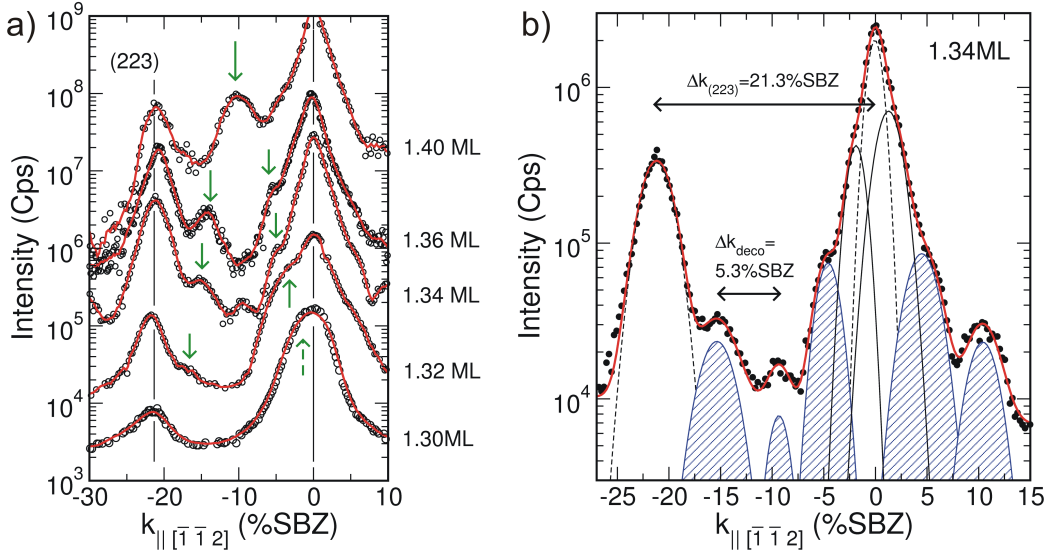


Abbildung 8.4: (color online) (a) Line scans taken along the  $[\bar{1}\bar{1}2]$  direction for Pb coverages between 1.31 and 1.4 ML. The adsorption was done at 75 K substrate temperature. (b) From a detailed spot profile analysis the new periodicity can be accurately determined as shown exemplarily for 1.34 ML. For details see text.

may contain also satellite peaks of even extraordinarily long-range ordered phases ( $> 10\Gamma_{223}$ ).

The spot splitting of the superlattice periodicity has been analyzed in detail and plotted versus the Pb excess coverage with respect to 1.31 ML (cf. with Fig. 8.4). The wave vectors have been calculated via  $\frac{\Delta k_{decco}}{100} \cdot \frac{2\pi}{a}$ , where  $a=3.32 \text{ \AA}$  is the lattice unit vector in the  $[\bar{1}\bar{1}2]$  direction. It should be emphasized that excess coverage of the order of 1% leads already to long range ordered structures. As the adsorption was done at low temperatures, the diffusion constant must be quite high. For Pb/Si(111) extraordinary high diffusion constants have been reported [48, 49]. The FWHM of the peaks from the superlattice are comparable to the FWHM of the (223) facet structure, i.e. the ordering of the long-range ordered phase is limited by the perfectness of the underlying facet structure. Therefore, it can be concluded that even the Schwoebel barriers are extremely low so that diffusion across the steps is very effective also at low temperatures.

Well ordered phases due to long-range repulsive interaction have been found for densely packed monolayer structures of Pb on Si(111) [50]. For these so-called devil's staircase phases more or less infinite numbers of different structures can be formed with minute changes in coverage, as it is always possible to rearrange the atoms into new pattern and lower the energy [51]. In this case of Pb/Si(557) a similar mechanism has been seen on the mini-(111) terraces as well [7]. However, for the  $[\bar{1}\bar{1}2]$  direction across the steps the situation is obviously different, because

the superlattices are pinned to the step structure. Furthermore, only even-integer step sites are decorated. Other step decoration turns out to be only metastable. A hint is given by the inspection of the curve corresponding to 1.36 ML in Fig. 8.4a). From the excess coverage a decoration of every third step is expected, however, the splitting is quite similar to the 1.34 ML case suggesting that this phase is not stable (cf. also with data point for 1.36 ML (open circle) in Fig. 8.5a).

As the (111)-sites are all saturated by a densely packed Pb adlayer, it is assumed that the step decoration takes place at the step sites. A hint toward the decoration is the vanishing of the half-order spots in LEED. While coverages below 1.31 ML results in a so-called spotty  $\alpha \times 2$  reconstruction [52], 1.31 ML show a streaky reconstruction. As explained in detail in **chapter 4**, the  $\times 2$  reconstruction stems from the dimerization at the Si step sites. For 1.55 ML the half order spots are not visible any longer, i.e. the adsorption of the excess Pb takes place presumably at step sites. Furthermore, as the comparison with the (simple) theory presented below shows, the excess Pb grow with the lattice constant of Si, i.e. coverage is by 1/1.3 lower to form a densely packed chain at the step site.

In order to explore the origin for the long range ordering, the Fermi wave vector  $k_F$  has been estimated (cf. with solid (blue) curve in Fig. 8.4a). As plotted in Fig. 8.4 there is a qualitative agreement in between the calculated Fermi wave vector and the wave vector obtained from diffraction experiments. This finding suggests that electron-electron interaction is responsible for the long range ordered phase. The Fermi wave vector have been calculated assuming a 2d electron gas ( $k_F = \sqrt{2\pi n}$ ). The electron density  $n$  was calculated from the Pb excess coverage assuming one electron per Pb atom. Perfect agreement between both quantities in Fig. 8.5a) is obtained if every Pb atom donates 0.8 electrons. Interestingly, there is a nice correlation between the electronic and structural quantity suggesting that the ordering is driven by, indeed, by an electron-electron interaction. The electronic properties of this superlattices are examined by transport studies presented in the next section.

### 8.3 Transport properties of the superlattice structure

The formation of the superlattice should be accompanied by the formation of new mini-bands with new characteristic band gaps. As detailed ARPES measurements are missing for this coverage regime, we can discuss only possible scenarios relying on the electronic band structure obtained for 1.31 ML, i.e. where Fermi nesting occurs.

The adsorption of Pb onto the (1,5) phase decorates steps and donates the system with electrons. As the 1D/2D transition is still seen after adsorbing a very small amount of lead (cf. with Fig. 8.2 0.02 ML excess coverage) the new band gaps

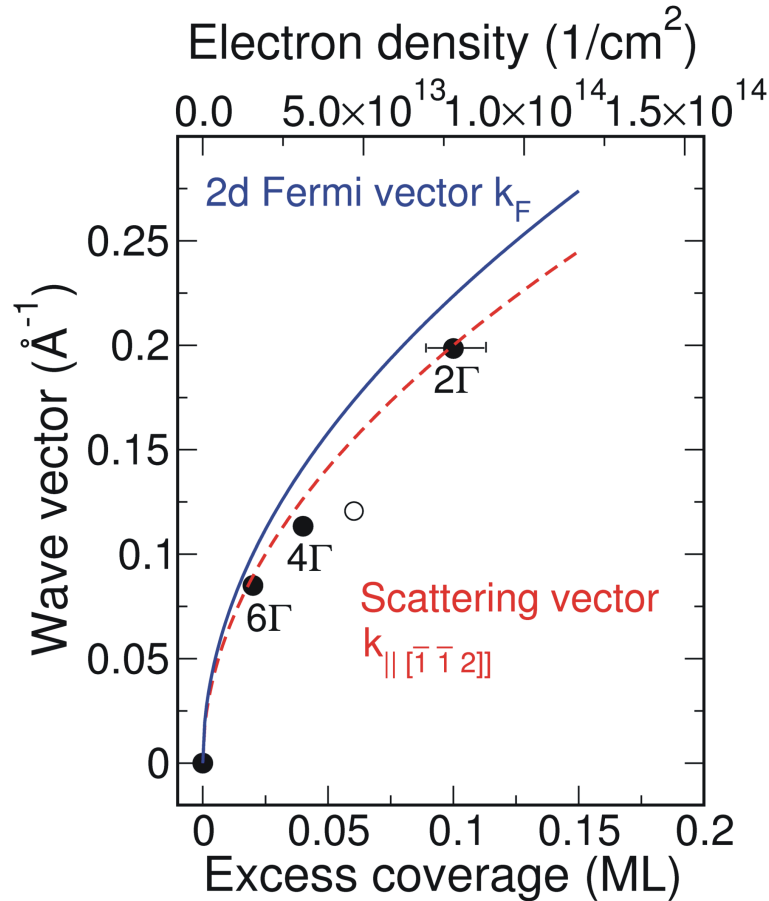


Abbildung 8.5: (color online) (a) Plot of the satellite periodicities seen in Fig. 8.2 versus the Pb excess coverage (relative to 1.31ML). Circles denote the structure step decoration and the dashed (red) line is a best fit. The solid (blue) curve represents the Fermi wave vector  $k_F$  assuming an (isotropic) 2d gas of electrons induced by the excess coverage. The valence state was assumed to be +1.

will be very small, i.e. eventually too small to be resolvable with ARPES. More sensitive are transport studies.

It turns out, that the order of the superlattices is imperfect with respect to the order of the 1.31ML phase, i.e. whereas for the latter phase a clear transition is seen in a macroscopic transport measurement, for the superlattice structure the gap is reflected by the activation energy needed to perform transport along the disordered phase. Indeed, the activated regime below  $T_c$  is seen for different excess coverages as shown in Fig. 8.6. For instance, in Fig. 8.6 for 1.36 an exponential increase is seen in this temperature range. It should be noted, that, at this point, only the data below  $T_c$  can be evaluated accurately. The measurements shown in Fig. 8.6 do not belong to the same series, i.e. depending on the exact treatment

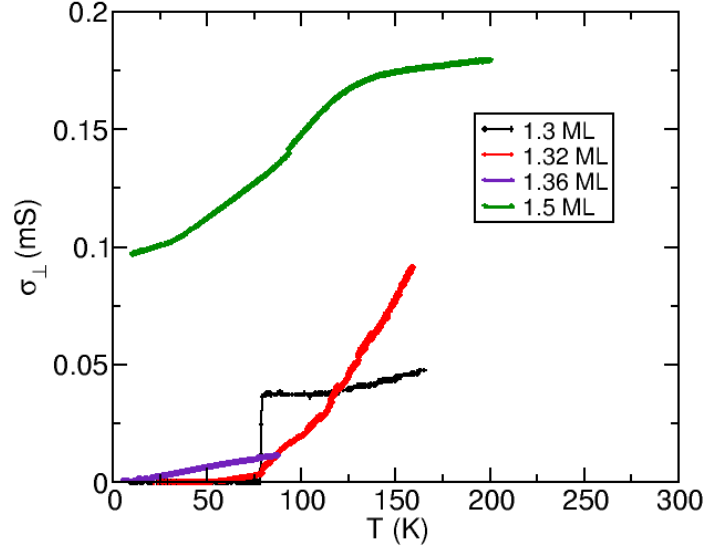


Abbildung 8.6: (color online)  $\sigma_{\perp}$  as a function of temperature for different Pb phases in the 1D and quasi 2D regime.

of the (different) samples the bulk contributes differently at higher temperatures, e.g. at 150K the conductance of 1.32 ML is higher than for 1.31 ML.

In Fig. 8.7 the conductance (on a logarithmic scale) versus the inverse temperature of this low temperature regime is plotted. The fitting reveal an activation energy close to 4.7 meV, significantly lower than the band gap of 20meV for 1.31ML. The evolution of the band gap can be better seen by plotting the  $\ln(\sigma_{\perp})$  as function of  $\frac{1}{T}$  in the temperature range that is below the  $T_c$  8.7. The sudden increase of the conduction around 60K (marked with blue dashed line on fig. 8.7) for 1.32 ML is attributed to the ionization energy of the dopant (in our case it was Bor) of the silicon surface which is equal to 45 meV. Eventually, due to too many flash cycles of the sample during the sample preparation, the dopant concentration has been increased accidentally.

Fig. 8.8 shows finally the 'gaps' of the different Pb phases obtained by transport and spectroscopy. In agreement with the model presented above, the superlattice formation is associated with a new band structure. The system is energetically stabilized by the opening of mini-gaps at the Fermi energy. This conclusion is in agreement with the finding, that the (223) facet orientation is sustained upon the deposition of excess coverage.

It was mentioned that most likely even-integer step sites are occupied by the excess coverage. As the determination of  $k_F$  for this system (see above) was

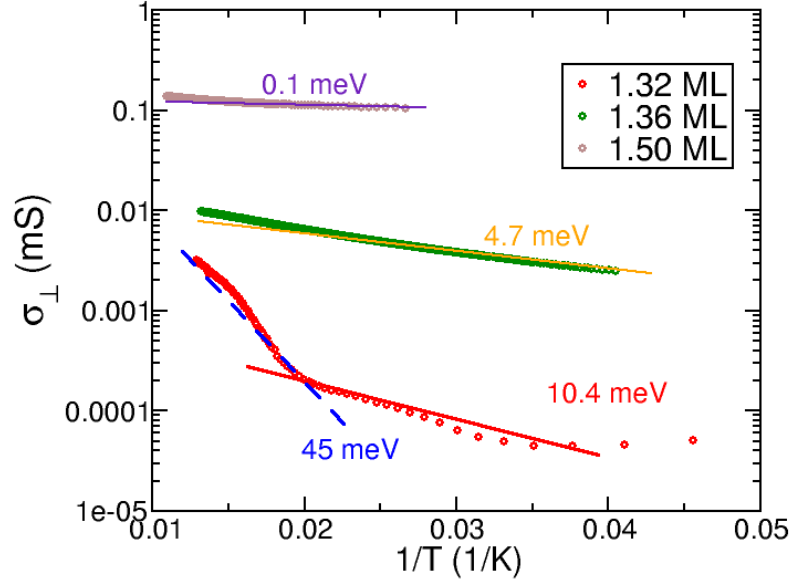


Abbildung 8.7: (color online) Natural logarithm of conductivity as a function of inverse temperature for different coverages. The slope of linear fit is proportional to the energy gap in meV.

done without any assumptions about the ordering, the model can be checked independently by calculating the amplitude modulation of the new electronic wave function. Fig. 8.9) shows the result obtained after the in-phase overlay of plane waves modeled by  $\cos(k_F\Gamma)$  of hundred adjacent unit cells. The maxima corresponds perfectly to the separation, which has been measured with SPA-LEED. It should be noted that an indirect interaction between the superperiodic chains via Friedel oscillations of the electron density, i.e.  $\cos(2k_F\Gamma)$  results in an incorrect periodicity. The formation of the superlattices is therefore a direct consequence of the constructive interference of plane waves, i.e. the formation of new band structures, which is expected for superlattice structures. As the ordering is a result of an electron-electron interaction the problem can be treated also a  $4k_F$  CDW-distortion, i.e. the band filling with the associated periodicity can be expressed via  $g = 4k_F$  in terms of the Fermi wave vector  $k_F$  and the reciprocal lattice vector  $g = 2\pi/\Gamma_{223}$ . In general this is accompanied by lifting the spin degeneracy causing enhanced spin-orbit interactions. As shown in the next section, indeed, there are strong hints towards an increased SO-interaction as weak anti-localization has been found in magnetoresistance measurements in this coverage regime.

The periodicity that has been observed for the quasi-2D regime supports also the



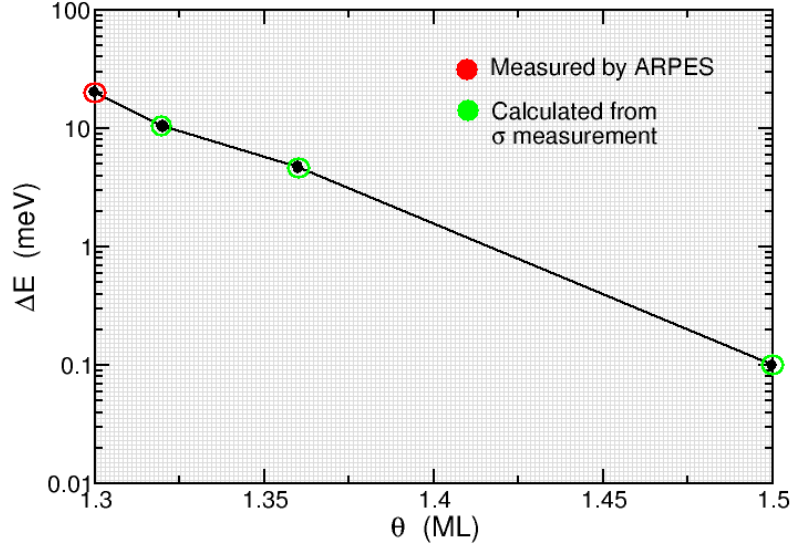


Abbildung 8.8: (color online) Energy gap estimated from the slope of the log conductance as function of inverse temperature.

observation that has been made in the section before, where linear dependency between log of  $\sigma$  and coverage has been shown. This characteristic gives clear evidence for band filling, what effectively reduces the band gap i.e. insulating behavior between the chains. This extra periodicity as mentioned is the case of  $4k_F$  CDW - distortion that is interfering with the Fermi nesting phase.

## 8.4 Magnetoresistance measurements

In order to address the question of spin-orbit interaction in more detail, first magnetoresistance measurements have been performed. In particular the conductivity in the  $[\bar{1}\bar{1}2]$  direction has been analyzed as a function of the magnetic field for different Pb coverages. The result is shown in Fig. 8.10

As reference, we have measured a 6ML thick Pb, which will be presented first. After annealing LEED reveals a 12-fold pattern originating from Pb(111) crystallites in two different orientations. For these thick films, the underlying stepped structure is simply overgrown. The average terrace size is around 40nm revealed from the FWHM of the (00) peak taken at an out-of phase condition. Further details about the multilayer growth of Pb on Si(557) can be found in [53]. As can be seen in Fig. 8.10, for these multilayer structures a negative magnetoresistance

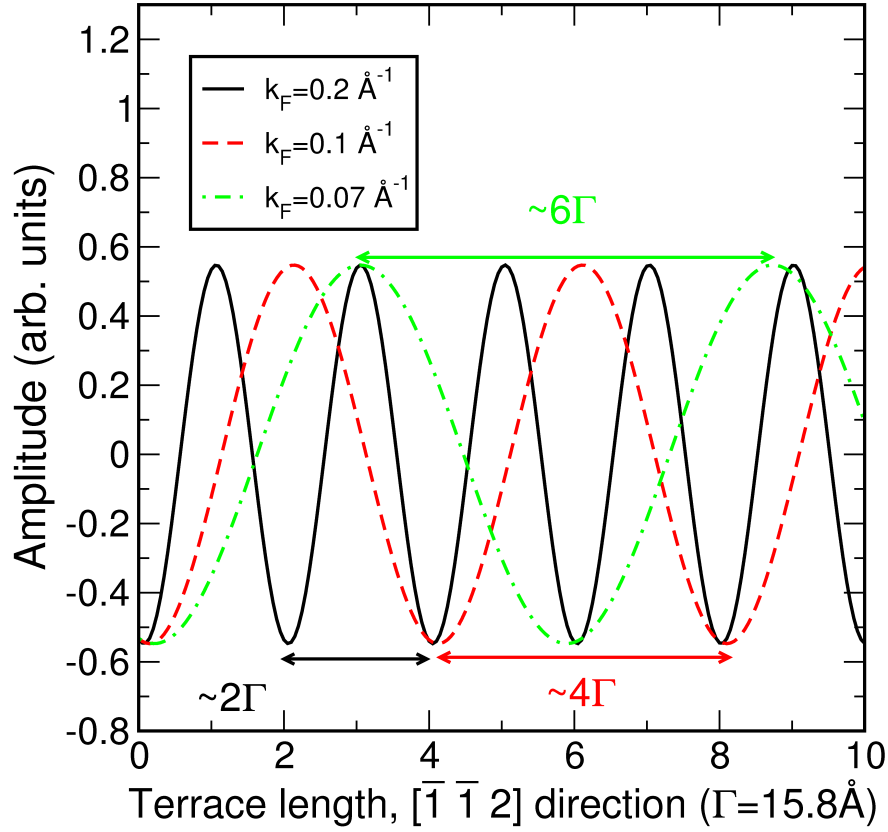


Abbildung 8.9: (color online) Modulation of the amplitude versus the crystal position. The modulation of plane waves, i.e.  $\cos(k_F r)$ , has been calculated taking hundred unit cells into account. For further details see text.

can be observed, i.e. scattering is dominated by weak localization causing an enhanced resistance at zero magnetic field. The direct consequence of this observation is, that elastic scattering occur in between inelastic scattering events ( $\tau_0 > \tau_i$ ).

For monolayer phases, representing the 1D and quasi-2D regime, completely different transport behaviors are found. Starting with the 1D regime (1.32ML) a magnetic resonance around 1.5 T can be seen. Apart, the background increases gradually as the magnetic field is increasing. Although the change in conductance is plotted, one should keep in mind, that the absolute conductance is close to zero, as well, for this ideal coverage. This uniquely shows, that the nesting condition can destroyed simply by applying a magnetic field. The easiest explanation can be given in terms of the Zeeman energy. As the magnetic field is applied, the electronic states are shifted energetically. As the bands intersects the Fermi energy with a finite slope, the Zeeman energy leads inevitably to Fermi vectors such that  $g \neq 2k_F$ .

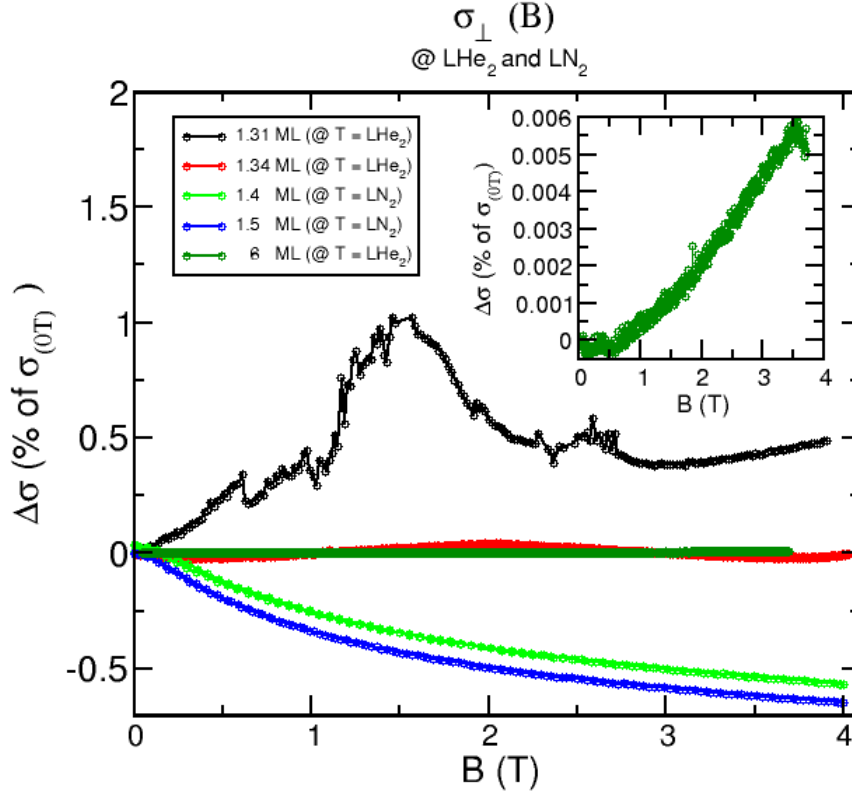


Abbildung 8.10: (color online)  $\sigma_{\perp}$  as a function of the external magnetic field for different Pb phases in the 1D and quasi 2D regime.

We have mentioned above, that the 1D phase can be doped to some extent. The effect of doping for the 1D phase is shown in Fig. 8.10, too. Besides the fact, that the slope of the background decreases (see below) the maximum of the resonance shifts to higher magnetic fields (2 T). We have seen above, that doping at this level already enables transport in the  $[\bar{1}\bar{1}2]$  direction, i.e. by changing the filling factor the nesting condition has been changed. Assuming that still a 1D signature of this phase can be seen in magnetotransport, it turns out that because of the higher electron density the magnetic field has to be increased. In terms of magnetic length ( $\ell_B = \text{sqrt}(\hbar/eB) = 20 \text{ nm}$ ) is an order of magnitude higher than the width of the atomic wires (1.5nm).

# Kapitel 9

## Summary and outlook

The combination of SPA-LEED and conductivity measurements allows to investigate the structure and the electrical properties of thin Pb layers grown on Si(557) surfaces. In particular, with SPA-LEED a detailed phase diagram has been measured as a function of the Pb coverage, but also as function of the temperature. The phase diagram considers the coverage range between 1.2 and 1.6 ML, where strong refaceting has been found. The original Si(557) step orientation could be changed from (112) to a (223) facet orientation. This behavior suggests strong coupling between the structures of both Pb and Si(557) with their electronic configuration. As the refaceting costs energy, it can only be gained via modifications of the electronic structure, i.e. the surface states. This has been achieved by destroying the (7x7) reconstruction of the surface substrate. Unlike the Au/Si(557) system [54], in case of Pb, the surface orientation is modified upon adsorption. An important observation is, that Pb induced (557) orientation with a regularly distributed terraces of  $5\frac{2}{3}a_{Si}$  is only meta-stable. Also the atomic configuration within the wires has been successfully determined. It has been shown that alike for the Pb/Si(111) system, also here the devil's staircase regime has been observed in a similar coverage range. The development of the devil staircase phases modify the surface energies so that only as less as 0.01 ML of Pb can rearrange the periodicity along the wires. Thereby, only the terraces are decorated with Pb atoms. The steps remain undecorated what is indicated by the 2x1 step reconstruction, which is also present on the clean Si surface. First step decoration is observed only for the coverages above 1.3ML.

All signatures and phase transitions seen in transport, can be related to certain structural properties and phase transitions, respectively. However, as it was shown for many other systems and for the Pb/Si(557) as well, the changes are related to each other. For this particular system, the SPA-LEED has shown its advantages compared to local techniques e.g. STM. The transition at  $T=78K$ , as observed in the conductance, is well correlated with the structural changes of the wire array in the  $[\bar{1}\bar{1}2]$  direction. This also has reflection on the electronic configuration, as confirmed by photoemission experiments. The localized state due to Fermi

nesting below 78 K, which results in uniaxial transport only along the wires, is destroyed above the phase transition. Below 78 K the nesting is associated with the opening of a mini-gap in the order of 20 meV.

Finally, also the influence of excess coverage evaporated on the 1.31ML Pb/Si(557) structure has been investigated in detail by means of SPA-LEED and conductivity measurements. Both the structural phase transition and the switching in transport between 1d and 2d occurs only at a coverage of 1.31ML, i.e. the (1,5) phase. As the coverage deviates by 0.02 ML, the transition is suppressed at all. In addition, starting with the (1,5) phase of Pb/Si(557) surface, increase of the coverage cause decoration of the steps with additional Pb atoms. The experiments performed on (1,5) phase has shown an extra periodicity which is commensurate with the periodicity of the step edges of the (223) facet. This can be either used as a new 1d metallic pattern to study electron transport in such system or can be used for better understanding the physics of the processes that drove the reorientation of the Si(557).

The decoration of the steps induces the new coherent state that can be characterized as charge density waves (like the (1,5) phase of Pb/Si(557)). The extremely long range ordering in the order of 10nm is basically the result of an electron-electron interaction. By judging from the excess electron density induced by the excess coverage, there is again found a relation between the reciprocal lattice vector of the superlattice structure and the Fermi-wave vector. Obviously, instead of filling unoccupied states, new subbands evolve in the former bandgap. The gradual reduction of the band gap with new subbands, depending on the coverage, is seen by activated transport in the direction across the wires.

Furthermore, magneto transport measurements have been performed for the first time on such an uniaxially epitaxial system. Within this experiments, it was possible to distinguish different transport regimes like weak anti localization and strong localization. It was shown further that stability of the quasi-1D state can be influenced by the magnetic field. This clearly demonstrated that the Zeeman energy has to been taken into account for this system. Qualitatively, the magnetic fields leads to an imbalance of the electron distribution within their different electronic states, i.e. the former Fermi-nesting condition is destroyed resulting in transport across the wires. The oscillatory behavior within the magnetoresistance for the quasi-1d regime remains unanswered at this stage. In order to explain this effect further experiments are necessary, in particular the transport along the wires ( also with presence of the magnetic fields oriented in different direction with respect to the plain of the sample) should be performed.

In summary, the Pb/Si(557) is interesting and shows a lot of exciting effects (Peierls like phase transition, tunable CDWs, superlattices, 1d transport). While for many other systems showing a 1d behavior, e.g. Au/Si(557), the reason is due to confinement, the Pb/Si(557) is a strongly 2d interacting system. This fact might be responsible for the richness of effects and the possibility of functionalization, i.e. changes in microscopic structure has an impact on the macroscopic scale as

tested by transport measurements.

# Literaturverzeichnis

- [1] C. Liu *et al.*, Physical Review B (Condensed Matter and Materials Physics) **77**, 205415 (2008).
- [2] J. N. Crain, M. C. Gallagher, J. L. McChesney, M. Bissen, and F. J. Himpsel, Physical Review B **72**, 045312 (2005).
- [3] N. Oncel *et al.*, Phys. Rev. Lett. **95**, 116801 (2005).
- [4] T. Tanikawa, I. Matsuda, T. Kanagawa, and S. Hasegawa, Physical Review Letters **93**, 016801 (2004).
- [5] C. Tegenkamp *et al.*, Phys. Rev. Lett. **95**, 176804 (2005).
- [6] C. Tegenkamp *et al.*, Physical Review Letters **100**, 076802 (2008).
- [7] M. Czubanowski, A. Schuster, S. Akbari, H. Pfnur, and C. Tegenkamp, New Journal of Physics **9**, 338 (2007).
- [8] M. Czubanowski, A. Schuster, H. Pfnur, and C. Tegenkamp, Physical Review B (Condensed Matter and Materials Physics) **77**, 174108 (2008).
- [9] D. Liang, M. R. Sakr, and X. P. A. Gao, Nano Letters **9**, 1709 (2009), <http://pubs.acs.org/doi/pdf/10.1021/nl900424k>.
- [10] S. Teys, K. Romanyuk, R. Zhachuk, and B. Olshanetsky, Surface Science **600**, 4878 (2006).
- [11] A. Kirakosian *et al.*, Appl. Phys. Lett. **79**, 1608 (2001).
- [12] A. Kirakosian *et al.*, Applied Physics Letters **79**, 1608 (2001).
- [13] M. Yakes, V. Yeh, M. Hupalo, and M. C. Tringides, Phys. Rev. B **69**, 224103 (2004).
- [14] A. Petkova, J. Wollschlaeger, H. L. Guenter, and M. Henzler, Surface Science **471**, 11 (2001).

- [15] V. Yeh, M. Yakes, M. Hupalo, and M. Tringides, *Surface Science* **562**, L238 (2004).
- [16] P. W. Anderson, *Phys. Rev.* **109**, 1492 (1958).
- [17] N. F. Mott, *Electronic Processes in Non-Crystalline Materials* (Clarendon Press, New York, 1971).
- [18] W. N. Shafarman and T. G. Castner, *Phys. Rev. B* **33**, 3570 (1986).
- [19] Y. Shapir and Z. Ovadyahu, *Phys. Rev. B* **40**, 12441 (1989).
- [20] J.-L. Pichard, M. Sanquer, K. Slevin, and P. Debray, *Phys. Rev. Lett.* **65**, 1812 (1990).
- [21] E. Abrahams, P. W. Anderson, D. C. Licciardello, and T. V. Ramakrishnan, *Phys. Rev. Lett.* **42**, 673 (1979).
- [22] P. W. Anderson, E. Abrahams, and T. V. Ramakrishnan, *Phys. Rev. Lett.* **43**, 718 (1979).
- [23] L. P. Gorkov, A. I. Larkin, and D. E. Khmel'nitzkii, *JETP Lett.* **30**, 228 (1979).
- [24] D. J. Bishop, D. C. Tsui, and R. C. Dynes, *Phys. Rev. Lett.* **44**, 1153 (1980).
- [25] S. Hikami, A. I. Larkin, and Y. Nagaoka, *Progress of Theoretical Physics* **63**, 707 (1980).
- [26] O. Pfennigstorff, *Quantisierter elektronischer Transport in ultradünnen Bleischichten*, PhD thesis, Universität Hannover, 2001.
- [27] A. Kawabata, *Progress of Theoretical Physics Supplement* **84**, 16 (1985).
- [28] G. Bergmann, *Phys. Rev. Lett.* **49**, 162 (1982).
- [29] K. Fuchs, *Mathematical Proceedings of the Cambridge Philosophical Society* **34**, 100 (1938).
- [30] E. H. Sondheimer, *Phys. Rev.* **80**, 401 (1950).
- [31] A. F. Mayadas and M. Shatzkes, *Phys. Rev. B* **1**, 1382 (1970).
- [32] D. S. Acker and W. R. Hertler, *Journal of the American Chemical Society* **84**, 3370 (1962), <http://pubs.acs.org/doi/pdf/10.1021/ja00876a028>.
- [33] C. Dekker, *Physics Today* **52**, 22 (1999).
- [34] R. Thorne, (1996).



- [35] G. Godzik, T. Block, and H. Pfnür, Phys. Rev. B **69**, 235414 (2004).
- [36] H. W. Yeom *et al.*, Phys. Rev. Lett. **82**, 4898 (1999).
- [37] R. E. Peierls, *Quantum Theory of Solids* (Clarendon, Oxford, 1964).
- [38] W. Tremel and E. W. O. Finckh, *Ladungsdichtewellen* (Wiley-VCH Verlag GmbH, 2004).
- [39] T. Schmidt, *Entwicklung der verbesserten Elektronenbeugungsapparatur.* (, 1989).
- [40] C. Kittel, *Einführung in die Festkörperphysik*, 14 ed. (Oldenbourg, München, 2005).
- [41] M. Henzler and M. Gpel, *Oberflächenphysik des Festkörpers* Teubner Studienbcher, 1 ed. (Teubner, Stuttgart, 1994).
- [42] M. von Hoegen, *Zeitschrift Fr Kristallographie*, 214 ed. (, 1999).
- [43] P. Hofmann and J. W. Wells, Journal of Physics: Condensed Matter **21**, 013003 (21pp) (2009).
- [44] L. J. van der Pauw, Philips Res. Rep. **13** (1958).
- [45] D.-H. Oh *et al.*, Physical Review B (Condensed Matter and Materials Physics) **77**, 155430 (2008).
- [46] O. Pfennigstorf, A. Petkova, Z. Kallassy, and M. Henzler, European Physical Journal B **30**, 111 (2002).
- [47] A. Petkova, *Epitaktische Bleimonolagen auf Si(111)-Oberflächen: Struktur und Defekte*, PhD thesis, Universität Hannover, 2001.
- [48] M. Yakes, V. Yeh, M. Hupalo, and M. C. Tringides, Phys. Rev. B **69**, 224103 (2004).
- [49] M. Yakes, M. Hupalo, M. A. Zaluska-Kotur, Z. W. Gortel, and M. C. Tringides, Physical Review Letters **98**, 135504 (2007).
- [50] M. Hupalo, J. Schmalian, and M. C. Tringides, Phys. Rev. Lett. **90**, 216106 (2003).
- [51] P. Bak, Reports on Progress in Physics **45**, 587 (1982).
- [52] K. S. Kim, H. Morikawa, W. H. Choi, and H. W. Yeom, Physical Review Letters **99**, 196804 (2007).
- [53] E. Hoque, A. Petkova, and M. Henzler, Surface Science **515**, 312 (2002).

- [54] I. K. Robinson, P. A. Bennett, and F. J. Himpsel, *Phys. Rev. Lett.* **88**, 096104 (2002).

# List of abbreviations

2DAG	2D Adatom Gas
2DEG	2D Electron Gas
AES	Auger Electron Spectroscopy
ARPES	Angle Resolved Photoemission Spectroscopy
CITS	Current Imaging Tunneling Spectroscopy
EB-STD	Electron Beam stimulated Selective Thermal Desorption
$E_F$	Fermi-Energy
ESD	Electron Stimulated Desorption
$E_{\text{Vak}}$	Vakuum-Energie
fcc	face centered cubic
FWHM	Full Width at Half Maximum
HTC	Honeycomb Chained Triangle
IET	Inequivalent Triangle
$k_b$	Boltzmann-Konstante
LEED	Low Energy Electron Diffraction
$\text{LN}_2$	Liquid Nitrogen
MBE	Molecular Beam Epitaxy
ML	Monolayer
PMMA	Polymethylmetacrylat
QSE	Quantum Size Effect
SPA-LEED	Spot Profile Analysis LEED
STM	Scanning Tunneling Microscopy
TEM	Transmission Electron Microscopy
$\Theta$	Coverage
UHV	Ultra high Vacuum
UPS	Ultraviolet Photoelectron Spectroscopy
VBM	Valence Band Maximum
XPS	X-ray Photoelectron Spectroscopy

# Kapitel 10

## Acknowledgments

I would like to thank my supervisor Prof. Dr. Herbert Pfnür for giving me the opportunity to continue my scientific work in his laboratory. His support with fruitful discussions, advices and comments were always appreciated.

Special thanks to my second supervisor, PD Dr. Christoph Tegenkamp for patience, that he always had for me. His determination and brilliant motivation techniques were of great support to me. His invaluable help in correction my thesis as well as with experimental setup will never be forgotten.

Special thanks to all my students, that I have supervised during my time at the Surface Science Section of Solid State Physics Institute. I hope, I was not too hard teacher. I wish them all the best in their future.

My successor Daniel Lückermann, I wish all the best and many successful experiments.

Jdrzej Schmeidel, Maciej Cgiel, Tammo Block, Thomas Langer, Dirk Müller-Sajak, Svend Wiessel, Jan Rönspies and Wei Chen for their friendly collaboration.

I would also like to thank the members of the workshop, for their supportive cooperation.

I would like to send special regards to all former coworkers that I met during my work at the institute for everything that I learned from them.

Dr. rer. Nat. Heinz-Lorenz Günter for introducing my person to the world of UHV techniques. Nearly everything that I know about UHV systems, has been pictured and explained by him. Also the knowledge of german culture that I gained, has its origin in the hot discussions with Hi-Lo.

I would like to thank my wife Maria for her patience and understanding during this hard time. Her love has given me the faith and power to proceed.

Specjalne podzikowania dla moich rodzicw i rodzestwa za ich wsparcie i wyrozumiao. Dziki nim doszeem do wszytkiego co mam.

I would like to thank James DiGugliemo for his friendship and nice time during our coffee meetings at the Clemens student hostel.



## Lebenslauf

Marcin Czubanowski  
 Fundstr. 12  
 30161 Hannover  
 Geb. am 10. Oktober 1978 in Posen / Polen  
 verheiratet

### Schulbildung

1984–1993 Besuch der Grundschule in Nochowo / Polen.  
 1993–1997 Liceum Ogólnokształcące im. gen. J. Wybickiego w Śremie.  
 1997 Allgemeine Hochschulreife.

### Studium der Physik

1997–2002 Physikstudium an der Universität Posen / Polen.  
 12.2002 Master of Science.  
 2003–2004 Studium der Physik an der Universität Hannover.  
 2004 Diplomarbeit in der Arbeitsgruppe von Prof. Dr. H. Pfnür mit dem Thema:  
*Growth modes and electrical properties of thin silver films  
 on Silicon on Insulator substrat.*  
 06.2006 Diplom im Fach Physik.

### Promotion im Fach Physik

06.2004 Beginn der Dissertation bei Prof. Dr. H. Pfnür mit Tätigkeit als wissenschaftlicher Mitarbeiter am Institut für Festkörperphysik der Universität Hannover.